Electromechanical behaviour of three-dimensional (3D) woven composite plates

A thesis submitted to the University of Manchester for the degree of

Doctor of Philosophy

In the Faculty of Science and Engineering

2016

Mohamed Nasr Saleh

School of Materials

The University of Manchester

Table of Contents

1 Introduction 17

1.1 Background 17

1.2 Problem definition 21

1.3 Aims and objectives 22

1.4 Research outline 23

2 Literature Review 26

2.1 Introduction 26

2.2 Mechanical characterisation of 3D woven composites 26

2.3 X-ray Computed Tomography of 3D woven composites 29

2.3.1 Principle of operation 30

2.3.2 Scanning Artefacts 33

2.3.3 X-ray CT application in composites 35

2.4 Electrical Resistance Monitoring (ERM) of composite materials 37

2.4.1 Principle of operation 38

2.4.2 Effect of surface preparation 40

2.4.3 Damage detection in CFRP laminates 41

2.5 Composite joints design 43

2.5.1 Composite joints' challenges 43

2.5.2 Types of composite joints 44

2.6 Modelling of 3D woven composites 51

2.6.1 Elastic material properties prediction 52

2.6.2 Damage and Strength Evaluation 55

2.7 Concluding Remarks 60

3 Manufacturing and characterisation of 3D woven composites 61

3.1 Materials specifications 61

3.2 Resin Film Infusion (RFI) 63

3.3 Volume fraction Analysis 66

3.2.1 Acid digestion 66

3.2.2 Directional fibre volume fraction analysis 66
3.2.3 Effect of z-binder on directional V_f 67
3.4 X-ray Computed Tomography 68
3.5 Concluding Remarks 70
4 Tensile Properties of 3D woven composites 71
4.1 Mechanical Testing 71
4.1.1 Test specimens preparation 71
4.1.2 Test Setup 71
4.2 On-axis mechanical properties 73
4.3 Off-axis mechanical properties 76
4.4 Failure mechanisms 78
4.5 Energy absorption 85
4.6 Concluding Remarks 87
5 Electrical resistance monitoring for damage detection in 3D woven composites 89
5.1 Introduction 89
5.2 Test specimen preparation 91
5.2.1 Monotonic testing 91
5.2.2 Cyclic testing 93
5.3 Results and discussion 93
5.3.1 Initial resistance measurement 93
5.3.2 On-axis tension resistance variation 95
5.3.3 Off-axis tension resistance variation 97
5.4 Concluding Remarks 106
6 Open hole tension of off-axis 3D woven composites 108
6.1 Introduction 108
6.2 Testing procedure 109
6.2.1 Specimen preparation 110
6.2.2 Test setup 111

6.3 Results and discussion 111
6.3.1 Stress strain curves 111
6.3.2 Damage evolution 115
6.4 Concluding Remarks 119
7 Bearing strength response of off-axis 3D woven composites 120
7.1 Introduction 120
7.2 Testing procedure 121
7.2.1 Test setup 121
7.2.2 X-ray CT setup 122
7.3 Results and discussion 123
7.3.1 Stress strain curves 123
7.3.2 X-ray CT damage characterisation 127
7.4 Concluding Remarks 131
8 Micro-mechanics based damage model for 3D orthogonal woven composites 132
8.1 Introduction 132
8.2 Model considerations 133
8.3 Micro-mechanics damage model 136
8.3.1 Structure of the mechanical fields 136
8.3.2 Strain energy density and homogenisation of the damaged layer 137
8.3.3 Micro-mechanics based damage evolution 140
8.4 Results and Discussion 144
8.4.1 Stress strain curves 144
8.4.2 DIC Results 145
8.4.3 Micro-mechanical modelling 145
8.5 Concluding Remarks 149
9 Conclusions and Recommendations 151
9.1 Introduction 151
9.2 Conclusions 151

Tensile properties 151
Electrical resistance monitoring 152
Open hole tension 153
Bearing strength 153
Micro-mechanics model 154
9.3 Summary 154
9.4 Recommendations for future work 156
References 157

List of Figures

Figure 1.1 Types of 3D Textile Preforms based on [1] 18
Figure 1.2 Types of 3D Woven Composites (a, b) AI, (c, d) ORT based on Ansar *et al.* [1] 21
Figure 2.1 Schematic of X-ray CT process [34] 31
Figure 2.2 Schematic of X-ray CT different acquisition techniques: (a) fan beam, (b) cone beam, (c) parallel beam [35] 31
Figure 2.3 Types of adhesively bonded joints [65] 45
Figure 2.4 Bonded joints strength as function of adhesive layer thickness [65] 46
Figure 2.5 Types of bolted joints [65] 47
Figure 2.6 Joint efficiency as function of diameter to width ratio [71] 48
Figure 2.7 Bolted joints failure modes [70] 49
Figure 2.8 Interaction of failure modes as function of plies percentage in $0^{o}/\pm45^{o}$ CFRP laminate [71] 50
Figure 2.9 Composite joint design template for ply orientation selection [70] 51
Figure 3.1 Schematics of 3D woven composites unit cells: (a) ORT, (b) LTL, (c) AI 62
Figure 3.2 Schematic of the vacuum bagging technique 64
Figure 3.3 Vacuum bagging assembly attached to gauge to check the vacuum level and leakage 64
Figure 3.4 Diagram of infusion and curing cycle for MTM 57 65
Figure 3.5 Cutting orientation to produce 3D woven composite specimens in warp, weft and bias (off-axis) directions 65
Figure 3.6 3D orthogonal woven composite: (a) unit cell reconstruction from X-ray CT scans, (b) cross-section view along the binder path 69
Figure 3.7 3D Layer-to-layer woven composite: (a) unit cell reconstruction from X-ray CT scans, (b) cross-section view along the binder path 69
Figure 3.8 3D Angle interlock woven composite: (a) unit cell reconstruction from X-ray CT scans, (b) cross-section view along the binder path 70

Figure 4.1 Experimental Setup: (a) testing setup, (b) speckle pattern used for DIC 72
Figure 4.2 On-axis stress/strain curves: (a) ORT, (b) LTL, (c) AI 73
Figure 4.3 Strain contour ($\boldsymbol{\varepsilon yy}$) obtained by the DIC system and unit cell representation in (a) ORT, (b) LTL, (c) AI specimens (note: the black frames show the respective unit cell) 75
Figure 4.4 Off-axis stress/strain curves: (a) ORT, (b) LTL, (c) AI 78
Figure 4.5 On-axis failure mode in (a) ORT, (b) LTL, (c) AI 79
Figure 4.6 (a) Stress levels (Points A, B, C, D) in the off-axis stress/strain curve selected for damage observation by X-ray, (b) X-ray images of ORT, LTL, AI specimens at specified points 82
Figure 4.7 Stitched X-ray scans for the interrupted test 83
Figure 4.8 Off-axis failure mode in (a) ORT, (b) LTL, (c) AI 84
Figure 4.9 Off-axis X-ray cross-sectional slices in planes (a) without binder, (b) with binder, (c) close to the fracture region 85
Figure 4.10 Energy absorption of 3D woven composites 86
Figure 5.1 Schematic of the electrodes position on a testing specimen 91
Figure 5.2 (a) Experimental setup for tensile test, (b) 4-Probe technique for resistance monitoring 93
Figure 5.3 Normalised resistance variation in monotonic on-axis tension test: (a) ORT, (b) LTL and (c) AI 96
Figure 5.4 Normalised resistance variation in monotonic off-axis tension test: (a) ORT, (b) LTL, (c) AI and (d) comparison 98
Figure 5.5 Damage evolution in off-axis tested specimens 100
Figure 5.6 Cyclic off-axis tension of ORT: (a) stress and normalised resistance variation vs. time and (b) cyclic normalised resistance variation vs. stress 101
Figure 5.7 Magnification for the resistance variation in the last loading/unloading cycle 102
Figure 5.8 Cyclic off-axis tension of AI: (a) stress and normalised resistance variation vs. time and (b) cyclic normalised resistance variation vs. stress 103

Figure 5.9 Cyclic off-axis tension of LTL: (a) stress and normalised resistance variation vs. time and (b) cyclic normalised resistance variation vs. stress..... 104
Figure 5.10 Comparison between the level of damage and cross-section reduction for 3D woven composites in cyclic off-axis tension..... 104
Figure 5.11 (a) Reduced modulus and plastic strain calculation schematic, (b) evolution of resistance as function of damage level 105
Figure 6.1 (a) CNC lathe machine, (b) carbide drill bit with 2 mm diameter 110
Figure 6.2 Open hole tension (a) Test setup (the hole has been highlighted for clarification), (b) Typical speckle pattern around the hole 111
Figure 6.3 Stress strain curves for un-notched "solid" vs. notched "dashed" lines for (a) ORT, (b) LTL, (c) AI..... 112
Figure 6.4 Notch sensitivity/normalised strength in off-axis composites..... 113
Figure 6.5 Evolution of axial strain contour map for ORT (a) 0.05, (b) 0.09, (c) 0.11, (d) 0.18 mean strain 116
Figure 6.6 Evolution of axial strain contour map for LTL (a) 0.04, (b) 0.07, (c) 0.09, (d) 0.12 mean strain 117
Figure 6.7 Evolution of axial strain contour map for AI (a) 0.06, (b) 0.10, (c) 0.12, (d) 0.15 mean strain..... 117
Figure 6.8 Optical surface images at failure for (a) ORT, (b) LTL, (c) AI..... 119
Figure 7.1 Schematic diagram of double-lap bearing strength test..... 122
Figure 7.2 Bearing stress vs. bearing strain curves up to 50% strain for (a) ORT, (b) LTL, (c) AI..... 124
Figure 7.3 transformed bearing strength: (a) schematic, (b) comparison with compressive strength in warp and weft directions..... 126
Figure 7.4 Bearing stress vs. bearing strain: (a) up to 50% strain, (b) failure strain 127
Figure 7.5 At 50% strain: (a, b, c) damaged specimens, (d, e, f) X-ray front view for ORT, LTL and AI respectively 129
Figure 7.6 X-ray CT scans at 50% strain: (a, c, e) virtual sectioning along the warp direction, (b, d, f) isometric 3D volume for ORT, LTL and AI respectively..... 130

Figure 8.1 Schematic diagram of: (a) 3D orthognal woven composite unit cell, (b) cross-ply laminate simplification, (c) micromechanics reference problem 135
Figure 8.2 Micro-meso energy equivalence: (a) actual damaged weft layer, (b) homogenised weft layer with reduced stiffness 137
Figure 8.3 Damage evolution as a function of crack density: (a) transverse damage indicator, (b) shear damage indicator 143
Figure 8.4 Damage evolution as a function of applied strain: (a) Transverse damage indicator, (b) Shear damage indicator..... 143
Figure 8.5 3D orthogonal woven composite: (a) stress strain curves, (b) DIC strain contour at failure with unit cell highlighted in the black frame 144
Figure 8.6 Damage progression: (a) binder localised damage, (b-d) transverse damage in weft yarns, and (e-f) fibre breakage in warp yarns 146
Figure 8.7 Stress strain curves for the model vs. experimental results: (a) along warp direction, (b) along weft direction 147
Figure 8.8 Prediction of normalised elastic properties due to transverse cracking in (a) weft yarns, (b) warp yarns 148

List of Tables

Table 3.1 Material properties of IM7 fibre and MTM57 resin.....61
Table 3.2 Specifications of textile architecture of 3D woven composites.....62
Table 3.3 Total volume fraction of constituents (fibre, matrix, void) in 3D woven composites.....67
Table 3.4 Directional fibre volume fraction in 3D woven composites.....68
Table 4.1 Young's modulus, tensile strength and failure strain of 3D composites in warp and weft directions.....74
Table 4.2 Off-axis tensile modulus, strength and failure strain of 3D woven composites.....76
Table 4.3 Strain and stress levels at the "knee point" for off-axis tensile test 80
Table 4.4 Nomenclature of damage types in off-axis tension test.....80
Table 4.5 Sequence of damage events during tensile loading of off-axis 3D woven composites.....84
Table 4.6 Experimental rotation angles for off-axis specimens at 95% UTS 87
Table 5.1 Initial resistance for tested architectures in ohms (Ω).....94
Table 5.2 Nomenclature of damage types.....99
Table 5.3 Modulus, plastic strain and normalised resistance as function of the loading cycles 105
Table 6.1 Comparison between average notched and un-notched strength for 3D woven architectures loaded off-axially.....113
Table 7.1 Summary of bearing stiffness and strength for ORT, LTL and AI.....124
Table 7.2 Comparison of transformed bearing strength against warp and weft compressive strength for ORT, LTL and AI.....126
Table 7.3 Nomenclature of damage types in bearing strength test.....128
Table 8.1 Elastic properties of 3D orthogonal woven composite: Experimental vs Analytical.....134
Table 8.2 Comparison between experimental and modelling results 148

Abstract

Three dimensional (3D) woven composites have attracted the interest of academia and industry thanks to their damage tolerance characteristics and automated fabric manufacturing. Although much research has been conducted to investigate their out-of-plane "through thickness" properties, still their in-plane properties are not fully understood and rely on extensive experimentation. The aim of this work is to study the electromechanical behaviour of three different fibre architectures of 3D woven composites "orthogonal (ORT), layer-to-layer (LTL) and angle interlock (AI)" loaded, in three different orientations "warp (0°), weft (90°) and off-axis (45°)", in quasi-static tension. Stress/strain response is captured as well as damage initiation and evolution up to final failure. The ORT architecture demonstrated a superior behaviour, in the off-axis direction, demonstrated by high strain to failure (~23%) and high translaminar energy absorption (~40 MJ/m^3). The z-binder yarns in ORT suppress delamination and allow larger fibre rotation during the fibre "scissoring motion" that enables further strain to be sustained. *In-situ* electrical resistance variation is monitored using a four-probe technique to correlate the resistance variation with the level of damage induced while loading. Monotonic and cyclic "load/unload" tests are performed to investigate the effect of piezo-resistivity and residual plasticity on resistance variation while damage is captured by X-ray scanning during interrupted tests at predefined load levels. In addition, this study investigates the potential of using 3D woven composites in joint assemblies through open-hole tension and "single fastener double-lap joint" bearing strength tests. 3D woven composites in the off-axis orientation, especially ORT, demonstrate a potential for overcoming some of the major challenges for composite joints' applications which are the pseudo-ductility, stress redistribution away from the notch and notch insensitivity. Finally, the study proposes a micro-mechanics based damage model to simulate the response of 3D orthogonal woven composites loaded in tension. The proposed model differs from classical damage mechanics approaches in which the evolution law is obtained by retrofitting global experimental observations.

Declaration

No portion of the work referred to in the thesis has been submitted in support of an application for another degree or qualification of this or any other university or other institute of learning.

Copyright Statement

I. The author of this thesis (including any appendices and/or schedules to this thesis) owns certain copyright or related rights in it (the "Copyright") and he has given The University of Manchester certain rights to use such Copyright, including for administrative purposes.

II. Copies of this thesis, either in full or in extracts and whether in hard or electronic copy, may be made only in accordance with the Copyright, Designs and Patents Act 1988 (as amended) and regulations issued under it or, where appropriate, in accordance with licensing agreements which the University has from time to time. This page must form part of any such copies made.

III. The ownership of certain Copyright, patents, designs, trademarks and other intellectual property (the "Intellectual Property") and any reproductions of copyright works in the thesis, for example graphs and tables ("Reproductions"), which may be described in this thesis, may not be owned by the author and may be owned by third parties. Such Intellectual Property and Reproductions cannot and must not be made available for use without the prior written permission of the owner(s) of the relevant Intellectual Property and/or Reproductions.

IV. Further information on the conditions under which disclosure, publication and commercialisation of this thesis, the Copyright and any Intellectual Property and/or Reproductions described in it may take place is available in the University IP Policy (see http://documents.manchester.ac.uk/DocuInfo.aspx?DocID=487); in any relevant Thesis restriction declarations deposited in the University Library, The University Library's regulations (see http://www.manchester.ac.uk/library/aboutus/regulations); and in The University's policy on Presentation of Theses.

Dedicated to

My Parents and My Wife

Acknowledgments

I would like to express my gratitude to my supervisors, Professor Constantinos Soutis, Professor Gilles Lubineau and Professor Prasad Potluri for their valuable guidance and support throughout my PhD research journey. In addition, I would like to acknowledge the support from the technical and administrative staff of the National Composites Certification and Evaluation Facility (NCCEF) at the University of Manchester (UoM). Special thanks to Dr. Adam Joesbury, Dr. Matthieu Gresil, Dr. Clara Frias, Dr. Mubeen Arshad, Dr. Yan Liu and Dr. Zhen Li. I highly appreciate the support and guidance I received from the Composite and Heterogeneous Material Analysis and Simulation (COHMAS) Laboratory at King Abdullah University of Science and Technology (KAUST) especially Dr. Arief Yudhanto, Dr. Lakshmi Selvakumaran, Dr. Jian Zhou, Ran Tao and my friend Ditho Pulungan. Special thanks to the staff at Henry Moseley X-ray Imaging Facility, especially Professor Philip Withers, Dr. Bo Yu, Dr. Ying Wang and Dr. Julia Benhsen. Thanks to UK-Datacomp Project for funding this research work. Last but not least, I would like to extend my gratitude to my family members, my wife and my dear friends for their love and support throughout the whole journey.

List of Publications

The following publications are based on the work detailed in this thesis:

1. Saleh MN, Yudhanto A, Potluri P, Lubineau G, Soutis C. "***Characterising the loading direction sensitivity of 3D woven composites: effect of z-binder architecture***". Compos Part A Appl Sci Manuf 2016;90:577–88. doi:10.1016/j.compositesa.2016.08.028.

2. Saleh MN, Lubineau G, Potluri P, Withers PJ, Soutis C. "***Micro-mechanics based damage mechanics for 3D orthogonal woven composites: Experiment and numerical modelling***". Composite Structures 2016:3–12. doi:10.1016/j.compstruct.2016.01.021.

3. Saleh MN, Yudhanto A, Potluri P, Lubineau G, Soutis C. "***Electrical resistance monitoring for damage detection in 3D woven composites***". Composites Science and Technology. "Submitted"

4. Saleh MN, Wang Y, Yudhanto A, Joesbury A, Potluri P, Lubineau G, Soutis C. "***Investigating the potential of using off-axis three-dimensional (3D) woven composites in composite joints' applications***". Applied Composite Materials. "Accepted"

1 Introduction

1.1 Background

Transition from traditional metallic materials to composite materials remarked a revolution in the industrial and engineering applications during the previous decades. The need for light weight and low cost materials has driven researchers and engineers to investigate the potential for replacing metals and alloys with composite laminates and study thoroughly their mechanical, electrical and thermal properties. This is mainly due to the high strength and stiffness-to-weight ratio of those composites. They have excellent mechanical and thermal properties along with low density [1]. However, most of the composite materials used so far are in the form of laminates. These two dimensional (2D) laminates are suitable for applications in which the applied loads are in-plane loads as they are characterised by high in-plane mechanical properties such as high strength and stiffness. The major challenge that faces expanding into 2D laminated composites' usage is their out-of-plane properties. Although the in-plane properties of 2D laminated composites are high and suitable for many applications, their out-of-plane properties represent the weakest part of their application. This is mainly due to the fact that only the resin is responsible for keeping the stacked layers "lamina" together. The adhesion force between the resin and the fibres is always the problem, especially in the case of impact loading. This has led many researchers and engineers to try to use tougher resins or do some prior chemical or plasma treatments to the fibres to increase the adhesion strength [1].

Many applications in industry are exposed to out of-plane loading conditions that make it impossible to resort to the 2D laminates as the proper solution. Wind turbine blades, stringers and stiffeners in aircraft, pressure vessels and construction applications are some examples of applications in which out-of-plane loading conditions are imposed on the structure. The need for composite materials with

enhanced through-thickness "out-of-plane" properties emerged in order to replace metals in such applications. Instead of trying to enhance the adhesion strength of the 2D laminated composites, building a 3D textile structure has drawn more attention from both industry and researchers. This is not only due to the fact that a 3D composite structure will have better through thickness properties, but also it will save time in manufacturing. Using textile techniques to produce 3D composites is capable of producing large volume of preforms at faster rate. So, this will dramatically reduce the manufacturing cost, increase the flexibility of the design and increase the productivity [4]. Production of 3D textile preforms can be classified (Fig. 1.1) into major and minor categories. The superior edge of 3D textiles "composites" is the existence of a binder in the thickness direction that holds the composite from separating. Unlike 2D laminated composites, out-of-plane properties of 3D composites do not only depend on the adhesion strength between the matrix and fibres. The stuffer added in the third direction improves the integrity of the whole structure considerably although it may have a negative effect on the in-plane properties as it will be discussed later in this section.

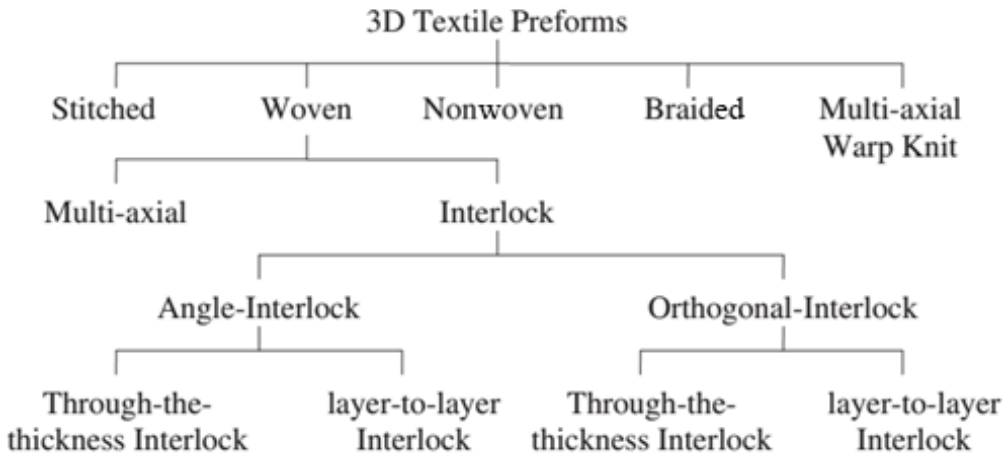

Figure 1.1 Types of 3D Textile Preforms based on [1]

The "enhanced out-of-plane properties" are not the only advantage of 3D composites. The delamination resistance, due to the binder, enhances the 3D

composite impact performance as well as damage resistance [4]. In addition; 3D composites allow flexibility and variety in their structure. This can be utilised to manufacture near-net-shape preforms. So, it reduces the manufacturing cost and manufacturing time even further. Although various techniques exist for manufacturing 3D textile preforms, the most widely used nowadays is the weaving category due to its high production rate along with the ability to produce various 3D woven structures [1]. For engineering applications, the 3D woven interlock architecture received more attention during the past decades. This category is further divided into two main groups. This classification is according to the interlacing angle of the structure. The first category is the angle interlock (AI) in which the interlacing angle between the fibres "binder and weft" can have any value except 90° (Fig. 1.2a, b). The second category is a special case of the first one. The orthogonal interlock (ORT) (Fig. 1.2c, d) occurs when the interlacing angle between the fibres "binder and weft" is equal to 90° [1]. Again both categories can be further classified according to the path of the binder in the thickness direction to layer-to-layer (LTL) or through thickness (TT) interlock (Fig. 1.2b, d). 3D woven LTL and AI architectures have been used in industrial applications where load is required to be transferred around a bend such as brackets, curved beams and T-shaped profiles [2]. In such applications, the developed architectures were reported to resist the interlaminar shear and radial stresses developed in service. In Automotive industries, LTL woven composite was used to replace the high-strength steel (HSST) beams [3]. In addition, McClain [4] reported successful usage of LTL and AI architectures in truss beams with integral off-axis stiffeners as well as stiffened panels in which continuous fibres run from the skin into each stiffening element. In this way, it overcomes the need for fasteners and bonds at joints which is one of the major challenges facing 2D laminated composites nowadays. ORT architecture has been successfully used in the LEAP project to manufacture fan blades and engine casings for A-320-neo, Comac C-919 and 737-MAX as well as fuselage barrel stringers on long-range aircraft [5,6]. Another interesting application of 3D ORT carbon fibre architectures is reported by

Hemrick *et al.* [7] in ultra-light weight heat exchangers for vehicle radiators. The application made use of the high thermal conductivity of 3D ORT architecture as the through-thickness binder creates a conduction path for the heat dissipation, In addition, In addition, Sharp *et al.* [8] and Mohamed *et al.* [9] have reported the usage of 3D ORT architecture in wind turbine rotor blade applications. The concept was to integrate Π-joints with I-beam joints to connect the shear web and the spar cap in order to resist delamination and improve the damage tolerance of the blade.

In spite of the previously mentioned advantages of 3D composite preforms, still the usage and applications are limited [10]. One of the main reasons for this limited application is the level of knowledge required to control the manufacturing process parameters. During the resin infusion process, it is essential and challenging, at the same time, to make sure that the resin has the ability to reach all the intricate positions in the 3D complex woven architecture in order not to have voids in the manufactured part. On the other hand, there may be positions of rich resin pockets in the composite as well. Many parameters affect the quality of the produced component such as the resin viscosity, the 3D woven composite architecture and the mould design. This requires a properly designed and controlled environment during the infusion process. Additional manufacturing defects can be in the form of fibre breakage, in-plane fibre distortion or z-binder fibre distortion. Tong reports a comprehensive study about the manufacturing defects and their possible causes [11]. Beside the manufacturing challenges; 3D woven composites are characterised by lower in-plane properties compared to 2D laminated composites. This is due to the fibres undulation or "crimp" caused by the interlacement of the longitudinal fibres "warp", transverse fibres "weft" and z-binding fibres "binder" [12]. The influence of the crimp on the in-plane properties was studied by Stig [13]. So, it is always a trade-off between the enhanced out-of-plane properties and the reduced in plane properties. This is an open area for optimising 3D woven composites according to specific applications. One last concern regarding 3D woven composites is to understand their mechanical behaviour in the elastic region; but more

importantly when damage occurs. Extensive experimental work has to be carried out before expanding in the usage of 3D woven composites in engineering applications. This is, of course, a tedious and very expensive task at the same time. The other solution, that is more appealing to researchers, is coming up with predictive analytical and numerical models that can save time and effort in evaluating the behaviour of those materials in application.

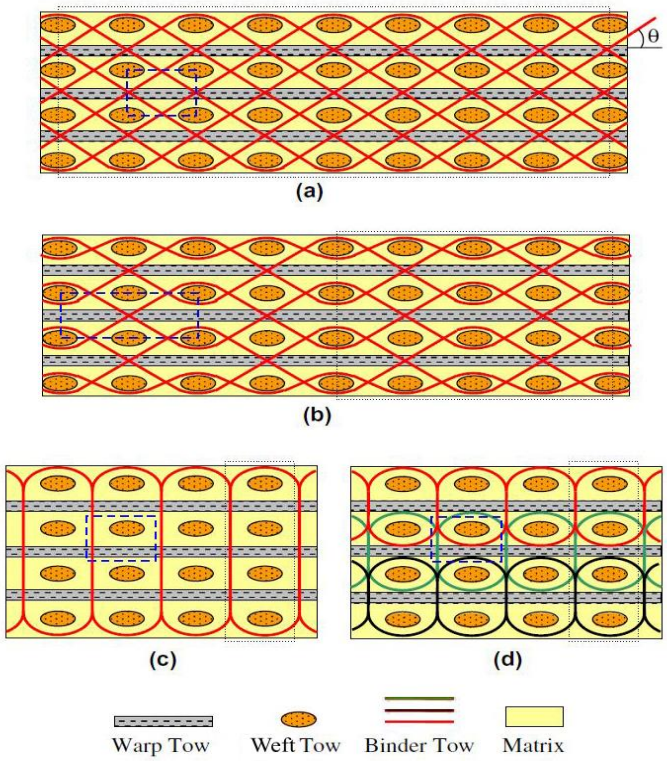

Figure 1.2 Types of 3D Woven Composites (a, b) AI, (c, d) ORT based on Ansar *et al.* [1]

1.2 Problem definition

There is still a need to understand the in-plane loading sensitivity of various z-binder architectures of 3D woven composites subjected to warp, weft and bias loadings. The relationship between damage mechanisms and energy absorption also needs to be revealed.

1.3 Aims and objectives

The main objective of this research is to investigate the loading direction sensitivity of 3D woven composites and its effect on the global stress strain response as well as the damage mechanisms and damage progression. The energy absorption for three different architectures: (i) layer-to-layer (LTL), (ii) angle interlock (AI), and (iii) orthogonal (ORT) tested along warp, weft and bias (45°) directions are evaluated to come up with a recommendation plan for utilising specific 3D woven architecture for specific application such as composites joints. In addition, a micro-mechanics based damage model is proposed to simulate the response of 3D orthogonal woven composites in tension. The proposed model differs from classical damage mechanics approaches in which the evolution law is obtained by retrofitting global experimental observations.

In order to achieve this research objective, the following milestones are set:

- Manufacture three different architectures of 3D woven composites: (i) layer-to-layer (LTL), (ii) angle interlock (AI), and (iii) orthogonal (ORT) using the Resin Film Infusion (RFI) process.
- Test those architectures in quasi-static tension along warp, weft and bias (45°) directions to characterise their mechanical properties and damage evolution.
- Determine the effect of the z-binder yarns on: (i) void content, (ii) failure and damage mechanisms in each case, (iii) energy absorption for all the tested architecture and orientations.
- Evaluate the damage evolution with a new proposed Structural Health Monitoring (SHM) technique by means of Electrical Resistance Monitoring (ERM) for all the tested architecture and orientations.
- Investigate the notch sensitivity of 3D woven composites tested in off-axis “bias” tension with a circular hole.

- Determine the bearing strength of the off-axis 3D woven composites to evaluate the potential of using them in composite joint applications.
- Develop a micro-mechanics based damage model for 3D orthogonal woven composites.

1.4 Research outline

Following the introduction given in **Chapter 1**, the literature review, divided into six sections, is presented in detail in **Chapter 2**. The first section gives an introduction for the different topics detailed in the chapter. The second section discusses the previous research that investigated the mechanical performance and characterisation of 3D woven composites. This also covers the damage mechanisms and damage evolution under various types of loading out-of-plane "i.e. impact loading" and in-plane "i.e. tension, compression and shear loading". The following section extends the damage characterisation by means of X-ray computed tomography in which internal damage is revealed. The fourth section deals with the principle of ERM and its applications in SHM of carbon-fibre composites. Different damage mechanisms detected by ERM such as fibre breakage, matrix cracking, delamination and impact damage are detailed in the literature review. Challenges of using composites in composite joint applications are the focus of the fifth section. And finally, the various attempts to model the mechanical response of 3D woven composites with their advantageous and limitations are discussed in the sixth section.

In **Chapter 3**, the different types of 3D woven composites considered in this study are detailed as well as the manufacturing process to produce the composite panels. This is followed by the characterisation techniques, such as the volume fraction process and X-ray scans, used to evaluate the quality of the manufacturing process in terms of void content, and fabric distortion.

Chapter 4 then describes the experimental procedures to determine the tensile behaviour of 3D woven composites; followed by the experimental results. A

comprehensive discussion is detailed to investigate the effect of the z-binder architecture on the on-axis and off-axis mechanical properties, damage and failure mechanisms and finally energy absorption. Digital Image Correlation (DIC) is used to provide a strain contour map during testing; and X-ray CT scans are carried out to evaluate the level of damage induced as a function of the applied strain/deformation mainly for the off-axis loaded specimens in which excessive damage is captured.

Afterwards, **Chapter 5** proposes the potential of using ERM as a SHM technique for damage detection in 3D woven composites. The testing procedures, in terms of specimen preparation and types of applied loadings, are detailed. Monotonic loading up to failure is carried out for all architectures in both On-axis and Off-axis orientations. Then, the effect of the z-binder on the initial resistance and correlation between level of damage and resistance increase is discussed. Finally, the chapter concludes by discussing results of the cyclic "load-unload" test carried out for the off-axis specimens.

Chapter 6 continues investigating the notch sensitivity of 3D woven composites loaded in tension in the off-axis direction. The testing procedures, in terms of specimens' preparation and the testing setup, are detailed. Then global stress/strain response is captured along with damage evolution using the DIC system. And finally, the fracture mechanism of the three architectures is compared.

As a step further to investigate the potential of 3D woven composites in meeting the requirements of composite joint applications, **Chapter 7** discusses the single-fastener double-lap joint bearing strength response of the off-axis 3D woven architectures (ORT, LTL and AI). Following the testing procedure, results of the global stress/strain response is highlighted. The comparison is established for all the architecture based on the global behaviour, energy absorption, damage mechanisms revealed by X-ray CT images and final failure.

Then, **Chapter 8** proposes a micro-mechanical damage based model for predicting the response of a 3D orthogonal woven composite loaded in tension. The derivation and assumption of the model are discussed in detail based on micro-mechanics. And the chapter concludes by comparing the predicted global stress/strain response in both warp and weft directions against the experimental results as well as the damage evolution mechanisms. Limitations of the model are also detailed, and recommendations for improvement are suggested.

Finally, the main findings of this research work are discussed and summarised in **Chapter 9** along with recommendations for future work.

2 Literature Review

2.1 Introduction

This chapter reviews previous work to provide better understanding of the research studies carried out for 3D woven composites and shows how the current research fits in the global framework of characterising 3D woven composites. First, it discusses the experimental characterisation techniques for 3D woven composites including mechanical characterisation and damage detection. The principle of X-ray computed tomography (X-ray CT) is described briefly with focus on the advantages, artefacts and applications in fibre-reinforced composites. Then, a survey of using electrical resistance monitoring (ERM) as a structural health monitoring (SHM) technique for damage detection and evaluation in composite materials is introduced. Challenges of designing composite joints and possible solutions are highlighted. Afterwards, modelling strategies for 3D woven composites are evaluated. Finally, a summary of the main key points and conclusions are presented.

2.2 Mechanical characterisation of 3D woven composites

Although the potential use of 3D woven composites is clearly apparent, their application is still limited [10] for various reasons. The first reason is that 3D woven composites generally exhibit lower in-plane properties in comparison with 2D non-crimp fabric (NCF) laminated composites [13,14] since they are inherently characterised by undulation or "crimp". This crimp is a direct result of the interlacement of longitudinal, transverse and through-thickness yarns [11]. The degree of crimp is dependent on the adopted woven architectures and the tension force during the weaving process. Secondly, the damage mechanisms in 3D woven

composites are complex as they involve interaction among damage modes within and between yarns, the effect of rich resin regions, voids and geometrical imperfections due to the manufacturing and compaction process. Thirdly, 3D woven composites are loading sensitive as yarns are distributed in three directions. For instance, the response of 3D woven composites in the warp and weft directions can be different. The problem is more complex when off-axis (bias) loading is considered.

As the main advantage of 3D woven composites is clearly their out-of-plane enhanced properties, many researchers [15–19] studied the effect of the z-binding yarns on the impact damage behaviour and the energy absorption of those material systems. Hao *et al.* [15] studied the behaviour of 3D orthogonal woven glass fibre composite plate and T-beams subjected to quasi-static indentation and impact loadings. Global response in the form of load displacement and energy absorption curves were evaluated; and Finite Element Modelling (FEM) results were validated against them. The implemented model correlated well with their experimental findings. In addition, damage mechanisms in the case of the T-beam and the plate were compared. They reported higher energy absorption by the T-beam as opposed to the composite plate for the same loading level. Another study by Ji *et al.* [16] investigated the quasi-static indentation and impact behaviour of a circular plate made of 3D orthogonal woven glass fibre composite. They developed a unit cell model to simulate the damage behaviour using a VUMAT subroutine in ABAQUS/Explicit. The model results were in good agreement compared to the experimental results and they suggested expanding the capabilities of their model for other 3D woven architectures. Luo *et al.* [17] carried out quasi-static indentation and transverse impact tests for 3D orthogonal hybrid woven composites with aramid and glass fibre yarns. The focus of this study was the strain rate sensitivity effect on energy absorption. It was reported that the higher the impact velocity, the higher the energy absorbed by the composite. Regarding the damage/failure mechanisms, the quasi-static loaded specimens suffered from tensile failure on the bottom side and compressive failure on the top side. In the

case of impact damage, three damage mechanisms were captured: matrix cracking, fibre breakage and fibres pull-out. Unlike laminated composites, the effect of the through-thickness binder was significant as it supressed the delamination. An interesting study by Seltzer *et al.* [18] revealed the damage mechanisms of 3D S2-glass, carbon and hybrid woven composites by X-ray micro-tomography due to low-velocity impact. In addition, they compared the energy absorption of the 3D woven composites with 2D laminated counterparts. They reported that the energy absorbed by the 3D woven composites was twice the energy absorbed by the 2D laminated composite. The X-ray images demonstrated that this higher energy absorption was due to the binding yarns delaying the delamination and providing integrity to the structure. The existence of binding yarns resulted in dissipating the energy by other damage mechanisms such as tow splitting, out-of-plane shear and extensive fibre breakage.

For the in-plane properties' characterisation, much work has been done to characterise the failure mechanisms of 3D woven composites under tension [19–30] along the warp- or weft-directions. Gerlach *et al.* [19] who investigated angle interlock 3D woven composites subjected to tension (warp, weft) showed that the effect of z-binder volume fraction on the in-plane properties is minor. Cox *et al.* [22,23] studied the failure mechanism of 3D woven composites (orthogonal, layer-to-layer) monotonically loaded in tension, compression and bending. They found that the dominant failure modes in 3D interlock woven composites are tow rupture and pull-out (tension case), delamination and kink-band formation (compression case), and a combination of those failure modes (bending case). The influence of fabric architecture in 3D woven composite under tensile, compressive and bending loads was investigated by Dai *et al.* [20] where they found that the mechanical performance is affected by resin rich region and waviness of load-carrying fibres. They also showed that angle interlock architecture outperforms orthogonal 3D woven composite for all loading conditions. For 3D orthogonal woven composites under tension, Lomov *et al.* [24] found that damage initiates firstly at binder interlacement points. It is then followed by transverse cracks in yarns

perpendicular to the loading direction and local delamination between yarns. Final failure is characterised by fibre failure that leads to complete rupture of the specimen. Warren *et al.* [29] characterised the global stress/strain curves and failure modes of 3D twill harness orthogonal woven composites, 3D layer-to-layer woven composites and 2D woven architecture under warp and weft tensions. In-plane shear testing was also carried out using V-notched rail shear method, where they found that the shear among adjacent tows and matrix degradation are the dominant damage mechanisms in shear. Visrolia and Meo [30] performed on-axis tension (0° direction), off-axis tension (45° direction) and compression tests to validate their modelling strategy for 3D orthogonal woven composites. A good agreement of global stress/strain was demonstrated between their proposed model and the experimental results, although for off-axis tension the experimental results were reported up to 3% strain only (not until failure) and the damage mechanism under shear was not revealed. Pochiraju and Chou [27] reported the behaviour of 3D woven composites (layer-to-layer angle interlock, through-thickness angle interlock) under tension in warp and weft directions. Nonetheless, limited work has been performed to characterise 3D woven composites under off-axis loading (bias direction). Ivanov *et al.* [31] have reported loading direction sensitivity (warp, weft, bias) of 3D woven composites but the materials were limited to orthogonal architecture. Nevertheless, there is still a need to evaluate the loading sensitivity of various architectures of 3D woven composites subjected to warp, weft and bias loadings. The relationship between damage mechanisms and energy absorption also needs to be revealed.

2.3 X-ray Computed Tomography of 3D woven composites

X-ray computed tomography (X-ray CT) is a technique that enables visualising the internal structure of a scanned object without cutting. This technique utilises a 2D slice images "radiographs" captured at different angles to computationally process

them afterwards into a 3D reconstructed volume. It has been widely used in the medical field for more than 50 years since it was employed to visualise human tissues and bones [32]. Recently, this technique has gained more attention from the researchers in the composites field as a non-destructive testing technique to be used for microstructure visualisation. Using the X-ray CT technique can reveal information about the internal geometry of a microstructure, defects and the damage/cracking level. In this way, the acquired knowledge of the internal features of composite materials improves the predictions and understanding of the macroscopic behaviour and eventually leads to better and enhanced design capabilities. In the following sections, the principle of operation of the X-ray CT is explained highlighting the challenges and limitations in the field. And finally, some examples from the literature are discussed to demonstrate the capability and potential of using X-ray CT in the composite field.

2.3.1 Principle of operation

X-ray radiography represents the basis for X-ray computed tomography. The principle of operation is based on the attenuation law [33]. As the X-ray beam travels through an object, photons are absorbed, transmitted or scattered by the object's material. The difference between the incident beam energy and the transmitted beam energy is the attenuation due to the material of the object. In the case of fibre-reinforced composites, different constituents have different attenuation capabilities, so this creates the contrast in the X-ray radiographs. Capturing 2D radiographs while rotating the object 180º or 360º is then the basis for X-ray CT imaging. The X-ray CT process consists of three main stages which are summarised as: acquisition, reconstruction and analysis. The acquisition and reconstruction processes are depicted in Fig. 2.1. The specimen/object is mounted on a rotary stage to control the rotation angle during the scanning. The transmitted X-ray beam is then captured on a photo detector resulting in series of 2D projections. Finally, the 2D projections are reconstructed into a 3D volume. Acquisition, reconstruction and analysis processes are discussed further in the following sections.

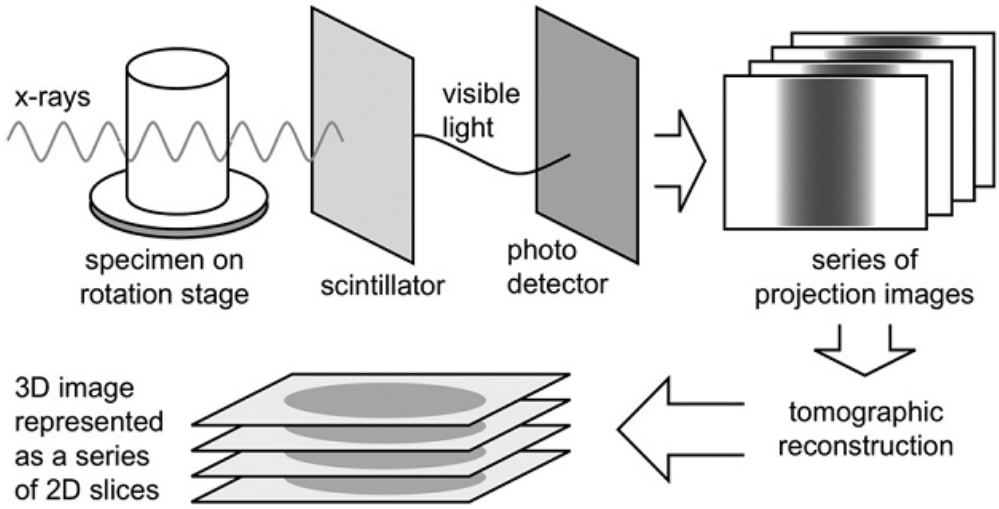

Figure 2.1 Schematic of X-ray CT process [34]

2.3.1.1 Acquisition

As highlighted before, the X-ray beam is emitted from the source, travels through the sample and finally is captured by the detector. The sample can be moved towards the X-ray source or towards the detector to control the resolution of the scan. Due to the detector field of view limitation, a compromise has to be made between the sample size and the resolution required [35]. Both the X-ray source and detector may vary in type; and accordingly the quality of the scans is affected. Fig. 2.2 shows three different acquisition techniques namely as fan beam, cone beam and parallel beam respectively.

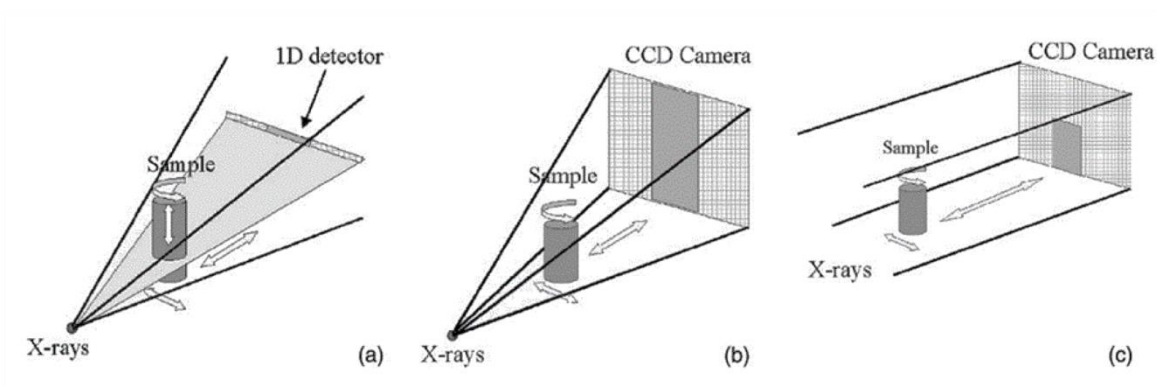

Figure 2.2 Schematic of X-ray CT different acquisition techniques: (a) fan beam, (b) cone beam, (c) parallel beam [35]

In the first two techniques (see Fig. 2.2a, b), the X-ray beam initiates from a micro-focus source having a cone shape which might lead to scanning artefacts such as beam hardening (see Section 2.3.2) upon reconstruction. In contrast, the parallel beam configuration (see Fig. 2.2c) applies an intense parallel X-ray beam which improves the scanning and reconstruction quality significantly and simplifies the reconstruction algorithm complexity [34]. For the detector, it can be either a line detector (see Fig. 2.2a) or a 2D planar detector (see Fig. 2.2b, c). In the case of a line detector, the specimen needs to be moved vertically during the scanning process which leads to longer scanning time compared to the 2D planar detector.

2.3.1.2 Reconstruction

The next step after acquiring the series of projections is reconstructing these 2D slices/radiographs to produce a 3D volume. Once the 3D volume is reconstructed, the scanned data can be visualised in the form of 2D cross-sectional slices or a 3D reconstructed volume. The transition from the 2D acquired images into the 3D volume is done using suitable reconstruction algorithms. There are various algorithms developed over the years such as: the filtered back projection (FBP) algorithm by Herman [36], the Feldkamp-Davis-Kress (FDK) algorithm [37] and the algebraic reconstruction technique (ART) algorithm [38]. The FDK algorithm is mainly suitable for small angle cone beam systems while the ART algorithm is suitable for parallel beam systems. For detailed explanation of the algorithms, the listed references are recommended.

2.3.1.3 Analysis

After reconstruction, analysis of the data is essential to utilise the scanning and visualisation capabilities offered by the X-ray CT technology. It is up to the user to decide to what extent the reconstructed data requires processing and analysis. Some users can be interested mainly in visualising the scanned objects. Others may require more analysis through separating the different constituents or features of the 3D reconstructed volume. This is applicable in the analysis stage by segmenting the 2D images or the 3D volume according to the grey scale level. This helps extracting features of interest such as voids, yarns, cracks and resin-rich

regions in composites for instance. In addition, the segmentation process can be taken one step further to quantify the 3D reconstructed data. Calculating the void content or the fibre volume fraction in a composite can be achieved using post-processing software such as Avizo. For modelling purposes, the segmented data can be used to generate 3D geometry and meshes and export them to finite element software packages for mechanical, thermal, electrical or any other multi-physics analysis.

2.3.2 Scanning Artefacts

Over the past decades, extensive research has concentrated on improving both the X-ray CT scanning "acquisition" and the reconstruction algorithms. Despite this fact, avoiding scanning artefacts is almost impossible. A scanning artefact can be defined as any unnecessary feature that appears in the scans or the reconstructed volume other than the actual features of the scanned object. Scanning artefacts can result from the scanning set-up while others can result from the image processing "reconstruction stage". Sometimes it is possible to get rid of those artefacts and remove them from the scanned images. Others are inherent to the images and cannot be avoided. In this section, some of the most common artefacts are discussed further suggesting methods to avoid them. The reader is referred to [39] for a more comprehensive review about X-ray CT scanning artefacts.

2.3.2.1 Ring Artefacts

One typical scanning artefact in X-ray CT is the ring artefact. It is usually identified in the scanned images by concentric circles around the axis of rotation as reported in [39]. The possible reasons causing this artefact can be having faulty elements in the detector or having differences in the sensitivity between adjacent elements in the detector. Another possible cause for ring artefacts is the non-linear signal intensity spread. Thus, calibrating the detector before the scans can adjust the spread of the signal intensity and control it to be linear. And just by shifting or translating the stage/object before scanning, the effect of bad "faulty" elements can be avoided.

2.3.2.2 Beam Hardening

Another artefact that is quite common in X-ray CT is beam hardening. It results from the polychromatic nature of the X-ray beam. The low-energy photons of the beam are absorbed as they travel through the scanned object while the remaining high-energy photons experience less attenuation [40] which leads to non-linear attenuation through the thickness of the object. The beam hardening artefact can be spotted in the 3D reconstructed volume as shading effects. Adding filters to the path of the incident beam before scanning or correcting it after scanning in the reconstruction process can help eliminating this artefact.

2.3.2.3 Centre of rotation

The first step required to perform the reconstruction after scanning is the determination of the centre of rotation of the projection images. If the centre of rotation is not determined properly, it results in distortion of the 3D reconstructed volume especially at the free edges. Large deviation from the actual centre of rotation leads to clear double edge effects while small deviation results in blurry images. The centre of rotation artefact is characterised by constant spacing between the two edges across the entire image [39]. This centre of rotation artefact is better corrected before acquisition by carefully positioning the specimen on the rotary stage and checking the centre of rotation. If it is not cleared before the scanning process, it can still be accounted for in the setup of the reconstruction stage.

2.3.2.4 Partial volume effect

One example of an inherent artefact in X-ray CT imaging is the partial volume effect. This artefact represents more a limitation of the capability of the imaging system. When the feature of interest is smaller, in size, than the spatial resolution of the system it cannot be captured. The reason behind this is that more than one constituent, with different attenuation coefficients, occupy a single voxel. So, the averaging of these coefficients represents the attenuation coefficient of the voxel resulting in the partial volume artefact. This artefact is quite common to be observed in composite materials scanning because small features such as micro-

cracks or delamination can be smaller than the voxel size leading to blurred images. Thus, the quantification accuracy can be affected.

2.3.3 X-ray CT application in composites

Advancements and capabilities of X-ray CT have been employed in many research projects to detect manufacturing defects such as voids [41,42] as well as damage progression in the form of matrix cracking [43,44], delamination [45–47] and fibre fracture [48]. A brief summary of those previous studies is discussed in this section.

Early work by Desplentere *et al.* [49] investigated the effectiveness of using X-ray micro CT in capturing the geometrical characteristics and micro-structure of four different types of 3D woven fabrics. In order to assess the quality and accuracy of this technique, dimensions "width, thickness and spacing" of the yarns obtained by X-ray micro CT slices were compared against dimensions measured by optical microscopy images. Statistically, no significant variation was observed from the comparison. However, the variation within the micro-structure of the individual fabrics was found to be quite significant. Finally, authors reported good agreement between the predicted material properties using micro-mechanics analysis and the experimental values which confirmed the reliability of using X-ray micro CT as an input for the textile composite models.

Lambert *et al.* [41] examined the fatigue life response of glass fibre reinforced epoxy used in wind turbine blades. The as-manufactured coupon specimens were CT scanned to visualise the internal microstructure and quantify the void content. Voids were segmented, extracted and quantified in a volumetric distribution. They tried to find a correlation between the void content and the fatigue lives of the specimens, but there was no such correlation on the global void distribution. However, on a local ply-level, it was found that there is a clear correlation between the fatigue life and the largest void in those specific regions. The sub-critical damage propagates to critical damage starting from those local voids. Another recent study by Nikishkov *et al.* [42] argued that the current techniques for porosity/void detection in X-ray CT are susceptible to large errors and they can be

only used for qualitative analysis. So, they proposed a quantification model for void detection in composites. The model was validated for unidirectional carbon/epoxy composites as well as carbon/epoxy fabric manufactured with specific porosity levels. In addition, the method was successful in detecting and quantifying voids for composites with drilled micro-holes.

For matrix cracking detection, Bull *et al.* [43] presented a partial volume correction technique to better capture the crack opening displacement (COD). Two sets of data were used for validation, particle-toughened and non-toughened carbon fibre composites, subjected to low velocity impact. The estimated COD results were compared with results from higher resolution synchrotron radiation computed tomography (SRCT). Unlike conventional voxel counting to detect a crack, the developed method was able to accurately estimate the crack openings within 20% of SRCT results. One recent study by Yu *et al.* [44] investigated the damage evolution in angle interlock (AI) and modified layer-to-layer (MLL) 3D woven glass fibre/epoxy composites subjected to tension-tension fatigue loading. Using X-ray CT and scanning electron microscopy (SEM), matrix cracking and fibre matrix debonding was revealed. The first cracking mechanism observed is debonding between the binder yarns and in-plane yarns. Then, transverse matrix cracking uniformly distributed in the weft yarns perpendicular to the loading direction is observed. Due to stress concentration at the crack tip, delamination between warp and weft yarns was observed in both architectures but it was more extensive in MLL compared to AI.

Wright *et al.* [45] used synchrotron radiation computed tomography (SRCT) to visualise damage in carbon-fibre epoxy composite at the sub-micron level. The resolution used enabled the researchers to capture individual fibre breakage. The study concluded that delamination and intra-laminar cracking played a key role in localising fibre fracture. The authors suggested that using such visualisation capabilities improves the understanding of the physics governing crack propagation in composites. Moreover, Sket *et al.* [47] studied the damage evolution in carbon-

fibre epoxy laminates in shear using X-ray CT. Three main aspects were captured, including matrix cracking, inter-ply delamination and fibre realignment, as a function of the applied strain. They developed an algorithm to automatically quantify the cracking density and fibre rotation. The study revealed the complexity of the interaction between the different damage mechanisms. In addition, application of X-ray CT was successful in capturing the matrix cracking evolution and fibre realignment.

Aroush *et al.* [48] utilised high-resolution SCRT to validate the stochastic models developed for prediction of tensile strength and failure of unidirectional composites. Using quantitative analysis of the X-ray CT results, they concluded that the conventional stochastic models underestimated the size of critical cluster of adjacent broken fibres by a factor of 3 to 5 of the "failed-fibres" cluster. They also proposed a simple fracture mechanics model to predict the composite strength according to their X-ray CT data.

One recent study by Straumit *et al.* [50] proposed a quantification method for the determination of fibres orientation and degree of anisotropy in 3D woven composites which they referred to as the structure tensor method. The degree of anisotropy and the principal directions were determined from the scanned images as a three-dimensional function of the grey level values. Using the proposed model was successful in segmenting the composite constituents as yarns, matrix and voids. In addition, segmentation of yarns depending on their orientation was achieved. This can be useful to automatically generate voxel-based geometrical description of complex microstructures such as 3D woven composites.

2.4 Electrical Resistance Monitoring (ERM) of composite materials

Carbon fibre reinforced polymer (CFRP) composites have become widely used in aerospace and automotive applications due to their high specific stiffness and

strength properties. Such applications benefit significantly from the weight savings that such material systems offer. However, detecting damage in CFRP composites is a challenging task. Internal damage or even the barely visible impact damage (BVID) can go without being noticed which can lead to catastrophic damage of composite materials. Thus, there is a need for an automatic reliable structural health monitoring (SHM) techniques for CFRP composite structures. Utilising the electrical conductivity of carbon fibre has been applied in strain sensor applications [51]. Electrical resistance monitoring (ERM) of CFRP has attracted more interest for decades because it does not require any extra cost or expense for instrumentation. In addition, it does not require specific fabrication process or embedding of sensors such as optical fibres. In contrast, ERM can be applied to existing CFRP structures without compromising the strength or the mechanical properties. In spite of all the previously highlighted advantages, this technique is still challenged by the strong anisotropic nature of CFRP composites because the conductivity along the fibre direction is much higher than the transverse to fibres direction and the through-thickness direction, as will be discussed below.

2.4.1 Principle of operation

In CFRP composites, the carbon fibres are highly conductive while the matrix is an insulator. In an ideal situation, the electrical conductivity along the fibre direction can be simply estimated as the volume fraction of the fibres multiplied by the conductivity of fibres while the conductivity along the transverse and through-thickness directions should be almost zero. In reality, this is not the case. Unidirectional carbon fibres are not perfectly straight and aligned; on the contrary, they have waviness both in the longitudinal plane and transverse plane. This waviness leads to contact between fibres in both transverse and through-thickness directions creating a conductive network instead. Consequently, the electrical conductivity in the transverse and through-thickness directions is not zero but is definitely much smaller than the conductivity along the fibres. In the case of 2D laminated composites, the conductivity through the thickness (σ_t) only arises from the contact between plies, so it is always orders of magnitude lower than transverse

conductivity (σ_{90}) and longitudinal conductivity (σ_0). According to Todoroki *et al.* [52], the ratio between the transverse conductivity (σ_{90}) and the longitudinal conductivity (σ_0) in laminated composites is of the order of "10^{-3}". And the ratio between the through-thickness conductivity (σ_t) and the longitudinal conductivity (σ_0) is approximately "10^{-4}". In the case of 3D woven composites, due to binder existence, the through-thickness conductivity is much higher than for 2D laminated composites. Such comparison will be discussed in (Section 5.3.1). The conductive fibre-network within a single ply or between plies is disturbed once fibre breakage, matrix cracking or delamination occurs. This results in an increase in the electrical resistance which can be used as a damage indicator.

It is quite important here to differentiate between electrical resistance change due to damage or cracking event and the electrical resistance change due to the piezo-resistivite nature of the material. Piezo-resistance is defined as the change in electrical resistance due to applied strain. A typical example for this phenomenon is conventional strain gauges where the applied strain results in deformation that is directly captured as voltage/resistance change. The electrical resistance (R) as function of the material resistivity (ρ) and the geometrical parameters, length (L) and cross-sectional area (A), is defined as:

$$R = \rho \frac{L}{A} \tag{2.1}$$

So, the change in resistance due to applied strain can be expressed as:

$$\frac{\Delta R}{R} = \frac{\Delta \rho}{\rho} + \frac{\Delta L}{L} - \frac{\Delta A}{A} = (1 + 2\nu)\varepsilon + \frac{\Delta \rho}{\rho} \tag{2.2}$$

where, ($\varepsilon = \frac{\Delta L}{L}$) and ($\nu$) is Poisson's ratio. The change in resistivity is a function of the volumetric change such that:

$$\frac{\Delta \rho}{\rho} = m \frac{\Delta V}{V} \tag{2.3}$$

where, (m) is a material constant. Substituting (2.3) into (2.2), the change in resistance can be correlated to the applied strain through the constant of proportionality known as the gauge factor (K) such that:

$$\frac{\Delta R}{R} = K\varepsilon \tag{2.4}$$

$$K = (1 + 2\nu) + m(1 - 2\nu) \tag{2.5}$$

For most metallic materials [53], the material constant ($m = 1$) and the gauge factor are within the range of 2 to 4. The gauge factor for carbon fibre loaded in tension along the fibre direction [53] has been found to be close to 2. This suggests that the resistance change due to only the piezo-resistive effect is linearly proportional to the applied strain/deformation (see Sections 5.3.2 & 5.3.3).

2.4.2 Effect of surface preparation

Previous studies investigated the effect of the contact between the electrodes and the surface on the electrical resistance measurement [52,54]. Todoroki and Yoshida [52,54] studied electrical resistance variation, for both single ply and multi-ply unidirectional CFRP specimens, using the four-probe technique in which the outer most electrodes are used for current injection while the inner two electrodes are used for voltage/resistance evaluation. Surface preparation in terms of polishing the surface before introducing the electrodes was the main distinguishing parameter in this study. For the same specimens, two sets of data were obtained; one by introducing the electrodes by applying silver paste without polishing the surface and the other after polishing with sand paper. They observed that the resistance change in tension for the non-polished specimens was negative with the applied strain while it was positive for the polished specimens. In order to understand this phenomenon, Todoroki [54] has justified this by the poor quality of contact without polishing. Although contact can be obtained in CFRP specimens without polishing the surface, carbon fibres are not fully exposed. This means that the contact points with the introduced electrodes are minimal. However after polishing, fibres are exposed to the surface of the electrodes and better contact can be achieved which

directly has a significant effect on the electrical resistance measurement. So, unlike metallic materials, the quality of the surface preparation has a significant effect on the resistance measurement using the four-probe technique.

2.4.3 Damage detection in CFRP laminates

Damage detection for CFRP coupon specimens has been extensively investigated in literature. Schulte *et al.* [55] studied the electrical resistance change, of unidirectional laminates, due to tensile cyclic loading. Fibre breakage was found to be the main mechanism of damage that led to a "stepwise" increase in the resistance as a function of the applied strain. Similar observation has been supported by Ceysson *et al.* [56] in addition to damage detection using acoustic emission (AE). The study highlighted that electrical resistance is significantly increased due to fibre breakage. Moreover, the sensitivity of resistance variation was found to be much higher than stiffness degradation experienced by the structure. The thing that suggests that even if the damage effect is not significantly captured from the mechanical behaviour, it can still be detected by the ERM technique. Omagari *et al.* [57] used the four-probe technique to monitor matrix transverse cracking in cross-ply laminates under tension. Using only the four-probes on one surface of the specimen, the electrical resistance increased with the multiplication of transverse cracks. To make sure that the increase in resistance was mainly due to damage and matrix cracking, they unloaded the specimens after testing and monitored the final electrical resistance value. They found out that even after removing the tensile load, there is a residual increase in the resistance so it was proven that the increase in electrical resistance was not due to the piezo-resistive nature of the material.

Other researchers investigated the electrical resistance variation due to the bending and flexural testing of CFRP composites [58–61]. Abry *et al.* [61] studied the change in electrical resistance due to cyclic bending load for cross-ply laminates combined with in-situ damage detection for correlation between the resistance variation and the level of induced damage. Due to bending load, matrix cracking

and fibre-matrix debonding were found to be the dominant damage mechanisms that led to the increase in the electrical resistance. In addition to the direct current (DC) analysis, alternating current (AC) was also applied to determine the capacitance of the studied cross-ply laminates. They found that cross-ply laminates had a high capacitance that decreased with the increased level of induced damage. They explained this by the fact that the interface layers between plies are resin layers which acted as electric insulators. Todoroki [58] *et al.* also used the ERM method to detect delamination in beam-type cross-ply laminate specimens in inter-laminar shear tests. The test was designed to induce delamination between plies and then the ERM method was used along with the inverse problem method to determine the location and size of the induced delamination. Results obtained from their study suggested that ERM method was successful not only in determining the location of the delamination but also the size of it. However, they recommended a minimum of five electrodes to be attached to the surface to accurately detect delamination in those beam-type specimens. As a continuation of their study, Hirano and Todoroki [62] investigated the potential of the ERM method for delamination detection in woven CFRP laminates. Again using beam-type specimens with induced delamination by inter-laminar shear testing, they used the surface response method to solve the inverse problem. Their technique was proven to be successful for woven CFRP laminates as it was for cross-ply and quasi-isotropic laminates. Less research [63,64] has been carried out to investigate the capability of ERM in detecting impact damage in CFRP composites. They concluded that the method seemed to be less developed to identify the location and size of the damage; however the effect of the impact damage caused apparent change in the electrical resistance of the CFRP structures. In other words, the ERM technique can detect damage due to impact loading but further development is essentially required to have a practical efficient methodology.

2.5 Composite joints design

2.5.1 Composite joints' challenges

Although composite laminates are characterised by high stiffness and strength to weight ratio (high specific stiffness and high specific strength), in real life application where joining structures made of composites laminates is essential, the ultimate strength and stiffness of the structure is determined by the joint strength and joining efficiency [65]. Mainly there are two different joining techniques for composite laminates summarised as bonded joints and mechanically fastened joints; mainly achieved by bolting. Sometimes both techniques are combined to form bonded-bolted joints [66]. Several requirements for a successful joint design in service are outlined below:

- ***Material ductility/yielding***

  Composite materials are significantly less ductile than the types of metals used for similar structural. The stress, usually, cannot be distributed around a stress concentration region such as a notch or a hole, which is common in joints.

- ***Notch insensitivity***

  The ultimate strength and stiffness of metallic materials are not significantly affected by notches or drilling holes. However, composite laminates exhibit approximately 50% reduction in strength as compared to their un-notched strength.

- ***High strain to failure/energy absorption***

  As composite materials are brittle by nature, the energy absorbed up to final failure and strain to failure is relatively small especially if the material is loaded along the fibre direction.

These previously highlighted challenges make composite materials more susceptible to damage and joint problems once in service. The weaknesses of composite laminates in the in-plane shear, transverse and inter-laminar shear leads the design of composites to rely mainly on the notch/reduced properties instead of utilising the un-notched excellent properties. Some research has been done to try to overcome some of the issues highlighted such as the notch sensitivity and stress redistribution. In order to alleviate the stress concentration around holes in composite laminates, two methods were proposed and reported in [65,67]. The first method is referred to as the Softening Strip method [67] in which a strip of a relatively softer composite, several times the hole diameter, is inserted around the hole/notch. In this case, the less stiff inserted material helps in reducing the stress concentration around the hole but there is no control on the load redistribution. The second method is called the Stiffening Strip method [65]. In this method, a relatively stiffer material is inserted away from the hole so that the load is attracted to that specific region. In the following section, types of composite joints and their design considerations are discussed further.

2.5.2 Types of composite joints

The first type of composite joints is bonded joints. Adhesively bonded joints have been used for decades in structural applications [68]. The major design parameter in bonded joints is the area of the adhesive layer. There has to be enough bonding region to withstand the applied load in shear. This is the reason why most of the commonly used bonded joints have an overlap area with varying adhesive length depending on the load carrying capacity required. Different types of bonded joints are shown in Fig. 2.3. The single-lap and double-lap joints are the most common types of bonded joints in practice. Both joints are examples of joints where thin adhesive layers can be applied [68]. For applications exposed to higher load levels, the stepped-lap and scarf joints are used with thicker adhesive bonding layers.

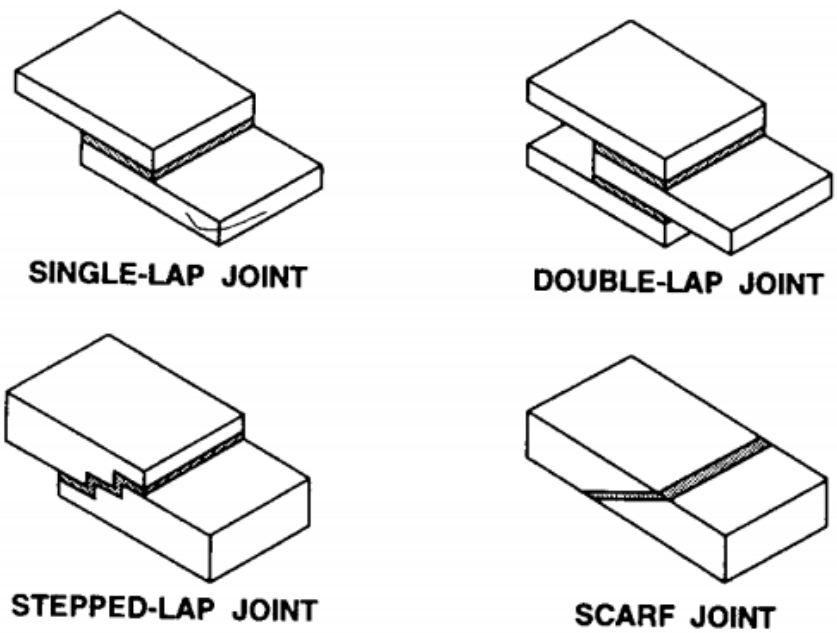

Figure 2.3 Types of adhesively bonded joints [65]

The other design parameter in bonded joints is the thickness of the bonding layer. It is not necessarily true that increasing the bonding layer thickness would increase the joint strength (see Fig. 2.4). Two extreme cases were investigated by Goland and Reissner [69] which are very thin bonding layers versus very thick bonding layers for single-lap joints. In the first case, the bond layer does not affect the joint flexibility while the thick layer contributes significantly to the joint flexibility. They studied the normal and shear stresses in the bond layer. According to Jones [65], the thick-layer approach is found to be more suitable for fibre-reinforced composites as the epoxy resin contributes to the effective thickness of the bonding layer. As per their findings, the shear and normal stresses in the bond layer are almost uniform except for significant concentration close to the end of the joint. A comparison between the various types of bonded joints depending on their efficiency, strength and modes of failure is detailed in Fig. 2.4. As mentioned before, the conventional single-lap and double-lap bonded joints are not designed for transferring higher loads as opposed to stepped-lap and scarf joints. For single-lap joints, due to the eccentricity in the load, bending moment is generated which leads to final failure of the joint. In the case of double-lap joints, there is no

bending applied and the joint fails due to shear only in the form of peel failure. The effect of the adhesive layer thickness is not obvious in either single or double-lap joints, but it increases the strength of the other types of bonded joints in a linear manner. For stepped-lap and scarf joints, shear failure is the most common failure mode.

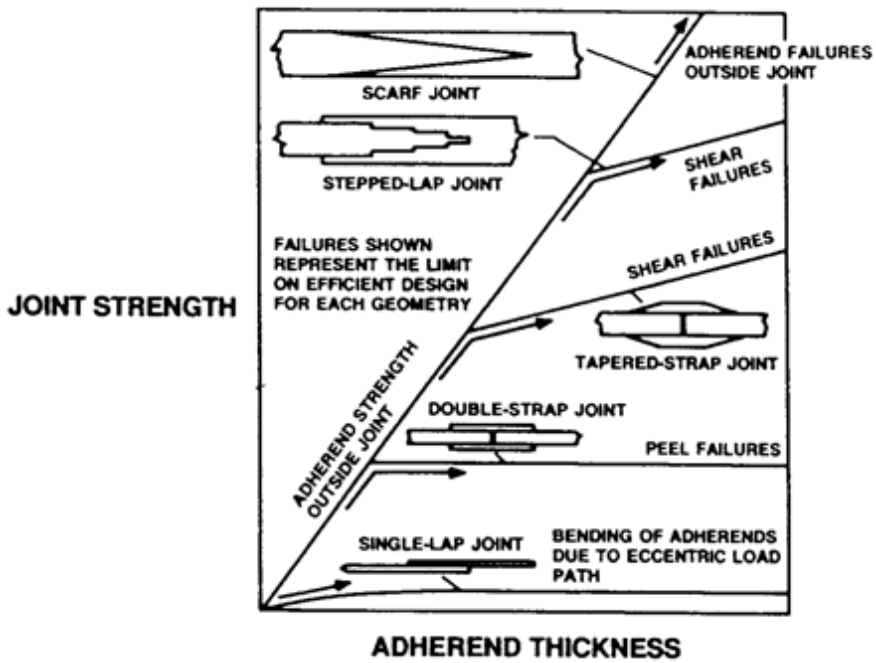

Figure 2.4 Bonded joints strength as function of adhesive layer thickness [65]

The second type of composite joints is the bolted one. In this case, drilling holes is a requirement to accommodate bolts or rivets. Similarly to bonded joints, bolted joints have various types (see Fig. 2.5). Again, the conventional types are single-lap and double-lap bolted joints while more complicated joints can be classified as reinforced-edge and shimmed joints.

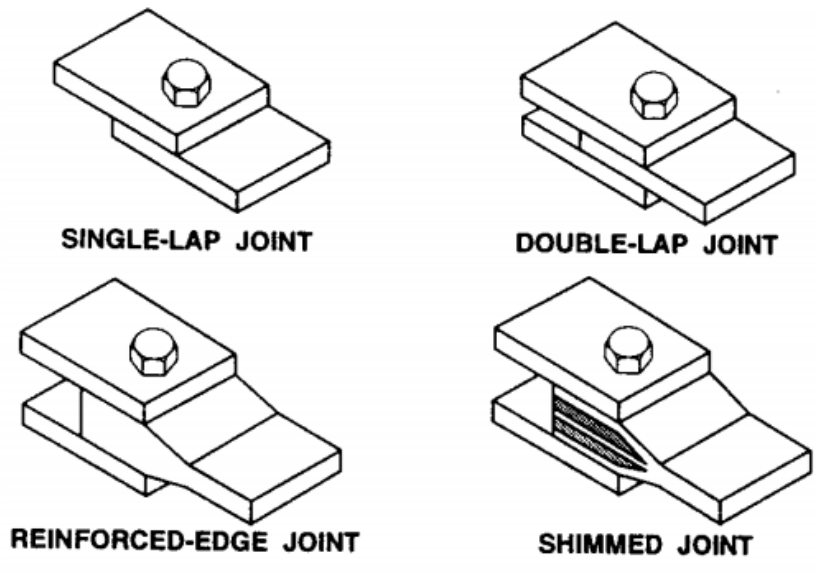

Figure 2.5 Types of bolted joints [65]

The main design concern in bolted joints is the stress concentration around the hole. For composite laminates, the stress concentration around the hole and the joint efficiency is function of the geometrical parameters (hole diameter "*d*", width "*w*", edge distance "*e*" and thickness "*t*") and the laminate lay-up orientation [70]. Joint efficiency is defined as the joint strength divided by the laminate ultimate strength. Although fibre-reinforced composites consist of two or more brittle materials, there is still a tendency to relieve some of the stress concentration around the holes. This tendency of stress concentration relief in composite laminates has been attributed to the progressive damage mechanisms [71] such as transverse cracking, delamination between plies and fibre matrix debonding at the hole periphery. So, it is not accurate to consider the response of CFRP bolted joints as brittle materials (see Fig. 2.6). On the other extreme, ductile material joints have almost double the efficiency of CFRP joints for the same diameter to width ratio (see Fig. 2.6). This is due to the yielding nature of ductile materials that results in load redistribution and stress concentration relief.

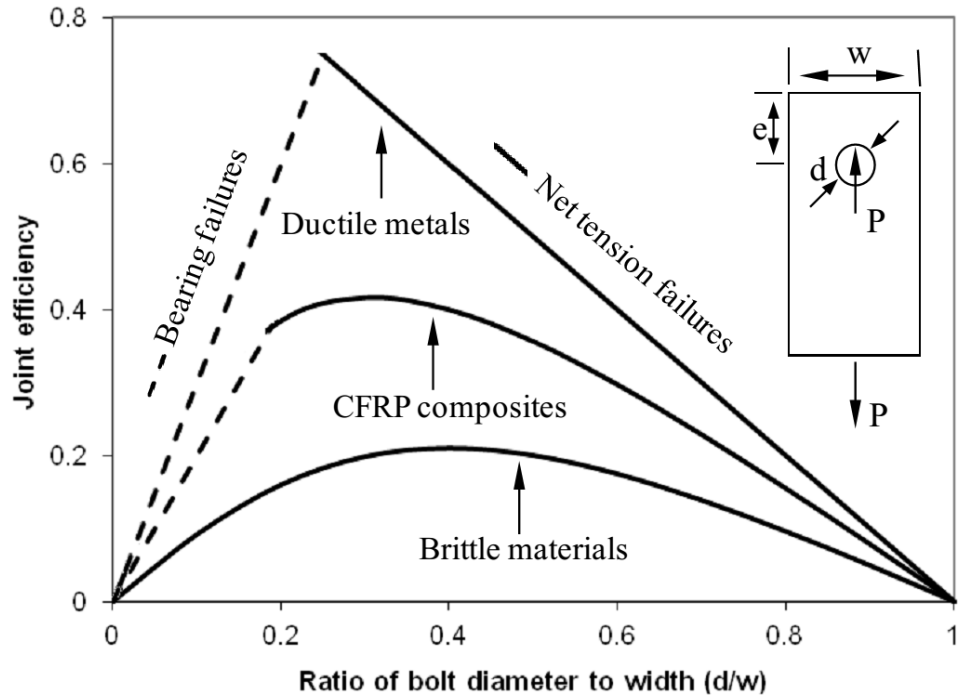

Figure 2.6 Joint efficiency as function of diameter to width ratio [71]

Various failure modes are experienced by composite bolted joints. The most common failure modes in single-fastener bolted joints are described in Fig. 2.7. Net-tension failure occurs mainly when the specimen is not wide enough to resist the normal stress applied (w/d ratio is low). Furthermore, when the specimen width can withstand the normal stress but the distance to edge is small, the specimens fail due to the shear stress developed, causing the second failure mode which is shear-out failure (e/d ratio is low). In both lateral cases, the compressive stress induced is not high enough to trigger damage and failure before net-tension or shear-out failures [71]. When the compressive stress is significant, it leads to bearing failure in which fibres kinking, matrix cracking, micro-buckling and delamination are the dominant damage mechanisms. Tong and Soutis [70] reported several studies that summarised the relationship between the geometrical parameters and the failure modes. They concluded that decreasing the specimen width leads to a point where the load carrying capacity of the joint is significantly reduced and the mode of failure changes from bearing to net-tension failure. Similarly, decreasing the distance of the hole from the edge changes the bearing

mode of failure to shear-out failure which directly affects the joint strength. To avoid bolt bending, a maximum thickness to diameter ratio of "one" should not be exceeded [70]. Other failure modes include cleavage and bolt failure in the form of what is called here as "pull-through" failure. All the failure modes cause brittle sudden failure except the bearing failure mode which fails in a non-catastrophic progressive nature. Therefore, bearing failure is the most preferred mode of failure for bolted composite joints in real life applications.

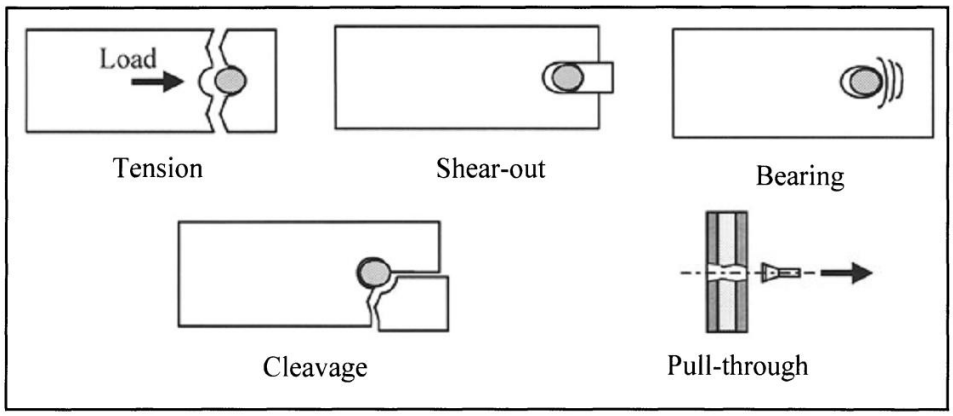

Figure 2.7 Bolted joints failure modes [70]

To design a composite joint to fail in a specific failure mode, the second design parameter comes into action which is the lay-up orientation. Generally, laminates dominated by 90º plies fail in net-tension mode because the load is applied in the transverse direction of the fibres. When the 0º plies dominate the laminate lay-up, the mode of failure changes to shear-out failure as there are not enough plies in the ±45º direction to resist the shear stress developed. Atas [71] reported an interaction chart that explains the dependency of the joint failure mode on the ply orientation for CFRP laminates (0º/±45º). For a specific ($w/d=4$ *and* $e/d=4$) and a fastening torque of 3.4 N.m, Fig. 2.8 demonstrates the failure mode variation as function of percentage of ±45º plies. Up to 40% of ±45º plies, the shear-out failure is the dominant failure mode. For a percentage of (40% to 60%) of ±45º plies, bearing failure dominates and then due to the low tensile strength of plies, the net-tension failure occurs beyond 60%. Both Tong and Atas [70,71] concluded that a design rule of thumb for composite joints is to have 12.5% to 37.5% of the plies in

the basic laminate directions (0º, 90º, +45º and -45º) producing a quasi-isotropic joint.

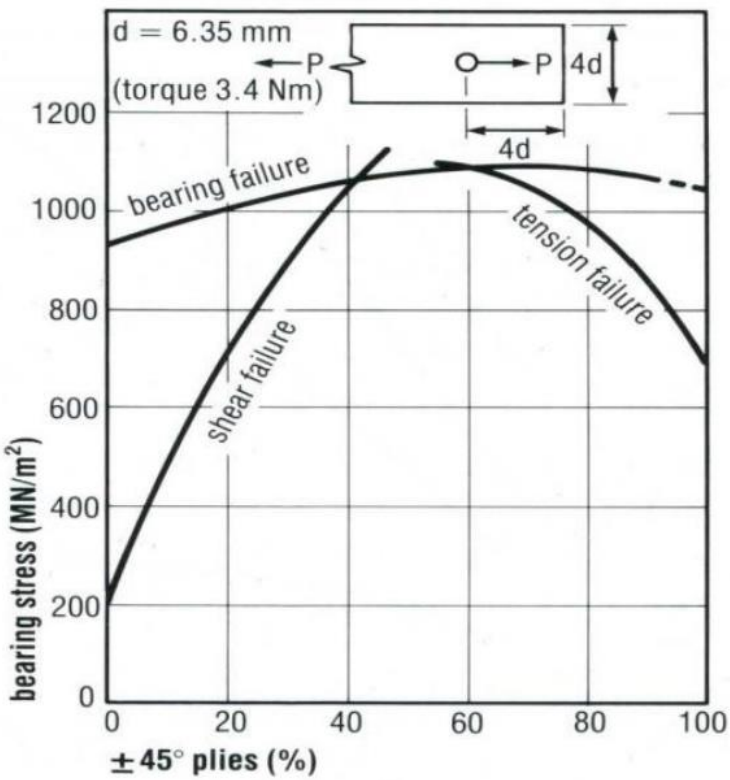

Figure 2.8 Interaction of failure modes as function of plies percentage in 0º/±45º CFRP laminate [71]

A composite joint design recommendation template (see Fig. 2.9) produced by Hart-Smith LJ and reported by Tong and Soutis [70], suggests that quasi-isotropic or nearly quasi-isotropic laminate lay-ups are the most suitable for bolted joints as long as these design recommendations do not conflict with any design requirements or limitations. In addition, the chart sheds some light on other possible lay-ups for lightly loaded structures and the critical lay-ups that should be avoided during the design process. Throughout the entire selection process, the main variables are the percentages of plies in the (0º, 90º and ±45º) directions.

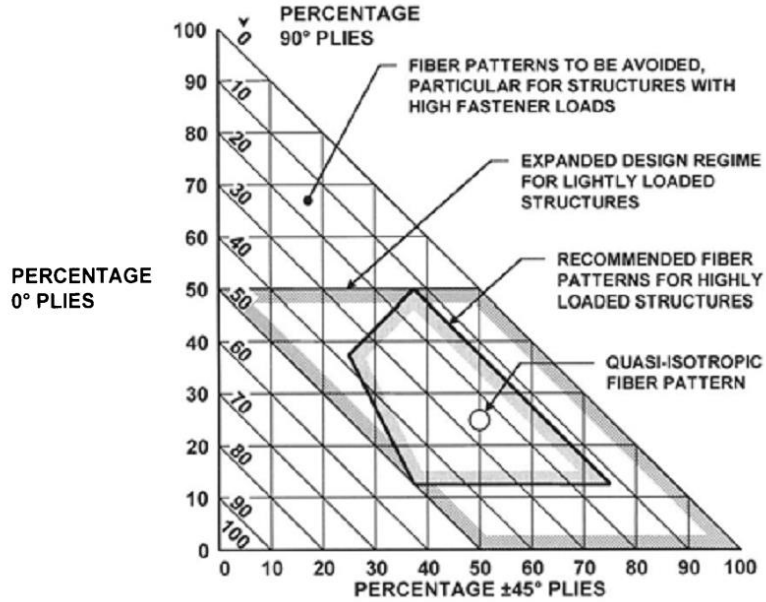

Figure 2.9 Composite joint design template for ply orientation selection [70]

2.6 Modelling of 3D woven composites

The thermo-mechanical behaviour of composites can be divided into three main regimes. The linear elastic regime, in which no damage is introduced, is the first category of the division. Then, damage initiation regime in which the stress state of the composite constituents has exceeded the permissible capacity "threshold" of stresses for the constituents. This regime also includes the damage evolution of the composite constituents beyond damage initiation. Finally, the failure regime occurs when the maximum degradation of material properties, due to damage propagation, is reached. In this stage, the strength prediction of the overall composite on the macro scale is computed. In this section, the three stages of characterising the thermo-mechanical response of composite materials are discussed starting first with evaluating the elastic response then moving forward to model damage initiation and evolution to failure

2.6.1 Elastic material properties prediction

The elastic thermo-mechanical properties of a heterogeneous material are always a function of the properties of the individual constituents and their volume fractions in the composite. Composite materials are a heterogeneous medium in which, at least, two different materials exist with specific volume fractions and interact at the micro-scale. In order to predict the effective material properties of such materials, some simplifications have to take place. The objective is to replace the heterogeneous medium with a virtual homogenous medium that has the same effective material properties as the original medium at the macro-scale.

Modelling of the effective elastic properties of 3D woven composites started with very simple and primitive models; yet they were quite effective in giving an idea about the upper and lower limits of the sought properties. Simple analytical models such as those of Voigt and Reuss are implemented for 3D woven composites as they were implemented before for laminated composites [3]. In these two models, the effective material properties are calculated as a weighted average of the individual constituents' properties; and the weight for the averaging of each of them is the volume fraction of the individual constituents in the medium. Those simplified models are independent of the material orientation that is why they are not so effective in the case of 3D woven composites where complex architectures exist. Unit cell models represent a step forward in the analytical modelling attempts for 3D woven composites. In such models, the effective material properties of the macroscopic level are determined through the representative unit cell (RUC) or in some other cases it is called representative volume element (RVE). The main consideration to apply such models is to have a repeated macroscopic structure that consists of a repeating unit cell. Iso-strain and iso-stress boundary conditions can be applied to the RVE to get an idea about the overall material properties at the macroscopic level. Another attempt utilising the unit cell concept is introduced by Kou and Pon [72]. In this analytical model, the unit cell of ORT architecture is studied to predict the elastic moduli in the three directions.

The yarns are assumed to be solid, homogeneous and straight with no crimp introduced, but they are spatially oriented in the x, y and z directions. Only normal strains are considered and no coupling between normal and shear stresses is involved. Static equilibrium of forces is used to calculate the normal strains from the applied stresses utilising the stiffness of the yarns. In order to predict the overall strain in any direction, the normal strains are averaged over the unit cell. Elastic moduli are then obtained from the global stress and strain tensors. Two cross sections for the yarns are considered elliptical and lenticular. Tensile and three point bending tests are conducted as well to investigate the cracking and damage mechanisms of the ORT architecture. It is found that for a tensile test, damage initiates first in the z binder yarns followed by debonding in the y-yarns. In the case of three point bending, debonding, transverse cracking and inter yarn matrix cracking are the main damage mechanisms.

Orientation averaging (OA) analytical models have also been applied for the same purpose. In this model, the representative cell is divided into small sub-volumes each of which is modelled as a transverse isotropic unidirectional composite. The effective macroscopic properties are then evaluated by averaging the response of the RVE to the external applied load "iso-stress or iso-strain". Cox and Dadkhah have applied this to 3D woven composites [73] by dividing the composite into its three main constituents "stuffer, filler and warp". Each of them has a specific volume fraction. The overall properties are evaluated by averaging the properties of the constituents taking into consideration the geometrical orientation of each of them. The results overestimated the experimental data and this is due to the fact that the model does not take into consideration the effect of fibre waviness. It only assumes that the stuffer and filler are straight that is not the case in the actual composite. So, they introduced a modified orientation averaging model (OAW) in which they introduced a knockdown factor that accounts for the undulation of the fibres and leads to stiffness degradation. The overall predicted properties were improved significantly.

Tan proposed an analytical model in which the RVE is segmented into smaller micro-blocks of tow impregnated matrix [74]. So, each block consists of matrix along with warp, weft or binder tow. To get the effective properties of the composite, the micro-blocks are assembled under the assumption of iso-stress or iso-strain according to specific models listed in their work "XYZ-model, YXZ-model and ZYX-model" [75]. The results were in a good agreement with the experiment but the problem is they did not clarify when to prefer using one of the three models over the other. Another analytical model was developed by Wu *et al.* [76] to predict the material properties of ORT architecture and is further improved by Buchanan *et al.* in [77]. The model divides the RVE into layers; and then divides each layer into stripes. Each stripe is modelled as a unidirectional composite. The properties of the layer are obtained by assembling the stripes under iso-strain or is-stress condition. Similarly, the properties of the composite are obtained by combining the stacked layers. The major difference of modification that makes the Buchanan model more accurate in prediciting the elastic material properties of the composite is the methodology developed in [77] to determine the representative volume fraction of the elements. Although this model is in good agreement with the experimental results, it is constrained by the geometrical complexity of the 3D composite. In other words, the model is mainly applicable to ORT architecture.

Following these analytical attempts, many FEM models have been introduced. A Large scale finite element model is proposed by Kim and Lee *et al.* [78,79] to predict the elastic properties of ORT architecture utilising the power of supercomputing. The model represents virtual material testing as it numerically simulates the complex geometry of the composite including warp, weft and binder yarns along with the matrix. One unit cell structure is repeated multiple times and then assembled to simulate the full finite element model. Moreover, the effect of geometrical irregularities is discussed and multiple solvers are used for the computation. The elastic properties are obtained using Hook's law through averaging the stresses and strains over the whole numerical model. Wang *et al.* [80] implemented a micro macro finite element model to predict the material properties

of ORT architecture using the commercial software MSC Patran/Nastran. Utilising the periodic nature of the composite structure, the RVE concept is used along with periodical boundary conditions to enforce the contiuity of the stress and strain on the boundaries of the RVE [81,82]. The elastic material properties for a single tow are first calculated using a micro-cell model with a hexagonal packing arrangement. Then, those obtained values for a single tow are used along with the matrix properties in a meso-unit cell model of the ORT to evaluate the macroscopic material properties of the structure. Application of periodic boundary conditions on the software are done using the multi-point constraints scheme. The compliance tensor is evaluated, column by column, by applying six independent macroscopic deformations. Another model proposed by Visrolia [30] in which asymptotic expansion homogenisation is employed to predict the macroscopic mechanical properties of ORT from the RVE. Periodic boundary conditions are applied on the boundary of the RVE in six discrete steps to get the total stiffness matrix of the composite. Predicted values were in good agreement with experimental data.

2.6.2 Damage and Strength Evaluation

This section mainly tackles some of the previous work done by researchers in the field of simulating the damage evolution and strength evaluation of 3D composites. Most of the work strategy adopted in the literature takes one of two approaches. The first approach is defining failure criteria for each of the 3D composite constituents. Once a failure criterion is reached, either degradation of the material mechanical properties is described as discrete values or just complete failure is assumed. The second direction is the continuum damage modelling (CDM) approach. In this approach, damage is depicted by an internal damage variable which has a continuous range from undamaged material (d=0) to a completely damaged material (d=1). A damage initiation criterion is specified to determine the threshold for the damage evolution to start. Then, the evolution constitutive relation varies according to the physics adopted to describe the damage evolution.

An analytical model to evaluate the failure strength of ORT is developed by Tong *et al.* [83]. In this model, the RVE consists of warp, weft and binder tows. The macroscopic load is transferred to the RVE scale under iso-strain condition. A maximum stress failure criterion is chosen to determine the failure threshold. Longitudinal failure strength is in a good agreement with the experimental values while the transverse strength is not. This is justified by the fact that the model does not take into account the waviness of weft tows in the actual sample. Further development by Tong *et al.* [84] was done to investigate the tow waviness effect on the strength of ORT. The model assumes that a single tow is represented by a curved beam supported by an elastic foundation. A maximum stress failure criterion is again chosen to determine the ultimate strength of the 3D composite. The predicted failure stresses in the fill direction match well the experimentally obtained results. In addition a parametric study is done to demonstrate the effect of the span length and the waviness amplitude of the filler tow on the failure stress in that direction. Yang *et al.* [85] implemented an empirical model in which the strength of ORT preform is predicted from the strength of its constitutive tows. The stress/strain response of tows and preform is correlated using tensile data for each of them separately. It is found that the stress/strain relationship for the preform is parabolic while the relationship between yarn strain and fabric strain is linear. In this way, the stress in the preform can be deduced from the strain data of the constitutive tows.

Further work has been done for 3D braided composites by Jiwei and Miaolin [86]. In this paper, the Tsai-Wu damage criterion is adopted to determine the yarn failure while the von Mises criterion is used for the matrix. Once the damage criterion is met, property degradation is defined according to the Murakami damage theory. According to this theory, the effective material properties are degraded due to the reduction of the load-carrying area of the material. Four damage patterns were considered for the yarns and the maximum value for the damage is limited to 0.999 to avoid a singularity in the numerical solution. Good agreement is found when compared with the experimental results. Song *et al.* [87]

implemented a FE model for a single unit cell for a braided composite that had geometrical imperfections. The objective of this study was to simulate the compressive response of the braided composite. The composite consisted of fibre impregnated tows and resin. Fibres were assumed to be transversely isotropic elastic-plastic solid elements while resin was modelled as an elastic-plastic solid obeying the J2 incremental theory of plasticity. The RIKS arc-length method was used to simulate the non-linear response of the unit cell and good agreement was obtained with the experimental results. Further improvements were carried out [88] with multiple cells model to investigate the effect of cell number on the compressive response of the braided textile. Results from this study demonstrate that the computational time required has increased dramatically; the compressive stiffness is unaffected; the peak stresses converge. The conclusion is that a 4-cell model is capable of capturing the compressive strength more accurately compared to others.

Bogdanovich proposed a progressive damage model based on the 3D Mosaic model at the RVE level for ORT [89]. In this model the RVE is divided into blocks of either matrix or unidirectional composite laminae. Again the macro-load is transferred to the micro blocks under the assumption of either iso-strain or iso-stress. And, a maximum strain failure criterion for tension, compression and shear is used. Upon identification of a failure mode, a knock-down factor or in other words, a degradation factor of 0.1 is multiplied by the material property of the previous step. Incremental analysis is done until full reduction of the mechanical properties is reached. Once this occurs, the material is assumed to have reached its ultimate failure strength. Moving on to some of the models that used CDM for ORT, a multi-scale finite element model is introduced by Jia *et al.* [90]. In this model, asymptotic expansion homogenisation is carried out on both the micro and meso-scale RVEs in order to evaluate first the elastic material properties. The RVE on the meso-scale is divided into two sub unit cells inner meso-RVE; and surface meso-RVE. A material constitutive behaviour is defined as a UMAT subroutine in ABAQUS/Standard to describe the damage initiation as well as damage evolution

on the micro and meso scales. Modelling results demonstrated good agreement with the experiment.

Although many models in the literature concentrated on understanding the global "macro" behaviour of 3D woven composites, very minor effort is directed towards understanding and simulating the micro-meso cracking and damage mechanisms. Cyclic fatigue bending analysis was conducted by Sun *et al.* [91] to investigate the meso-scale interaction between warp and weft yarns in (LTL) layer-to-layer composite. A half-size FEM model was implemented on ABAQUS/Standard with homogenised yarn properties on the meso-scale. The model revealed the stress concentration points at the warp and weft yarns interlacement points especially away from the mid-plane of the sample. The warp yarns were found to carry most of the load compared to the weft and the matrix. Stress concentration regions from simulation were compared against those of the experiment and good agreement is found. This work is developed further [92] in order to investigate stiffness degradation due to low-cyclic fatigue as well as the damage morphologies. The conclusion is that the stiffness degradation shows a similar trend to the experimental results.

In the model (Section 2.6.1) developed by Visrolia [30], the asymptotic expansion homogenisation is used to correlate the micro-scale stresses to the macro-scale stresses through the determination of the characteristic displacements for the unit cell. Then, stresses in the yarns and matrix are used to determine the damage state and the localised stiffness degradation if damage occurs. Damage growth is defined as a function of the energy release rate. The damage energy release rate is calculated as the derivative of the Gibbs free energy; and the damage indicator is defined as a linear function in the square root of the damage energy release rate. Again, the value for the damage indicator is limited to 0.999 to prevent singularity in the stiffness matrix. The threshold value for damage initiation is estimated by the authors due to the lack of information about this in literature. The logic behind the estimate is considering the yarns' behaviour more of a brittle response

compared to a ductile response for the matrix. So, the damage threshold for the yarns is set close to the failure strength. Finally, the unit cell constituents' properties are homogenised to get the macro-scale response of the composite. Three different loading conditions are applied "tension, compression and shear" to validate the proposed model. The stress strain response and the failure demonstrate good agreement with the experimental data. In addition, the model has the ability to locate the damage initiation and damage propagation regions in the RVE.

One recent study by Nasution [93] employed asymptotic expansion homogenisation to calculate the thermo-mechanical properties of ORT using periodic boundary conditions and in-house FEM code developed in Fortran. Material properties obtained are validated against experimental measurments. Afterwards, localisation analysis is carried out to determine the micro-stress state of the individual constituents due to mechanical and thermal loads. Two mechanical loading states are applied to a cantilever beam model: uniaxial tension and bending. In both cases, thermal residual stresses are computed and superimposed on the mechanical stresses to determine the overall stress state for each constituent "warp, weft, binder and matrix". The combined thermal and mechanical stress for each constituent is divided by the strength in the corresponding direction. Damage criteria are set according to the normalised stress criteria. This study concludes that bending is more critical, for this type of composite archeticture, than uniaxial load. In addition, incorporating thermal stresses may change the damage mechanisms as it may accelerate damage initiation in some cases. As geometrical distortions play a vital role in determining the mechanical properties of 3D woven composites after manufacturing, Green *et al.* [94] employed the voxel method to generate a realistic unit cell model for ORT and compare results obtained with an idealised unit cell model. The proposed model accounted for the geometrical destortions due to the preform waviness and compaction during manufacturing. A continuum damage model was used to simulate damage evolution in ORT loaded in tension. However, the damage evolution laws were defined by penalty functions that degrade the elastic properties with two empirical constants that define how

fast damage propagates in a constituient. The study concluded that the idealised unit cell model overestimated the stress strain behaviour while the realistic model was in a better agreement with experimental data.

2.7 Concluding Remarks

From the literature review, the following conclusions can be drawn. Most of the research has concentrated on the out-of-plane characterisation of 3D woven composites for impact resistance applications. Hence, less work has focused on characterisation of the in-plane properties of 3D woven composites along the warp and weft directions. Moreover, very few attempts have investigated the off-axis in-plane response of 3D woven composites and the different z-binder architectures. For damage characterisation in 3D woven composites, using X-ray CT has been proven to be an effective NDT method. Thus, this study will concentrate on investigating the off-axis in-plane behaviour of different z-binder architectures of 3D woven composites in addition to characterising the level of damage using X-ray CT. Although ERM has been widely employed as a SHM technique for laminated and 2D woven composites, no work has been done to investigate its potential for damage detection in 3D woven composites; which is the second main focus of this research work. As challenges facing composite joint applications include, but are not limited to, the material ductility/yielding, notch insensitivity and high strain to failure, 3D woven composites loaded in the off-axis direction are being investigated as a potential proposed solution. On the simulation side, most of the modelling strategies available in literature rely on fitting parameters to simulate the experimental results, hence this study will try to propose a micro-mechanics based damage model that is defined by only a few material parameters and test the model against experimental results.

3 Manufacturing and characterisation of 3D woven composites

This chapter details the specifications of the materials used in this study in section 1. Section 2 presents the resin film infusion (RFI) process used to manufacture the 3D woven composite plates followed by the volume fraction analysis in section 3. Section 4 then describes the setup of X-ray computed tomography (CT) used to visualise the internal geometry of the "as-manufactured" 3D woven composites to quantify the geometrical distortions and imperfections associated with this manufacturing technique. Finally, section 5 summarises the main concluding remarks of the chapter.

3.1 Materials specifications

The carbon fibre, used in this study, is HexTow IM7 (Hexcel), while the epoxy is MTM 57 (medium temperature epoxy produced by Solvay). The 3D woven dry fabrics are produced by Sigmatex UK. The material properties available from the manufacturers for both IM7 and MTM57 are listed in Table 3.1. The reported tensile strength was obtained from tow test data that is why a difference is observed between the 12k and 6k values.

Table 3.1 Material properties of IM7 fibre and MTM57 resin

Material property	IM7 (12k)*	IM7 (6k)*	MTM57**
Tensile Strength (MPa)	5655	5515	140
Tensile Modulus (GPa)	276	276	3.35
Elongation at break (%)	1.9	1.9	N/A
Density (g/cm^3)	1.78	1.78	1.19
Poisson's ratio [95]	0.3	0.3	0.35

* Data obtained from product datasheet [96] except for the Poisson's ratio.

** Data obtained from [97].

Three architectures are investigated, namely orthogonal (ORT), layer-to-layer (LTL) and angle interlock (AI). Fig. 3.1 shows the schematic architecture of three 3D woven fabrics drawn using TexGen software.

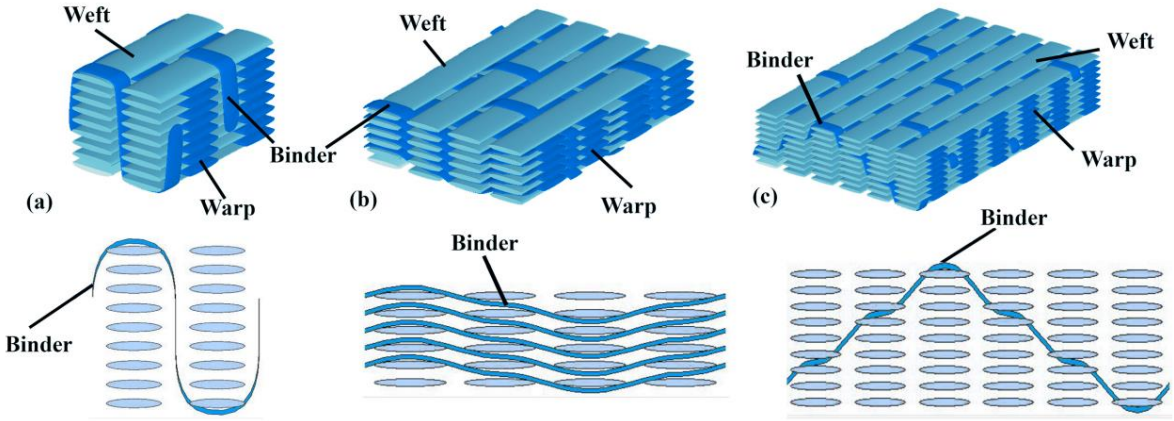

Figure 3.1 Schematics of 3D woven composites unit cells: (a) ORT, (b) LTL, (c) AI

Table 3.2 Specifications of textile architecture of 3D woven composites

Parameter	ORT	LTL	AI
Warp number of layers	8	5	8
Weft number of layers	9	6	9
Warp fibre count	12k	12k	12k
Weft fibre count	12k	12k	12k
z-binder fibre count	6k	12k	6k
Ends/cm (warp)	31.52	17.73	31.52
Picks/cm (weft)	38	36	34
Binders/cm (z-binder)	3.94	17.73	3.94
Areal density (g/m^2)	3353	3260	3044

Specification of the textile architecture parameters of 3D woven composites are detailed in Table 3.2. Warp and weft fibre count for ORT, AI and LTL is 12k. The z-binder fibre count for ORT, AI and LTL is 6k, 6k and 12k, respectively. The number of warp threads, weft threads and z-binder threads per unit length (centimetre) is specified in Table 3.2 as ends/cm, picks/cm and binders/cm,

respectively. In addition, the areal density of the dry 3D woven fabric is also given in Table 3.2 (unit is g/m^2). Architectures were manufactured to keep the areal density as close as possible for the three architectures but this led to a difference in the warp and weft volume fractions as shown in Table 3.2. This will affect the on-axis tensile results as it will be discussed in (Section 4.2).

3.2 Resin Film Infusion (RFI)

To produce 3D woven composite panels, the dry fabrics were infiltrated by MTM 57 epoxy matrix using the resin film infusion (RFI) process. Vacuum bagging infusion was chosen for its low cost compared to other available techniques as well as the convenience from the time point of view. A schematic diagram of the vacuum bagging assembly used for infusion is shown in Fig. 3.2. A polished steel tool plate 30 x 50 cm was cleaned and coated with three layers of release agent, with a time interval of five minutes between every coating and then left to dry completely at room temperature. While the tool plate was left to dry, the resin film was extracted out of the freezer and cut into the dimensions of the 3D woven fabric. The number of resin film layers required per a 3D woven fabric was determined as a function of the target fibre volume fraction and the areal densities of both the resin and the fabric. The areal density of the resin used is 319 gsm while the 3D woven fabric densities vary as reported in Table 3.1. After cutting the required number of resin layers, they are applied one by one and pushed against the bottom surface of the fabric. Once all the layers of resin had been applied to the pre-cut fabric, it was placed on the tool plate. A peel ply sheet of fabric was then put to cover the fabric top surface to facilitate the peeling-off process after curing and to make sure that the cured panel would not stick to the vacuum bag. Unlike the liquid resin infusion process, only one single spiral tube is required to act as a resin outlet. There is no need for an inlet tube as the resin is already enclosed in the vacuum bag. The spiral tube is sealed from one end with a sealant tape "tacky tape" while the other end is connected to the vacuum pump through an infusion tube. In order to completely seal the vacuum bag, tacky tape was

introduced on the perimeter of the tool plate and then a sheet of plastic bag is pushed against it.

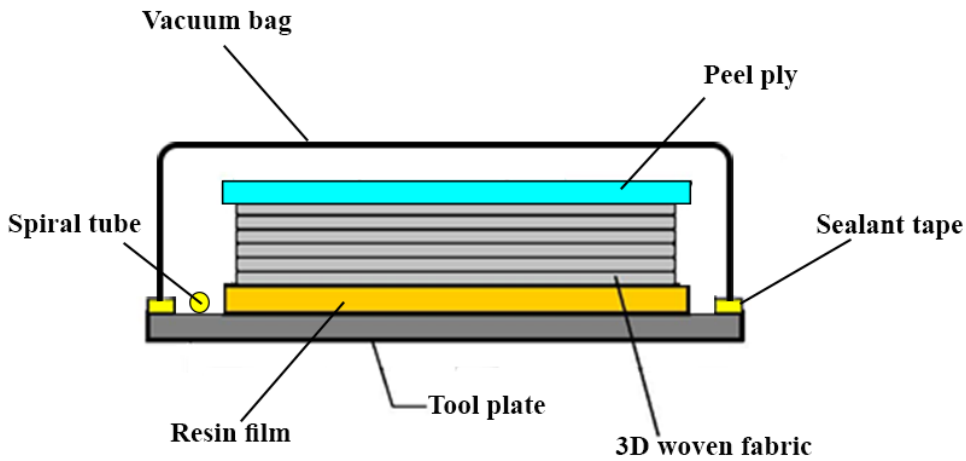

Figure 3.2 Schematic of the vacuum bagging technique

A vacuum level of (~760 mm-Hg) was applied; and then a gauge was attached to the vacuum valve and left for one hour to check for leakage as depicted in Fig. 3.3.

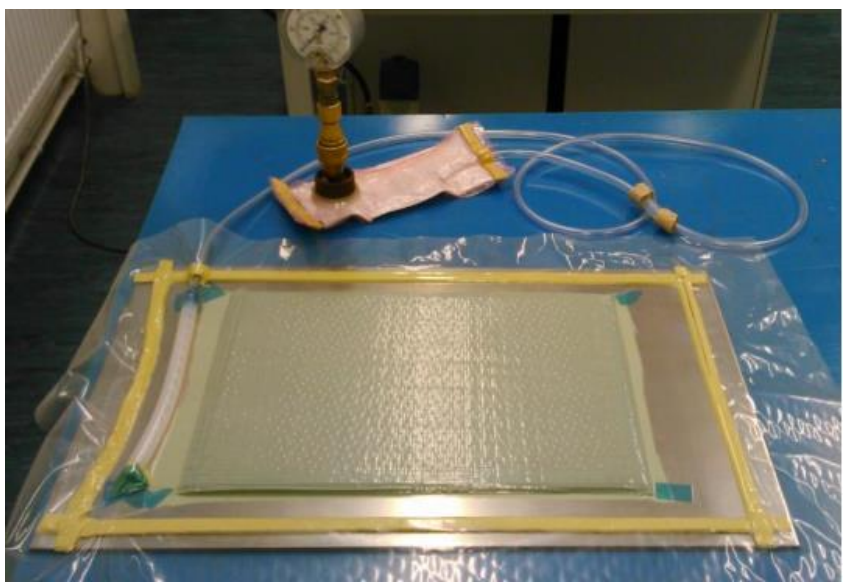

Figure 3.3 Vacuum bagging assembly attached to gauge to check the vacuum level and leakage

The infusion process was carried out under vacuum, according to the resin manufacturer specifications, at 70ºC for 1 h using a heating table, while the curing process was done at 120ºC for 1 h in a hot press with a cooling rate of 3º/min to 60º. The minimum curing pressure for MTM 57 was set to 2.8 bars (see Fig. 3.4)

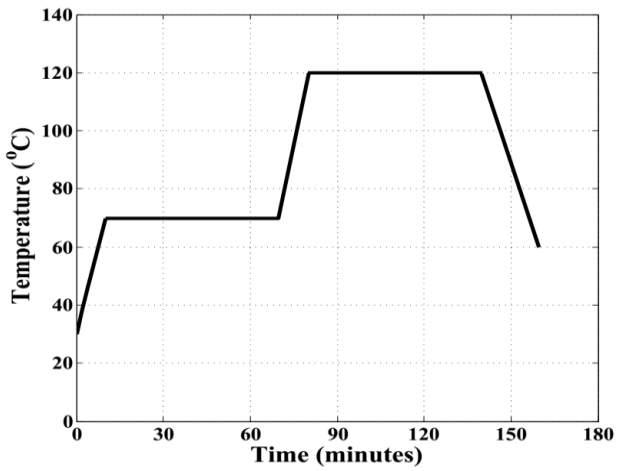

Figure 3.4 Diagram of infusion and curing cycle for MTM 57

Once the 3D woven composite panels with the size of 300 mm x 200 mm were cured, they were cut into three different orientations (see Fig. 3.5). The thickness of the cured composite panels ranges between 3.2 to 3.6 mm depending on the warp and weft number of layers.

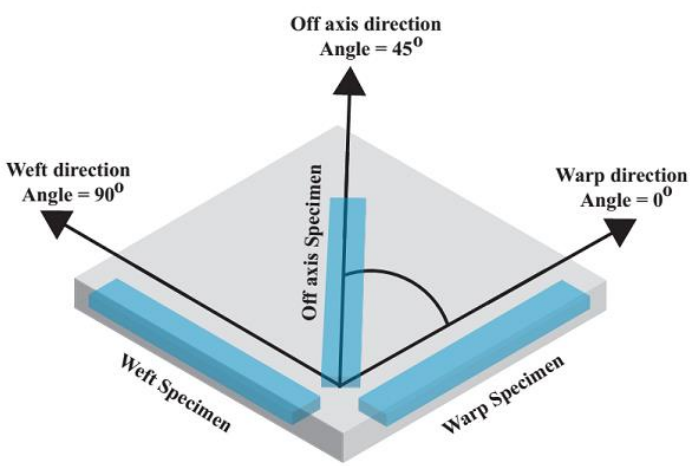

Figure 3.5 Cutting orientation to produce 3D woven composite specimens in warp, weft and bias (off-axis) directions

3.3 Volume fraction Analysis

In this study, the determination of fibre volume fraction of the manufactured panels was conducted in two stages. The first stage deals with an experimental measurement of the fibre volume fraction V_f (as well as the matrix V_m and the void volume fraction V_v) of samples from the manufactured panels. The second stage deals with an analytical calculation to determine directional V_f in the warp, weft and z-directions based on textile parameters given in Table 3.2. The procedures for both stages are described in the following sections.

3.3.1 Acid digestion

Fibre volume fraction measurement was conducted based on the acid digestion technique according to the ASTM D3171 standard (Constituent Content of Composite Materials). The procedure is generally described as follows: (i) specimen is immersed in the sulfuric acid where the matrix is entirely dissolved; (ii) weight of the specimen is measured before and after the digestion process. The measurement of fibre volume fraction by acid digestion also enables the measurement of the matrix volume fraction as well as the void content. The ASTM D3171 document provides detailed experimental and specimen's requirements.

3.3.2 Directional fibre volume fraction analysis

Directional fibre volume fraction analysis aims to calculate the fibre volume fraction in the warp, weft and z-directions, and to eventually determine the contribution of each set of directional fibre tows towards the overall V_f. The calculation of directional V_f can be summarised as follows: first, directional areal density of the fabric in the warp, weft and z-binder directions is calculated by multiplying the yarns' count (in tex) by the ends/cm, picks/cm and binders/cm, respectively. Second, the directional areal density is then normalised by the total areal density to determine the percentage of warp, weft and z-binder fibres (directional V_f).

3.3.3 Effect of z-binder on directional V_f

Table 3.3 shows the fibre, matrix and void volume fractions of 3D woven composites. LTL exhibits a higher V_f of 59.16% in comparison to other materials due to its higher amount of z-binder (12k). However, it is noteworthy that z-binders generally introduces a higher amount of void in 3D woven composites in comparison to 2D composites [10,13]. The architecture of the z-binder reduces the amount of resin that is flowing into areas between the warp and weft tows. This is also aggravated by the fact that the RFI process does not employ a transportation medium for resin to flow. In other words, Table 3.3 suggests that weaving architecture affects the void content "porosity" of the infused panel. AI architecture has a smoother weaving pattern as compared to ORT, while the LTL architecture has the smoothest weaving pattern among all the 3D woven investigated architectures. A smoother weaving pattern improves the resin flow between fabric layers and resin infiltration into the fabrics. As such, a smoother weaving pattern would have a lower void content. This explains the lower void content in the LTL materials. As also observed, the void content in AI is greater than the LTL, but less than that in ORT, which has the most complex weaving pattern and consequently the highest void content (see Section 3.4). The total fibre volume fraction given in Table 3.3 is then divided into warp, weft and z-binder content, and Table 3.4 shows the so-called directional V_f.

Table 3.3 Total volume fraction of constituents (fibre, matrix, void) in 3D woven composites

Constituent	3D woven composite		
	ORT	LTL	AI
Fibre (%)	51.35 ± 0.45	59.16 ± 0.24	55.4 ± 0.80
Matrix (%)	46.02 ± 0.43	39.21 ± 0.14	42.18 ± 0.97
Voids (%)	2.63 ± 0.02	1.63 ± 0.13	2.42 ± 0.19

Table 3.4 Directional fibre volume fraction in 3D woven composites

Direction of fibre tow	ORT	LTL	AI
Warp (%)	21.57	14.36	25.58
Weft (%)	26.00	29.15	27.59
z-binder (%)	3.77	15.65	2.22

Remark:

- The void content in the manufactured 3D woven composites is relatively high compared to "autoclave" produced composites for aerospace applications [10,13] in which the void content ≤ 1%. As previously mentioned, the manufacturing process of the 3D woven composite plates was an "out-of-autoclave" process using the hot press. However, this void content does not significantly affect the global tensile response of 3D woven composites as they are mainly fibre dominated (see Section 4.2).

3.4 X-ray Computed Tomography

An X-ray CT scan was performed on the orthogonal woven sample using a Zeiss Xradia VersaXRM-510. To obtain sufficient resolution, a square cross section of (30 mm x 30 mm) was cut from the sample. The 0.4x objective of the scanner was used. The total volume in the field of view was 10 x 10 x 10 mm^3, resulting in a voxel size of 5 µm. The source voltage and current were set to 40 kV and 75 µA respectively. The exposure time for each radiograph was 10s, with 1600 radiographs being collected over 360º. The total data acquisition time was 7 hours. After scanning, the 3D image (Fig. 3.6a) was reconstructed out of the 2D X-ray slices. To accurately capture the unit cell geometry, all dimensions, used to implement the model (Section 8.2), are measured from the X-ray CT images. Using a cutting plane along the warp yarns, the X-ray CT section view (Fig. 3.6b) clearly shows voids and binder distortion, due to the RFI process and fabric compaction, which is different from the idealised simulated geometry. The effect of simulating an idealised unit cell model is discussed in (Section 8.3).

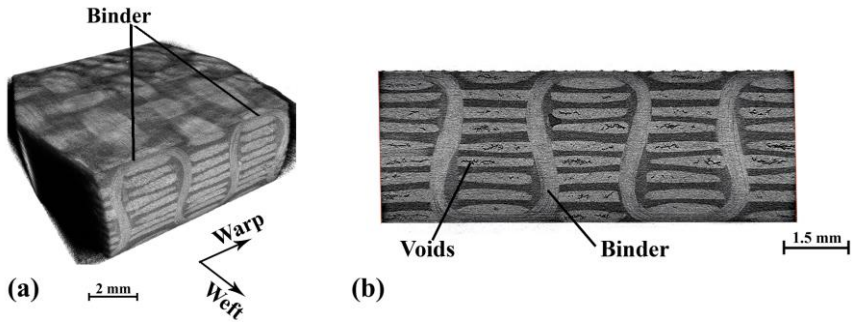

Figure 3.6 3D orthogonal woven composite: (a) unit cell reconstruction from X-ray CT scans, (b) cross-section view along the binder path

Similarly, all scanning parameters were kept the same for the layer-to-layer and angle interlock except for the total volume in the field of view and consequently the voxel size. As both the layer-to-layer and angle interlock have larger unit cells, the field of view was increased to 16 x 16 x 16 mm^3 and 25 x 25 x 25 mm^3 respectively. The layer-to-layer and angle interlock 3D scanned images after reconstruction are depicted in (Fig. 3.7a) and (Fig. 3.8a) respectively. Using a cutting plane along the warp yarns, X-ray CT section views (Fig. 3.7b) and (Fig. 3.8b) clearly show voids and binder distortion, due to the RFI process and fabric compaction, which is different from the idealised geometry. In the layer-to-layer architecture, the weft layers are distorted in the vertical plane and resin rich regions are shown in black.

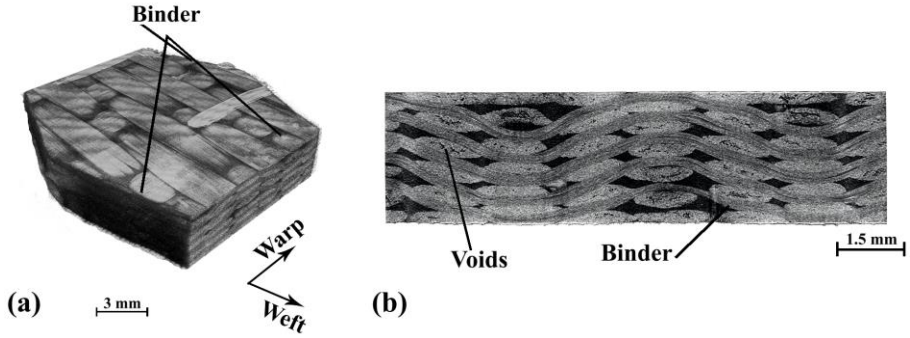

Figure 3.7 3D Layer-to-layer woven composite: (a) unit cell reconstruction from X-ray CT scans, (b) cross-section view along the binder path

Unlike the orthogonal and layer-to-layer architectures, the angle interlock architecture cross section (Fig. 3.8b) suggests that it has the most severe binder distortion.

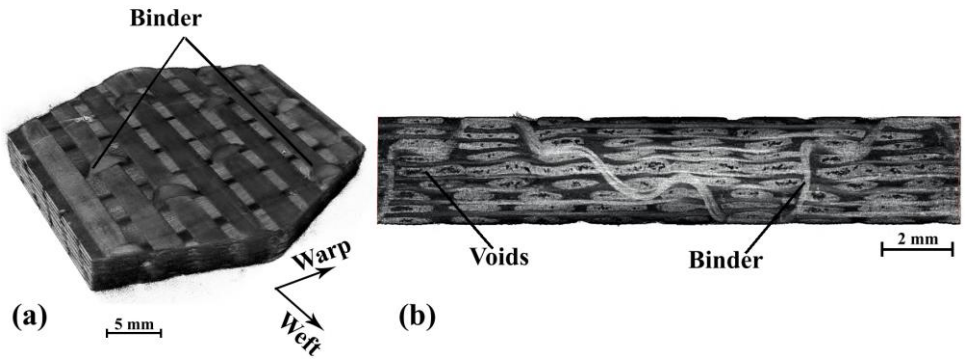

Figure 3.8 3D Angle interlock woven composite: (a) unit cell reconstruction from X-ray CT scans, (b) cross-section view along the binder path

3.5 Concluding Remarks

Three different architectures of 3D woven composite panels have been manufactured with the RFI process. Those architectures are (i) layer-to-layer (LTL), (ii) angle interlock (AI), and (iii) orthogonal (ORT). Characterisation of the manufactured panels was carried out via volume fraction analysis and X-ray tomography to capture the geometrical imperfections and manufacturing-induced distortions. The effect of the weaving architecture and binder path on the tensile properties of 3D woven composites, damage mechanisms and energy absorption is discussed in the next chapter.

4 Tensile Properties of 3D woven composites

This chapter is divided into six sections. Section 1 describes the mechanical tests (tensile tests coupled with digital image correlation analysis). Sections 2-5 present the results and discuss the experimental findings (effect of z-binder on stress-strain responses in on-axis and off-axis loading cases, their associated failure mechanisms and the energy absorption). Finally, section 6 highlights the concluding remarks of the analysis.

4.1 Mechanical Testing

4.1.1 Test specimens preparation

The testing panel (250 x 180 mm^2) was cut from the manufactured panels (300 x 200 mm^2) using a water-cooled diamond saw. This panel was then prepared for the tabbing process. Four pieces of tabbing material of (50 x 180 mm^2) were cut and sand blasted with a grit blaster. The same area of the tabbing material was blasted on the testing panel to roughen the surface for better adhesion with the end tabs. The tabbing material used, glass fibre reinforced polymer cut at 45° orientation, was consistent with D 3039 ASTM standards for "Tensile Properties of Polymer Matrix Composite Materials" to provide a soft interface. Both the testing panel and the tabbing material were then cleaned with running water, dried overnight in an oven and degreased by acetone immediately before bonding them. The tabbing adhesive used to bond the end tabs to the testing panel is a structural bonding adhesive (MTA240/PK13). For 1 hour at 120° and 3 bars of pressure, the tabbing process was accomplished using a hot press. Finally, rectangular specimens (250 x 25 mm^2) were cut from the tabbed panel with the rotary diamond saw, cleaned with running water and dried overnight in an oven at 70°.

4.1.2 Test Setup

The testing setup shown in Fig. 4.1a consists of two main data acquisition channels for load and displacement within an Instron 5882. Strains were acquired using a

digital image correlation (DIC) system utilising a SensiCam 12-bit CCD camera (PCO) with TC-2336 bi-telecentric lenses (The Telecentric Company) shown in Fig. 4.1a. The resolution of the CCD camera was 1376x1040 pixels. The bi-telecentric lenses have a depth of field of 11 mm, diameter of 61 mm and magnification of 0.234 x. Fig. 4.1b shows a typical speckle pattern on a specimen's surface. CamWare V3.11 software was used to capture the speckle pattern images acquired from the CCD camera.

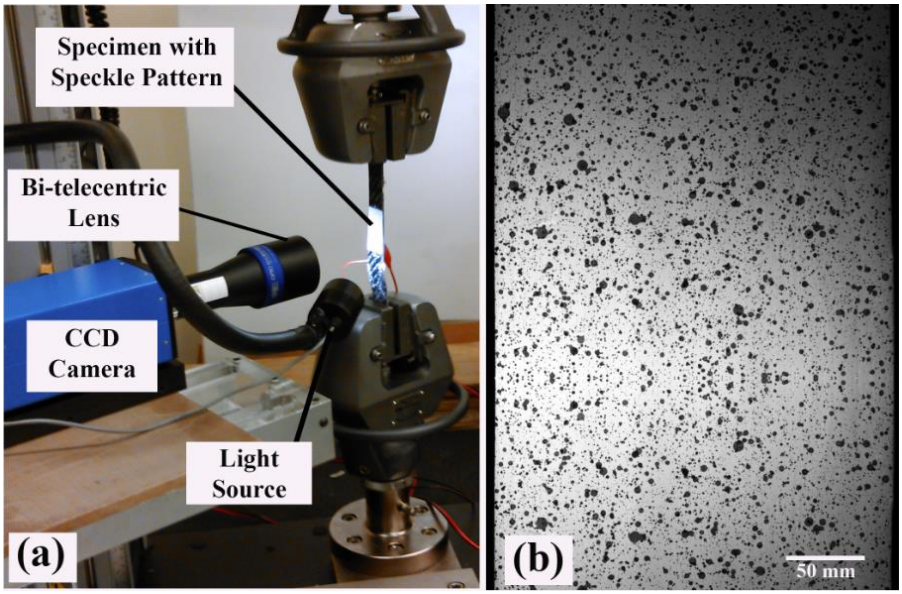

Figure 4.1 Experimental Setup: (a) testing setup, (b) speckle pattern used for DIC

Tensile testing was conducted in accordance to D 3039 ASTM standards for "Tensile Properties of Polymer Matrix Composite Materials" in a displacement controlled mode with a rate of 2 mm/min. Due to material limitations, at least three specimens were tested for each orientation (0º and 90º). All tests were performed in a controlled environment where the temperature was 21°C and the relative humidity (RH) was 45%. The speckle images were then processed using Vic 2D. In processing these images, the subset size was set to the value of 101 x 101 pixels; adequate for woven specimens [98,99]. In addition, the step size (distance between subsets) was set to 5 pixels. The observation window of approximately 25 x 22 mm^2 produced an image with dimensions of 1040x896 pixels.

Global mean values of strain (ε_{xx};ε_{yy};ε_{xy}) are obtained from DIC analysis using Vic 2D.

4.2 On-axis mechanical properties

The stress/strain curves for ORT, LTL and AI tested up to failure are shown in Fig. 4.2a-c, respectively. The stress/strain curves, either in the warp or weft direction, demonstrate good repeatability. The curves for ORT and LTL shown in Figs. 4.2a and Figs. 4.2b indicate that the specimens tested in the weft direction are stiffer than those tested in the warp direction (see Table 4.1). This is primarily due to the fact that ORT and LTL specimens have higher directional V_f in the weft direction than that in warp direction (see Table 3.4). When the directional V_f is similar between weft and warp directions, as in the case of the AI specimens, the tensile stress/strain curves along the warp and weft directions are similar (Fig. 4.2c).

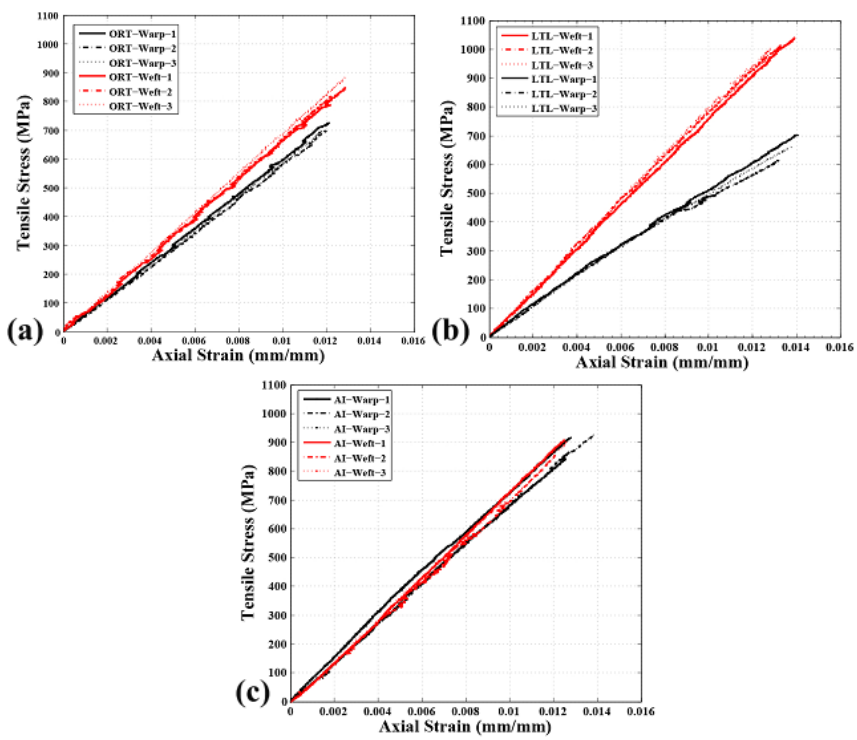

Figure 4.2 On-axis stress/strain curves: (a) ORT, (b) LTL, (c) AI

In the case of LTL architecture tested along the warp direction, a slight decrease in stiffness (see Figs. 4.2b) is observed beyond 0.5% strain. This may be attributed to premature fibre breakage at the interlacement points between the binder yarns and warp yarns where stress localisation is experienced on the micro-scale. This directly affects the macroscopic stiffness of the tested specimens. Based on the stress/strain curves shown in Figs. 4.2a-c, the mechanical properties (Young's modulus, tensile strength and failure strain) of 3D woven composites are given in Table 4.1.

Table 4.1 Young's modulus, tensile strength and failure strain of 3D composites in warp and weft directions

	Young's modulus (GPa)		Tensile strength (MPa)		Failure strain (%)	
	Warp (0º)	Weft (90º)	Warp (0º)	Weft (90º)	Warp (0º)	Weft (90º)
ORT	56.2±0.78	68.2±3.71	704 ± 14.78	849±26.14	1.19±0.01	1.26±0.03
LTL	53.5±0.92	75.8±1.67	660±43.64	1020±19.64	1.36±0.03	1.33±0.05
AI	69.1±3.84	68.5±2.83	873±80.52	894±61.35	1.31±0.05	1.24±0.02

Remarks:

- For the sake of comparison with Table 4.1, the rule of mixture was used to analytically calculate the stiffness of ORT, LTL and AI in both the warp and weft directions using the constituents' properties previously listed in Table 3.1. The calculated stiffness is always found to overestimate the experimental stiffness as it does not take into account the undulation of the weaving architecture.
- For a cross-ply laminate with the same total fibre volume fraction as the LTL architecture (~59.16%), the analytical calculated stiffness in the warp (~29.58%) and weft (~29.58%) directions is approximately 85.91 GPa with a strength of 1124 MPa which is found to be much higher than the values reported in Table 4.1.

The strain contour (ε_{yy}) obtained by the DIC system from the surface of ORT, LTL and AI specimens captured at ultimate stress is plotted in Figs. 4.3a-c.

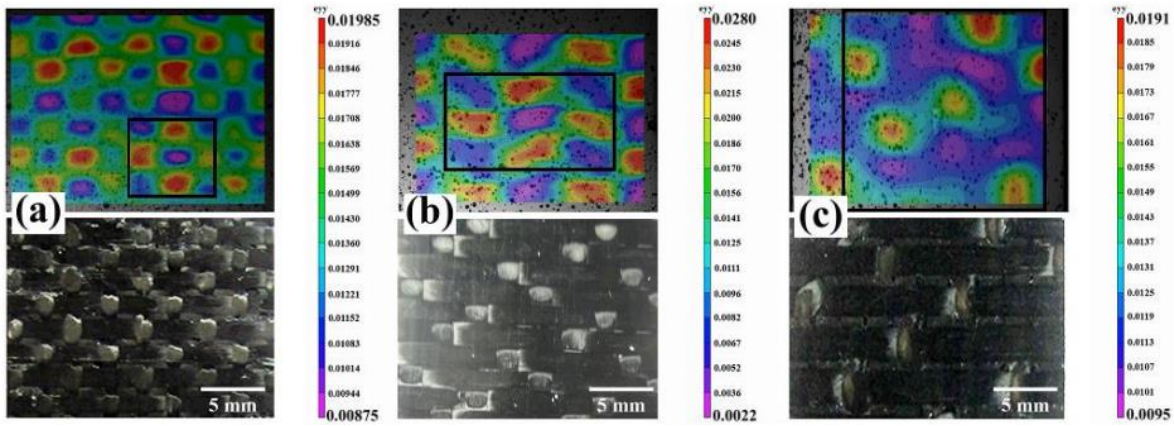

Figure 4.3 Strain contour ($\boldsymbol{\varepsilon_{yy}}$) obtained by the DIC system and unit cell representation in (a) ORT, (b) LTL, (c) AI specimens (note: the black frames show the respective unit cell)

A spectrum of colour map on the right side of each DIC image corresponds to the strain values. The region with high strain values is indicated with red colour, and this region is the interlacement points between the z-binders and the weft yarns. Although the conventional assumption that strain is homogenous over the gauge length of the loaded specimen, 3D woven composites clearly demonstrate variation of strain depending on the weaving and z-binder architectures. In addition, the strain contour obtained by DIC was also used to identify the unit cell of 3D woven composites based on the periodicity of the weaving pattern. Here, the dimension of the unit cell of ORT, LTL and AI specimens are identified to be approximately 5 x 5 mm^2, 10 x 7 mm^2 and 20 x 25 mm^2, respectively. The periodicity of the strain contours could be useful for validating the models of 3D woven composites utilising, for instance, the asymptotic expansion homogenisation method reported in [30,90,100,101].

4.3 Off-axis mechanical properties

Stress/strain curves of 3D composites loaded in the bias direction of 45° are shown in Fig. 4.4 where they show bilinear response. The "knee point" is defined as the transition point from the first to the second linear curve; and similarly to the angle ply laminate case reported by Fuller and Wisnom [102] this second linear curve is associated with matrix cracking and inter-yarn matrix delamination that leads to a gradual change of stiffness. As shown in Fig. 4.4, the failure strain of ORT, LTL and AI is 22.99%, 11.60% and 12.81% respectively. The z-binders affect the rotation of biased fibre tows, and eventually the strain hardening and failure onset of 3D woven composites. Table 4.2 summarises the tensile modulus, strength and failure strain which are derived from the off-axis stress/strain curves. Both AI and ORT demonstrate higher strength and strain to failure compared to LTL which suggests that a through-thickness binder improves the performance of off-axis loaded 3D woven composites compared to the layer-to-layer binder. Moreover, the effect of the z-binder yarns architecture is obvious when ORT is compared against AI. The failure strain of the ORT architecture is almost double the failure strain of the AI architecture. This suggests that the z-binder architecture "path" influences the damage evolution and the final failure of 3D woven composites. Thus, the following sections investigate in detail the effect of the z-binder architecture on the off-axis 3D woven composites' strength, damage mechanisms and energy absorption.

Table 4.2 Off-axis tensile modulus, strength and failure strain of 3D woven composites

Textile architecture	Tensile Modulus (GPa)	Tensile strength (MPa)	Failure strain (%)
ORT	7.91 ± 0.10	237.37 ± 1.60	22.99 ± 1.43
LTL	9.56 ± 0.73	135.73 ± 5.47	11.6 ± 0.23
AI	8.54 ± 0.56	173.30 ± 3.99	12.81 ± 0.97

Remarks:

1- For LTL and AI a necking region is developed that leads to final fracture. Before localisation, the measured strain is considered as a good estimation of the developed strain. However If localisation occurs outside the region of interest (ROI) of the DIC, the strain measured might not be accurate. The dashed line on Fig. 4.4 indicates the value after which the strain measurement might not be valid.

2- Approaching the point of failure in off-axis samples, several fibre bundles ruptured from the specimen surface within the DIC region, which caused some of the speckle pattern to debond. This might have an effect on determining the ultimate failure strain which is reported in Table 4.2. In this study, for the determination of failure strain, it was decided to select the point at which the strain value has not yet being disturbed. Unfortunately, conventional strain gauges bonded on the specimen or non-contact strain measurement methods, such as video extensometers, would suffer from the same problem.

3- For the sake of comparison with Table 4.2, $(+45/-45)_{5s}$ a laminate was manufactured and tested, in-house, in quasi-static tension. With a fibre volume fraction V_f of 52.93%, the mean values for the tensile modulus, tensile strength and failure strain were 10.01 GPa, 204.2 MPa and 10.22% respectively. It is obvious from the comparison that the modulus of the laminated composite is higher than all the 3D woven architectures which can be attributed to the undulating nature of the reinforcement fibres; however, the strength and failure strain of the ORT architecture still exceed their 2D laminated counterparts. Thus, the overall energy absorption (see Section 4.5) of the ORT architecture would be the highest among both 3D woven and 2D laminated composites.

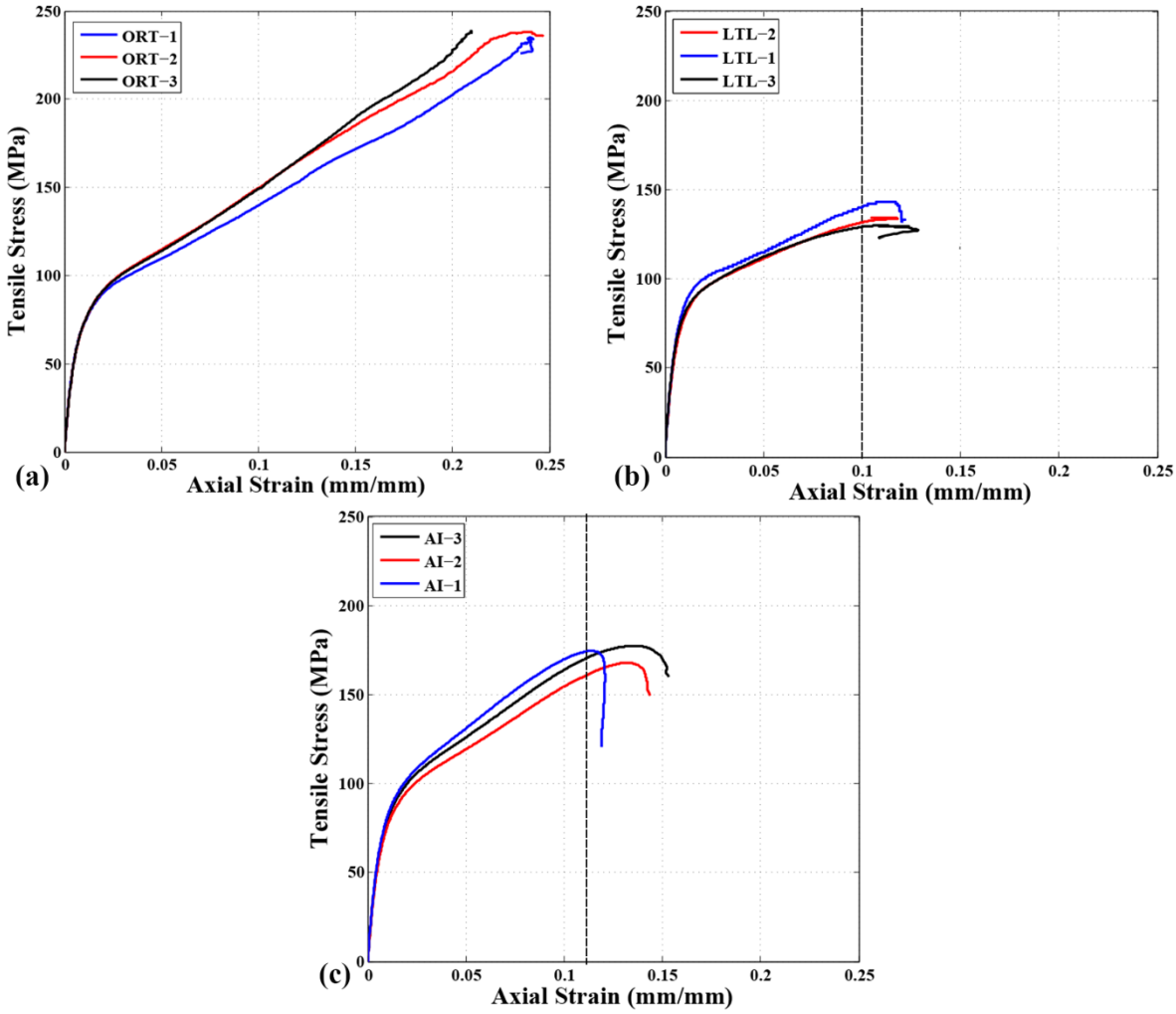

Figure 4.4 Off-axis stress/strain curves: (a) ORT, (b) LTL, (c) AI

4.4 Failure mechanisms

Macroscopic failure of 3D woven composites tested on-axis is shown in Fig. 4.5. The failure is characterised by a clear transverse fracture (perpendicular to the loading direction) across the whole width of the specimens. This indicates that the final fracture is predominantly due to longitudinal fibre breakage. In terms of failure mechanisms, damage initiation and progression up to final failure in on-axis 3D woven composites has been reported by a number of researchers in [24,44,101,103]. The damage initiation and progression were found to be similar for orthogonal, layer-to-layer and angle interlock architectures. The damage typically

starts at the interlacement points between the z-binder and the warp (or weft) yarns where the local stress fields are amplified. Following the stress localisation at the interlacement points, transverse cracks within the yarns, perpendicular to the loading direction, grow instantaneously and multiply in number up to a saturation point. Then, the damage mechanism changes from transverse cracking to delamination (between warp and weft yarns and along the z-binder boundary), and this transition happens at the last stages of loading prior to fibre/tow breakage.

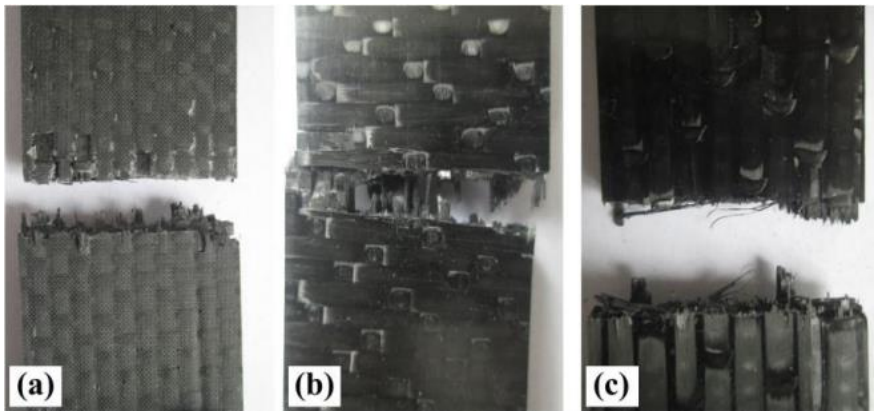

Figure 4.5 On-axis failure mode in (a) ORT, (b) LTL, (c) AI

Since the study of damage initiation and progression in off-axis 3D woven composite is very limited, here an interrupted test (at several load levels) was performed on the three architectures, and the underlying damage mechanisms were observed by X-ray machine (X-Tex XTH 225 cone-beam tomograph). The scanning spatial resolution was approximately 16 µm; and a diodomethane dye-penetrant (from Sigma Aldrich) was applied on the surface of specimens for one hour prior to scanning. Three stress levels (Points B, C, D) from the off-axis stress/strain curve of 3D woven composites were selected (see Fig. 4.6). The region of interest (ROI) for this observation is the centre of the specimen. Point A denotes zero stress where a non-damaged specimen was captured by X-ray as a reference. The strain level of the "knee point" in the off-axis tensile curves (and the corresponding tensile stress) of ORT, LTL and AI are given in Table 4.3.

Table 4.3 Strain and stress levels at the "knee point" for off-axis tensile test

Textile architecture	Axial strain (%)	Tensile stress (MPa)
ORT	1.84 ± 0.19	88.91 ± 2.80
LTL	1.45 ± 0.03	90.88 ± 2.58
AI	1.71 ± 0.16	94.70 ± 0.86

Point B was selected at the linear elastic segment (approximately 60 MPa) in order to characterise the damage initiation before the "knee point". Point C was around 110 MPa, which is a point after the knee point where damage progression was investigated. Point D was selected just before the specimen failure (around 95% of UTS), where the damage prior to failure was studied. The stress level for Point D was different for three architectures due to different UTS: the stress level is 210 MPa, 120 MPa and 170 MPa for ORT, LTL and AI specimens, respectively. X-ray images were captured with an X-ray setting of 35 kV and 310 µA. To aid the damage analysis using X-ray, nomenclature of damage types is given in Table 4.4.

Table 4.4 Nomenclature of damage types in off-axis tension test

Code	**Damage type**
F	Free edge matrix crack between yarns
Z	Z-binder induced damage
T	Transverse crack within yarns
D	Inter-yarn matrix delamination
S	Slippage between in-plane tows "warp/weft"

At Point A, no damage due to manufacturing is observed by X-ray. After the specimen was loaded to 60 MPa, the first damage characteristic at Point B observed in all architectures is free-edge matrix cracking (F-type). Damage at Point B is caused by the interlaminar stresses between layers as reported by a number of researchers in [104–106] due to the free-edge effect. Increasing the

applied stress, F-type cracks propagate towards the centre of the specimens. Reaching Point C, three damage types are identified. ORT and AI specimens exhibited binder-induced damage (Z-type) at the interlacement points between the in-plane yarns and the binding yarns. Transverse cracking (T-type) within yarns starts to multiply in number associated with inter-yarn matrix delamination (D-type). The (D-type) damage is driven by the in-plane yarns realignment and rotation towards the loading axis (see Section 4.5). In the case of the LTL specimen, accumulation of the (D-type) cracks is more severe as it has the least strength (~130 MPa) while no Z-type damage can be observed. Up to this stress level, there is no significant difference in the damage mechanisms between the three architectures. However at Point D (~95% UTS), the damage accumulation and evolution changed dramatically. In the ORT specimen, D-type cracks are arrested by the z-binder yarns while (T-type) cracks multiply in number. In ORT specimen, damage is uniformly distributed over the ROI. In the LTL and AI specimen, a different type of damage takes place, namely the slippage between in-plane yarns (S-type) that leads to an extensive localised damage which directly results in the reduction of the specimen's width.

The next step is to investigate whether the damage is homogenously distributed over the full gauge length of the specimen or not. So, three ROIs (top, centre, and bottom) of the specimen were scanned by X-ray, and "stitched" together as shown in Fig. 4.7. Three scans at different regions were carried out to maintain good image resolution. The horizontal lines seen in the X-ray images are the marking lines made to ensure correct transition for image stitching. Table 4.5 summarises the sequence of damage in the off-axis loaded specimens highlighted by this X-ray analysis.

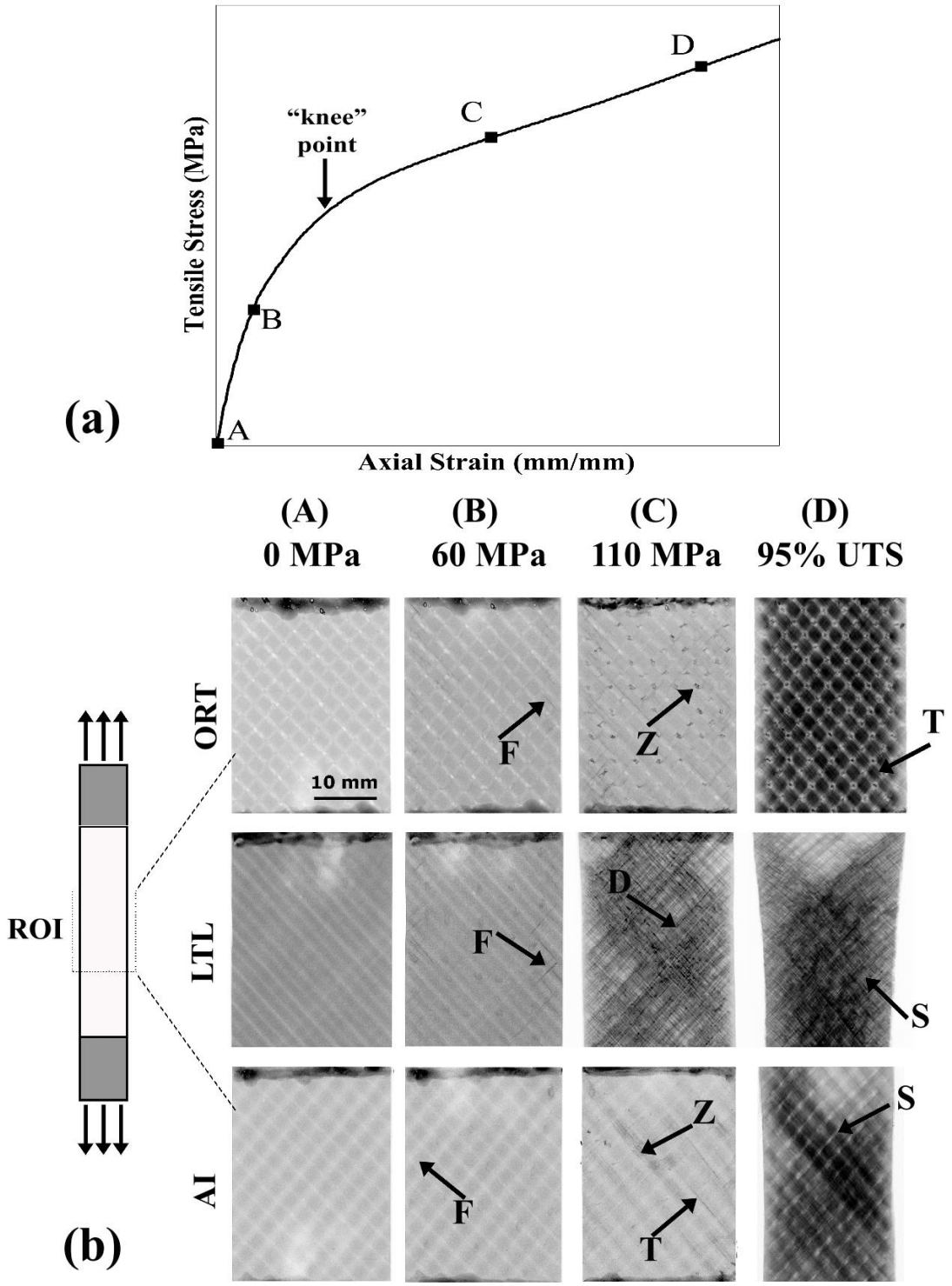

Figure 4.6 (a) Stress levels (Points A, B, C, D) in the off-axis stress/strain curve selected for damage observation by X-ray, (b) X-ray images of ORT, LTL, AI specimens at specified points

At 210 MPa (95% of UTS), as ORT specimen has smaller unit cell size than LTL and AI, this enables stress redistribution over a longer span of the specimen, and prevents the slippage between in-plane yarns. Thus, the damage in ORT is seen to be uniformly distributed all over the gauge length of the specimen. In contrast, both LTL and AI specimens exhibited localised damage due to S-type damage and extensive inter-yarn delamination. This is actually reflected in the global failure as shown in (Fig. 4.8). The ORT specimens broke into two separate parts (Fig. 4.8a) with an angled fracture where breakage of the z-binders is evident around the fracture area. Failure of the LTL and AI specimens shown in Figs. 4.8b and Figs. 4.8c, respectively, occurred in localised region that is characterised by angled fracture. No apparent ply separation was found in the LTL or the AI specimen as the z-binder yarns prevented the separation between the warp and weft layers.

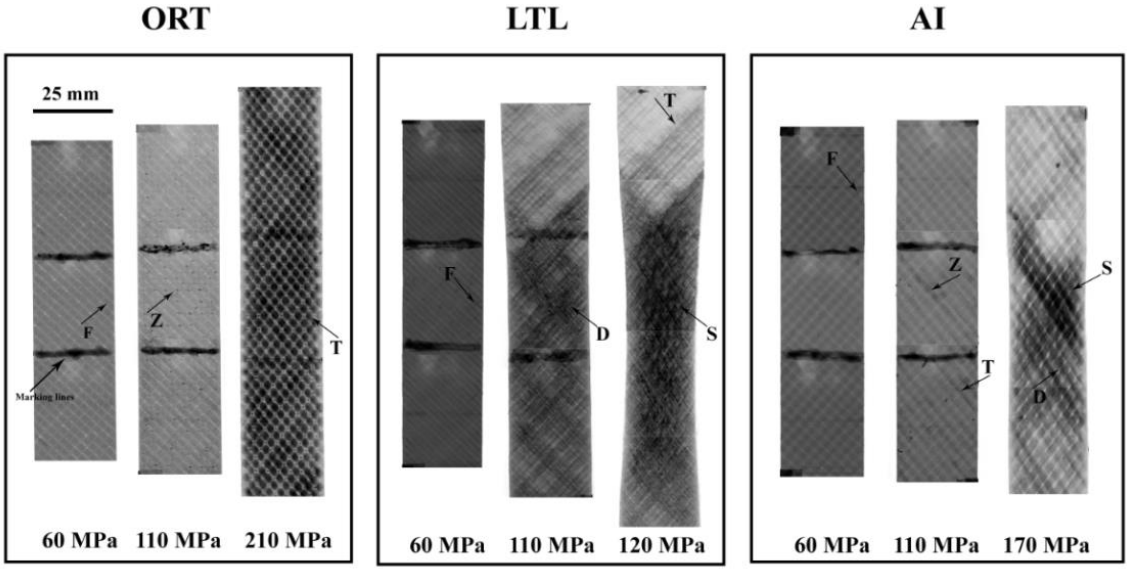

Figure 4.7 Stitched X-ray scans for the interrupted test

Table 4.5 Sequence of damage events during tensile loading of off-axis 3D woven composites

Point	Applied stress (MPa)	ORT	LTL	AI
A	0	--	--	--
B	60	F	F	F
C	110	F,T,Z	F,T,D	F,T,Z
D	95% UTS (210, 120,170)	F,T,D,Z	F,T,D,S	F,T,D ,Z,S

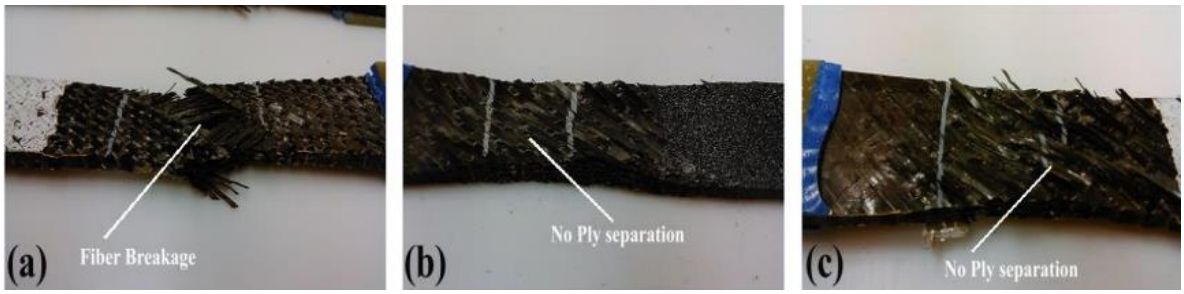

Figure 4.8 Off-axis failure mode in (a) ORT, (b) LTL, (c) AI

To further understand the underlying damage mechanisms, the failed specimens were X-ray scanned at different locations, i.e. close to the fracture region and away from it. After reconstructing the 3D scanned volumes, cross-sectional slices parallel to the binder plane "rotated 45º from the loading direction" were extracted (see Fig. 4.9). The three different locations were chosen in a systematic manner to show the damage in regions where there is no binder (Fig. 4.9a), with binder (Fig. 4.9b) and close to the fracture region (Fig. 4.9c). The ORT scans show extensive transverse cracking homogenously distributed across the width of the specimen (Fig. 4.9a). In regions where the binding yarns exist (Fig. 4.9b), no inter-yarn delamination is observed as opposed to regions where there are no binding yarns (Fig. 4.9a). In addition, localised damage (Fig. 4.9b) occurs due to binder interlacing with weft/warp yarns. Final failure happens when the binding yarns fracture (Fig. 4.9c) followed by extensive delamination. For the LTL architecture, transverse cracking and delamination, between warp and weft layers (Fig. 4.9a),

spans the whole width of the specimen. In regions with binding yarns, delamination is guided by their path (Fig. 4.9b). Close to the fracture region, the slippage (Fig. 4.9c) between planes and ply separations due to binder breakage characterises the damage mechanism resulting in final failure. In the case of AI architecture, multiple transverse cracking (Fig. 4.9a, b) is observed in the in-plane yarns "warp/weft" with inter-yarn delamination (Fig. 4.9a-c). Localised induced damage (Fig. 4.9b) due to binder interlacement is clear in the form of matrix cracking. When binding yarns break, ply separation, between warp and weft planes, is observed (Fig. 4.9c) leading to final failure of the specimen.

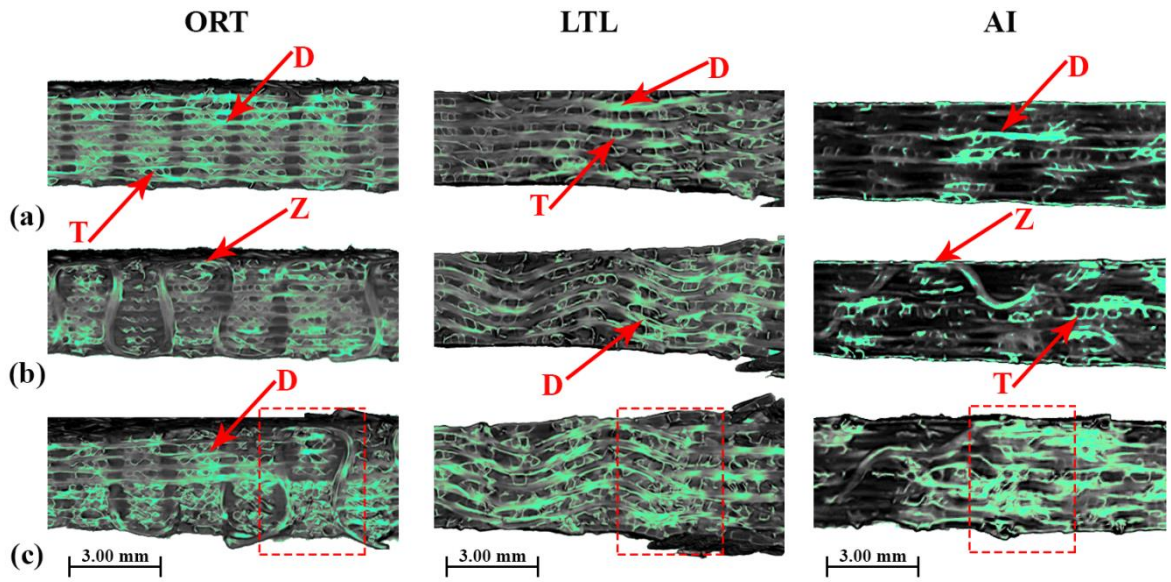

Figure 4.9 Off-axis X-ray cross-sectional slices in planes (a) without binder, (b) with binder, (c) close to the fracture region

4.5 Energy absorption

The energy absorbed per unit volume up to fracture (in MJ/m^3) is calculated as the area under the stress/strain curve. The energy absorption of 3D woven composites with different z-binder architectures is shown in Fig. 4.10. It is clear that the specimens loaded in the off-axis direction demonstrate greater energy absorption in comparison with their on-axis counterparts. More importantly, the z-

binder architecture has a significant effect on the energy absorption of the off-axis loaded specimens. Under off-axis loading, the ORT architecture absorbs energy almost three times higher than other 3D architectures. Furthermore, the ORT specimens loaded in the off-axis direction absorbs energy five times higher than those loaded in the on-axis direction. This suggest the following: (i) based on energy absorption criterion, all 3D woven composites perform better under off-axis rather than on-axis loading; (ii) among all 3D woven composites investigated here, the ORT performs the best in terms of energy absorption under off-axis loading. These findings can be used for the analysis of composite structures which may employ 3D woven composites for better response under multi-axial loading and impact resistance, where energy absorption is of prime interest.

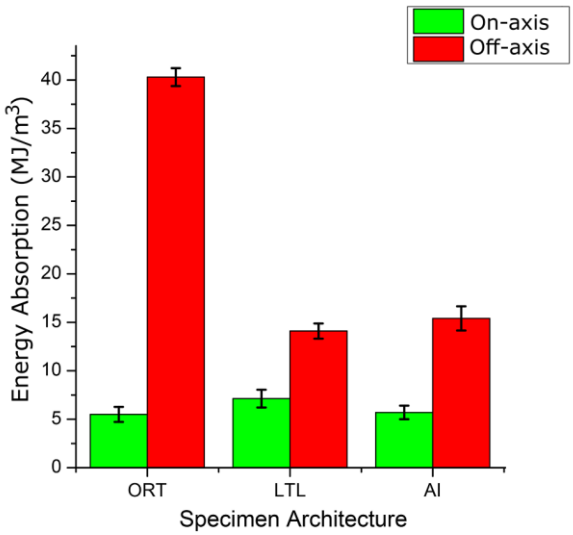

Figure 4.10 Energy absorption of 3D woven composites

When 3D woven composites are subjected to off-axis loading, the warp and weft yarns that are biased with a certain angle tend to reorient towards the principal loading axis. During the reorientation process, the so-called "scissoring effect" takes place between the warp, weft and binder yarns. This reorientation process allows further strain to be borne by the composite laminate and consequently energy absorption. Table 4.6 shows the rotation angles of the 3D woven composites measured experimentally at 95% UTS of the different specimens.

Table 4.6 Experimental rotation angles for off-axis specimens at 95% UTS

Parameter	ORT	LTL	AI
Exp. Rotation angle (deg)	12.07 ± 0.12	7.93 ± 0.49	5.43 ± 0.73

The ORT specimens exhibit the largest rotation angle as compared to other specimens indicating that the orthogonal z-binder coupled with small unit cells provides the best interlocking mechanism for in-plane yarns. The interlocking mechanism, with high fibre rotation angle at failure as exemplified by the ORT 3D woven composites, improves their shear performance (failure strain and energy absorption) compared to other woven architectures.

4.6 Concluding Remarks

Three different architectures of 3D woven composites (orthogonal, ORT; layer-to-layer, LTL; angle interlock, AI) were characterised in terms of on-axis and off-axis mechanical properties and the influence of the z-binder. Several remarks can be made from present investigation. The z-binder affects void content in 3D woven composites since the amount of resin flowing between warp and weft tows is partly inhibited by the binders; in this case, orthogonal architecture induces the highest amount of void in comparison to other architectures. Regardless of the weaving architecture type, the stiffness and tensile strength of 3D woven composites under on-axis loading mainly depends on the directional fibre volume fraction of the warp and weft yarns. Among all textile architectures, 3D orthogonal woven composites exhibit the best performance (highest failure strength and failure strain) under off-axis loading due to the interlocking mechanism provided by z-binder. This interlocking mechanism increases the rotation angle of the warp and weft yarns, and thus the ability of the yarns to bear extensive off-axis strain. Moreover, as the ORT specimen has smaller unit cell size, this enables stress redistribution over a longer span of the specimen, and prevents slippage between in-plane yarns. So, the

damage is uniformly distributed all over the gauge length of the specimens. The 3D orthogonal woven composites exhibit the highest energy absorption among other architectures during off-axis loading, which paves the road for their use in composite structures designed with an energy absorption criterion as well as impact performance. Investigating the potential of using the Electrical Resistance Monitoring (ERM) technique for detection of damage initiation and progression in 3D woven composites follows in the next chapter.

5 Electrical resistance monitoring for damage detection in 3D woven composites

This chapter is divided into four sections. Section 1 introduces some of the previous research work related to damage detection in composite materials and the application of electrical resistance monitoring. Section 2 describes the specimens' preparation process and the testing setup (tensile test coupled with digital image correlation and four-probe electrical analysis). Section 3 details the results and discusses the significance of the experimental observations (effect of z-binder on the initial resistance, damage resistance correlation for on-axis and off-axis tested specimens as well as residual plasticity and piezo-resistivity in off-axis monotonic and cyclic tests). Finally, section 4 summarises the main concluding remarks of the chapter and discusses the limitations of the proposed technique.

5.1 Introduction

For decades, damage detection and characterisation has been a challenge in 2D laminated composites because of its complex nature. There are various damage mechanisms in 2D laminated and woven composites which can be grouped into intra-laminar damage (i) diffused damage [107], (ii) transverse cracking [108–110], (iii) local delamination [111–113], (iv) fibre breakage [114,115] and inter-laminar damage which is mainly delamination between plies/yarns [24,44]. Detecting damage in 3D woven composites is rather more complicated as the z-binding yarns also contribute to the damage initiation and development [11,20,24,44,116]. Due to interlacement between the z-binding yarns and the in-plane yarns, stress concentration leads to premature localised damaged at those regions. In addition, the inter-laminar delamination is guided by the path of the z-binding yarns. Having a reliable real-time damage detection technique is essential for monitoring the integrity of 2D laminated and 3D woven composites in service especially for the non-visible damage that may lead to catastrophic failure. Structural Health Monitoring (SHM) techniques such as ultrasonic [117], optical fibres [118], acoustic

emission [119] and lamb waves [120,121] have been widely used for damage detection in composites. However, most of those techniques are relatively expensive and require skilled personnel. One alternative method for monitoring damage, particularly in carbon based composites, is by measuring electrical resistance change due to damage accumulation. Electrical resistance monitoring of unidirectional composites [52,55,60] during monotonic and cyclic "load/unload" tensile testing have proved the potential of this technique in detecting and tracking damage evolution in carbon based composites. Correlating different damage mechanisms (matrix cracking, transverse cracking and fibre breakage) with the change in resistivity [52,61,122–124] as well as negative piezo-resistivity due to fibre alignment was detailed in [52,61,125]. Damage monitoring as a function of resistance change has been extended to delamination detection in flexural testing by Abry *et al.* in [60,61]. Moreover, Todoroki and Berry [126,127] have reported successfully using electrical resistance monitoring for damage detection in 2D woven composites.

To date, the feasibility study of electrical resistance measurement in 3D woven composites has not been realised. To the best of the author's knowledge, no correlation has been made between damage and electrical resistance in 3D woven composites. There is a need to have a well-defined and reliable interpretation of the level of damage based on the electrical resistance in 3D woven composites. Thus, this research work extends the well-established damage detection and correlation using electrical resistance monitoring for 2D laminated composites to 3D woven composites. The idea is to provide a systematic strategy (as well as limitation, if any) for detecting damage using electrical resistance variation in 3D woven composites under monotonic and cyclic loading. Three types of 3D woven architecture are investigated here: (i) orthogonal (ORT), (ii) layer-to-layer (LTL) and (iii) angle interlock (AI). Those materials are loaded in tension along (i) warp (0°), (ii) weft (90°) and bias (45°) directions. Global stress/strain curves are evaluated along with resistance variation due to damage initiation and accumulation. For the off-axis loaded specimens, both monotonic and cyclic

"load/unload" tests are carried out to evaluate the piezo-resistivity effect and residual plasticity.

5.2 Test specimen preparation

Test specimens (250 mm x 25 mm) were cut from the manufactured panels after a tabbing process utilising glass/epoxy laminates. Afterwards, bonding of electrodes on the specimen was carried out. Four regions (5 mm wide) in the specimen were polished with sandpaper (320 grit size), cleaned using acetone and treated with concentrated sulfuric acid to expose the fibres and ensure a good contact between electrodes and specimen [128]. Silver paste layers were introduced over the treated regions. Finally, conductive silver epoxy was used to bond copper wires onto the specimen surface. As depicted in Fig. 5.1, four probes were introduced to evaluate the resistance variation over the span of 70 x 25 mm^2 of the specimens during testing. Two outer electrodes were used to induce the current (I) while the voltage (V) difference is measured by two inner electrodes. An Agilent U2741A 5.5 Digital Multi-meter was used to record the resistance. Average initial resistance for various specimen types before testing is reported in Section 5.3.1.

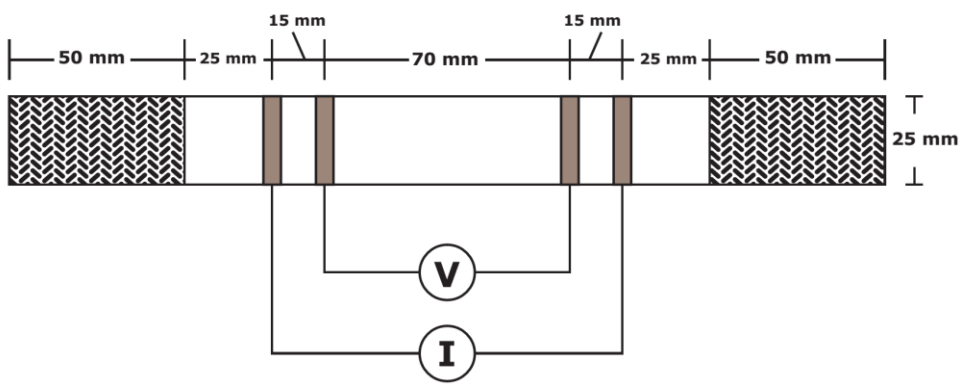

Figure 5.1 Schematic of the electrodes position on a testing specimen

5.2.1 Monotonic testing

Monotonic tensile testing was carried out on on-axis (warp, weft) and off-axis (45º) specimens of LTL, AI and ORT until the specimens failed. An Instron 5882 with a

100 kN load cell was used to apply a displacement-controlled tension with a loading speed of 2 mm/min according to ASTM D3039 standard (Tensile Properties of Polymer Matrix Composite Materials). Due to material limitation, three specimens were tested for each type (ORT, LTL and AI) and each orientation (0°, 90° and 45°). All tests were performed in a controlled environment where the temperature was 21°C and the relative humidity (RH) was 45%. Fig. 5.2a consists of two main data acquisition channels for load and displacement within the Instron 5882. Strains were acquired using the digital image correlation (DIC) system utilising a SensiCam 12-bit CCD camera (PCO) with TC-2336 bi-telecentric lenses (The Telecentric Company) shown in Fig. 5.2a. The resolution of CCD camera was 1376 x 1040 pixels. The bi-telecentric lens has a depth of field of 11 mm, a diameter of 61 mm and a magnification of 0.234 x. CamWare V3.11 software was used to capture the speckle pattern images acquired from the CCD camera. A Similar setting has been successfully used for 3D woven composites, and proven to provide reasonable quality of strain fields for 3D composites [99,129]. The frame rate is set as 0.5 and 0.33 frames per second (fps) for on-axis and off-axis tensile testing, respectively. The main reason for the lower fps in off-axis tests is that the deformation up to failure in off-axis specimens is much larger than that in on-axis tests. The speckle images were then processed using Vic 2D. In processing these images, the subset size was set to the value of 101 x 101 pixels, sufficient for woven composite specimens. In addition, the step size (distance between subsets) was set to 5 pixels. The observation window of approximately 25 x 22 mm^2 produced an image with dimensions of 1040 x 896 pixels. Global mean values of strain (ε_{xx};ε_{yy};ε_{xy}) are obtained from DIC analysis using Vic 2D. During testing, voltage was simultaneously recorded from the two inner probes (out of four probes) shown in Fig. 5.2b to calculate the resistance.

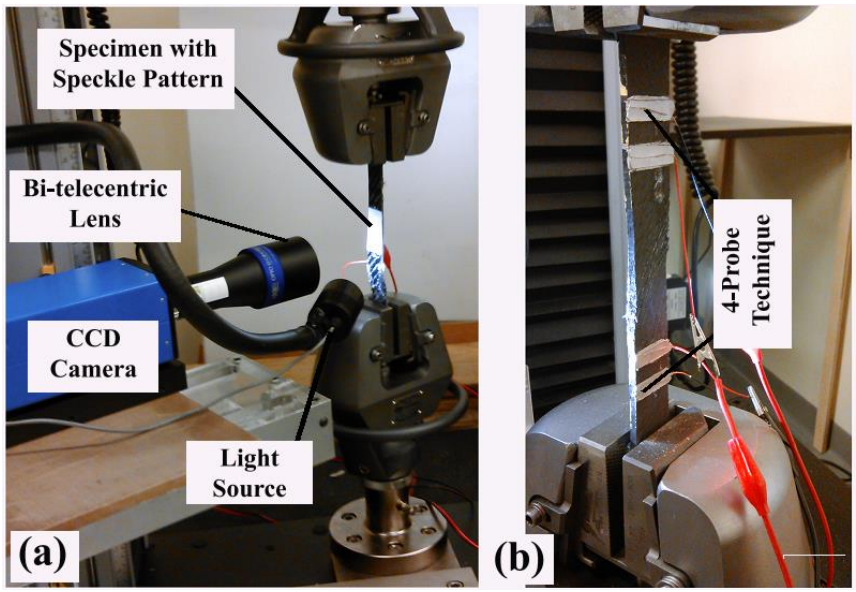

Figure 5.2 (a) Experimental setup for tensile test, (b) 4-Probe technique for resistance monitoring

5.2.2 Cyclic testing

Cyclic (load/unload) testing was conducted on off-axis specimens to evaluate residual plasticity and damage evolution and their effect on resistance variation in 3D woven composites. The loading rate was kept at 2 mm/min during cyclic loading. Five loading/unloading cycles were applied on the specimen, and the maximum displacement for each cycle (from 1st to the 5th cycle) was 4, 8, 12, 16 and 20 mm, respectively. The minimum load during each unloading cycle was set at 100 N to avoid compression of the specimen.

5.3 Results and discussion

5.3.1 Initial resistance measurement

To ensure that the measured resistance values were not just surface measurements, eight electrodes were bonded; four electrodes on each side of the specimen, and the resistance of each surface were evaluated. For all the tested specimens, the resistance obtained by injecting the current on one side “top or bottom” was found to be similar to the one measured by injecting the current on both sides

simultaneously. Such resistance similarity indicates that the resistance value determined by the 4-probe technique on one surface is a representative volumetric resistance and not just a surface measurement which is attributed to the through-thickness binding yarns creating a conduction path between the top and bottom surfaces. Then, using the 4-probe technique only on one surface, the initial resistances of 3D woven specimens were measured before applying any mechanical loads. Table 5.1 details the measured resistance values of off-axis and on-axis specimens. The initial resistance values can be used as a baseline measurement. The influence of the z-binder yarn architecture on the resistance values can also be investigated based on the initial resistance.

Table 5.1 Initial resistance for tested architectures in ohms (Ω)

Architecture	Off-axis	On-axis	
	45°	Warp (0°)	Weft (90°)
ORT	0.094 ± 0.012	0.08 ± 0.001	N/A
LTL	0.11 ± 0.001	0.076 ± 0.004	0.07 ± 0.005
AI	0.129 ± 0.008	0.065 ± 0.001	0.085 ± 0.002

It is clear that for on-axis specimens, all 3D woven architectures have lower resistance values compared to the off-axis ones which is typically due to the yarns' orientations being along the longitudinal fibre direction, either warp or weft, rather than the 45° direction. Moreover, the resistance of off-axis specimens seems to be a function of the unit cell size or the density of the binding yarns. ORT specimens have the smallest unit cell of 5 x 5 mm^2, while both LTL and AI have larger unit cells of 10 x 7 mm^2 and 20 x 25 mm^2, respectively. As ORT architecture has the z-binder going from top to bottom and then top again in a shorter length, its off-axis resistance is less than the LTL and AI architectures in which the z-binder yarns complete a full cycle over a wider area "longer length" of the composite. The z-binder yarns create a conduction path between the in-plane yarns and thus enhance the conductivity of the 3D woven composite.

In addition to Table 5.1 detailing the transverse "weft" and longitudinal "warp" resistances for the 3D woven specimens, the through thickness resistance of specimens was evaluated and in all cases it was less than 1 ohm (1 Ω). So, the ratio between the transverse conductivity and the longitudinal conductivity in 3D woven composites is approximately "10^{0}" as compared to "10^{-3}" for laminated composites [52]. And the ratio between the through-thickness conductivity and the longitudinal conductivity is approximately "10^{-1}" as opposed to "10^{-4}" for laminated composites [52]; which highlights the effect of the z-binding yarns in creating a conduction path/network for the current to flow in both the transverse and through-thickness directions. Moreover, this suggests that no strong anisotropy in conductivity exists in 3D woven composites. Thus, it is expected to have good current penetration within the sample as studied by Selvakumaran in [123,130]; and this ensures that the measured resistance using the 4-probe technique is actually representative volume resistivity.

5.3.2 On-axis tension resistance variation

The global stress/strain response for all the 3D woven composite architectures, tested either along the warp or the weft directions, features almost a linear elastic behaviour up to fracture (see Fig. 5.3a-c). Previous studies [20,24,44] have proven, experimentally, that the damage and cracking progression in 3D woven composites is very similar to cross-ply laminates when loaded along the warp or the weft directions. The damage starts first at the interlacement points between the Z-binder and the in-plane yarns "warp and weft". Following this stress localisation effect, in-plane yarns, perpendicular to the loading direction, start experiencing transverse cracking. This is characterised by cracks spanning the whole yarn length and multiplying in number within the yarn up to a saturation point. The damage mechanism changes to delamination between the in-plane yarns that happens at a very last stage of the loading right before the longitudinal fibre breakage of the yarns.

From the electrical resistance point of view, those damage mechanisms, detailed above, result in resistance increase due to the loss of the conduction path within the composite. For on-axis loading of 3D woven composites, damage does not start from the beginning. However, damage initiation occurs at a specific strain value [20,24] which is referred to here as Crack Onset Strain (COS). This COS value is an architecture dependent as depicted in Fig. 5.3a-c.

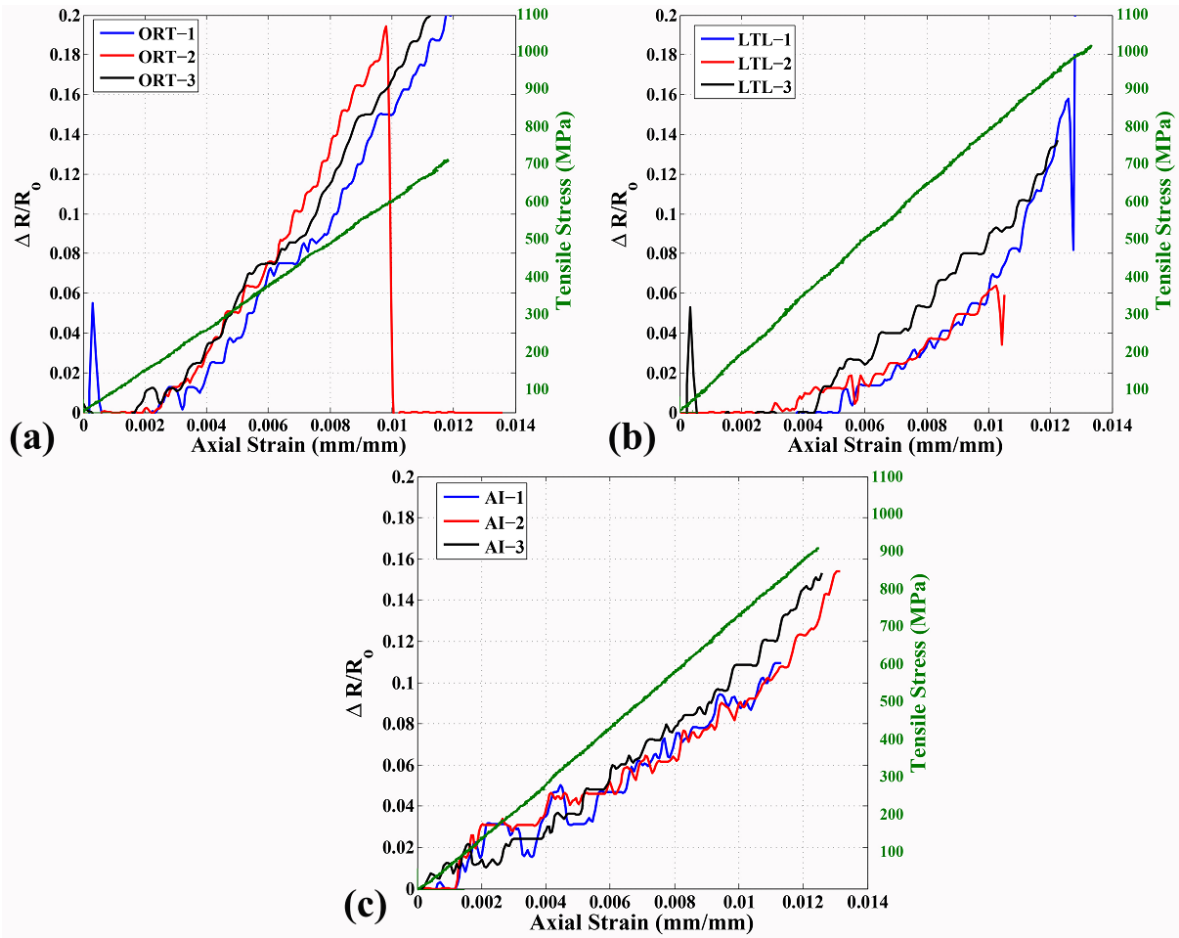

Figure 5.3 Normalised resistance variation in monotonic on-axis tension test: (a) ORT, (b) LTL and (c) AI

The normalised resistance variation in the on-axis specimens (Fig. 5.3a-c) is in the range of (15 to 20%); and it shows a repetitive pattern for all the tested specimens. This relative resistance increase is due to the fact that the main conductivity path in the on-axis specimens is the longitudinal and binder yarns while damage occurs in the transverse yarns in the form of transverse cracking and matrix diffused

damage. Those types of damage do not significantly affect the main conduction path for the current and consequently the overall resistance variation. However, this resistance increase can be detected by the electrical resistance monitoring technique. In other words, it is high enough to be captured by the proposed technique and make sure that this is not measurement error or poor electrode contact.

5.3.3 Off-axis tension resistance variation

Monotonic tensile loading

Stress/strain curves of 3D woven composites loaded in the off-axis direction (45º) are characterised by a bilinear response (see Fig. 5.5a). The "knee point" is defined as the transition point from the first to the second linear curve; and similar to the angle ply laminate case reported by Fuller in [102] this second linear curve is associated with matrix cracking and inter-yarn matrix delamination that leads to a gradual change of stiffness. Out of the three architectures investigated in this study, only the ORT architecture exhibits larger deformation and higher strain to failure. This tendency of accommodating larger deformation can be correlated to the yarns reorientation towards the loading direction. This realignment nature of the ORT architecture was captured by the electrical resistance monitoring technique as shown in Fig. 5.4a. At a specific strain value, around 17% strain, the resistance drops drastically indicating a recovery in the conduction path for the current in the ORT architecture. This can be attributed to the higher reorientation angle of yarns during testing which has been previously reported by Saleh *et al.* in [98]. As a general observation and unlike the on-axis tested specimens, there is no clear COS value for resistance increase.

Fig. 5.4d shows the representative curve of resistance of three specimens. The resistance variation, in the shaded area, (Fig. 5.4d) suggests that loss of conductivity is higher in LTL followed by AI and finally ORT. This can be correlated with the level of damage in the different architectures. At the same loading level in this reported region, LTL should have more damage followed by AI

and finally ORT. In order to validate the accuracy of this technique, an interrupted test (at several load levels) was performed on the three architectures, and the underlying damage mechanisms were observed by X-ray machine (X-Tex XT H 225 cone-beam tomograph). Two stress levels (Points B and C) from the off-axis stress/strain curve of 3D woven composites were selected (see Fig. 5.5a). The region of interest (ROI) is the centre of the specimen.

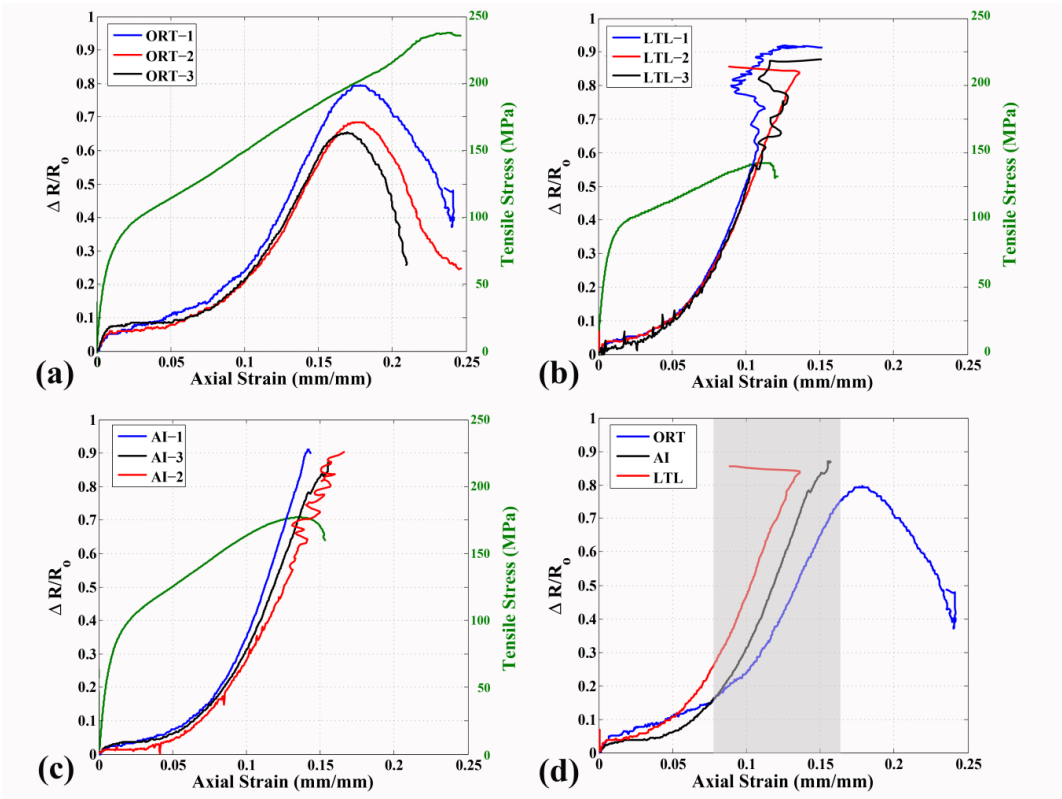

Figure 5.4 Normalised resistance variation in monotonic off-axis tension test: (a) ORT, (b) LTL, (c) AI and (d) comparison

Point A denotes zero stress where an undamage specimen was scanned by X-ray as a reference. Point B was selected at the linear elastic segment (approximately 60 MPa) in order to characterise the damage initiation before the "knee point". Point C was around 110 MPa, which is a point after the knee point where damage progression was investigated. X-ray images were captured with an X-ray setting of 35 kV and 310 µA. To aid the damage analysis using X-ray, nomenclature of damage types is given in Table 5.2.

Table 5.2 Nomenclature of damage types

Code	Damage type
F	Free edge matrix crack between yarns
Z	Z-binder induced damage
T	Transverse crack within yarns
D	Inter-yarn matrix delamination

At Point A, no damage due to manufacturing is observed by X-ray. After the specimen was loaded to 60 MPa, the first damage characteristic at Point B observed in all architectures is free-edge matrix cracking (F-type). Damage at Point B is caused by the inter-laminar stresses between layers as reported by several researchers in [104–106]. Increasing the applied stress, F-type cracks propagate towards the centre of the specimens. Reaching Point C, three damage types are identified. ORT and AI specimens exhibited binder-induced damage (Z-type) at the interlacement points between the in-plane yarns and the binding yarns. Transverse cracking (T-type) within yarns starts to multiply in number especially in the AI specimens. This explains the higher increase of resistance of the AI architecture compared to the ORT counterpart. The (D-type) damage is driven by the in-plane yarns realignment and rotation towards the loading axis. In the case of the LTL specimen, accumulation of the (D-type) cracks is more severe as it has the least strength (~130 MPa) while no Z-type damage can be observed. This leads to extensive localised damage which directly results in higher resistance for LTL as captured by the electrical resistance monitoring technique.

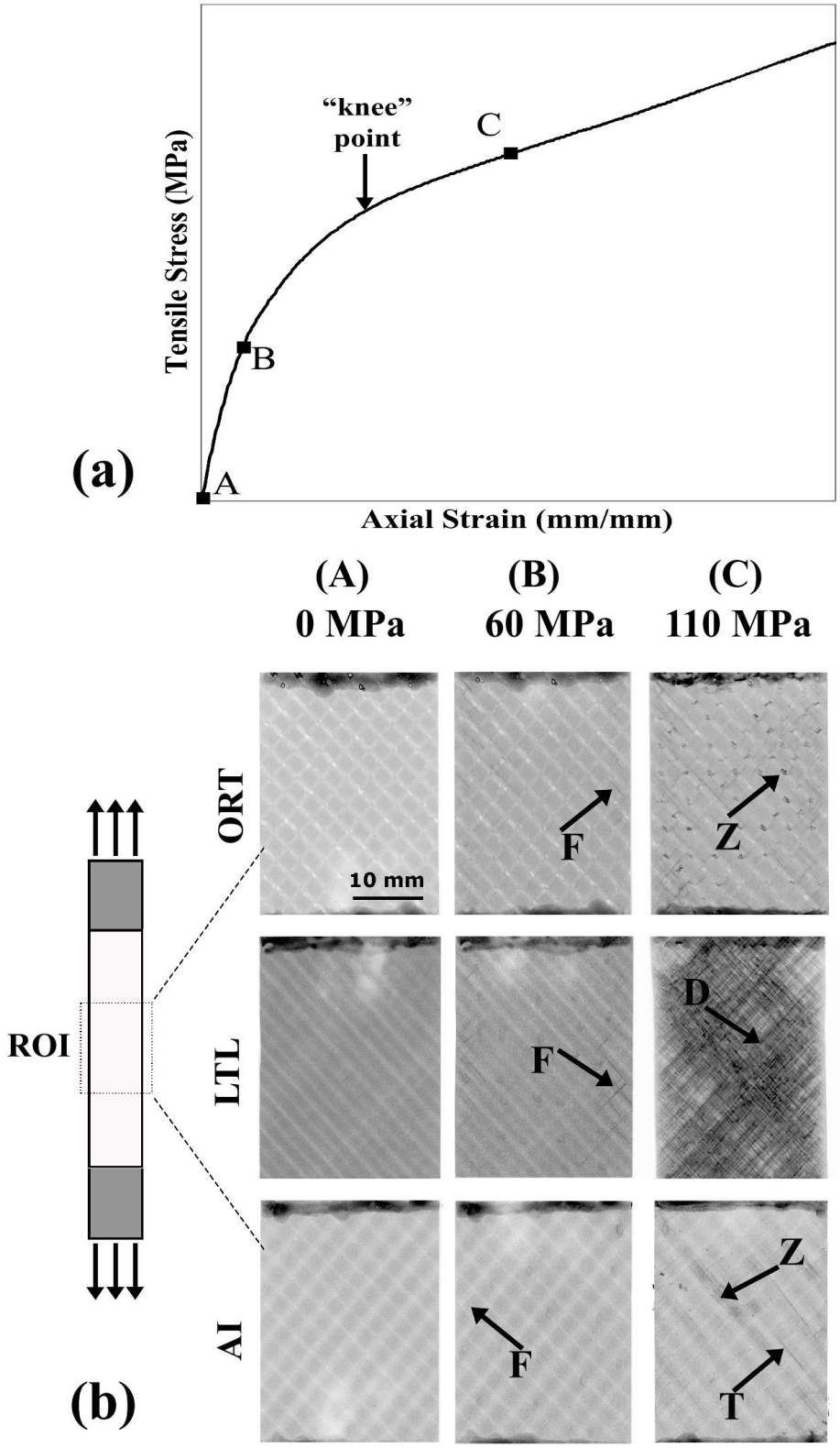

Figure 5.5 Damage evolution in off-axis tested specimens

Cyclic tensile loading

ORT specimens demonstrate a constant resistance during the unloading cycles with a slight recovery of conductivity. However, there is a tendency to recover conductivity in the beginning of the consecutive loading cycles. In Fig. 5.6a, the resistance curve drops to a minimum and starts increasing again in every loading cycle. This trend is repeatable for all the tested specimens and the different architectures as it will be detailed later. A closer investigation is detailed in Fig. 5.7 by zooming into the last unloading/reloading cycle in Fig. 5.6a.

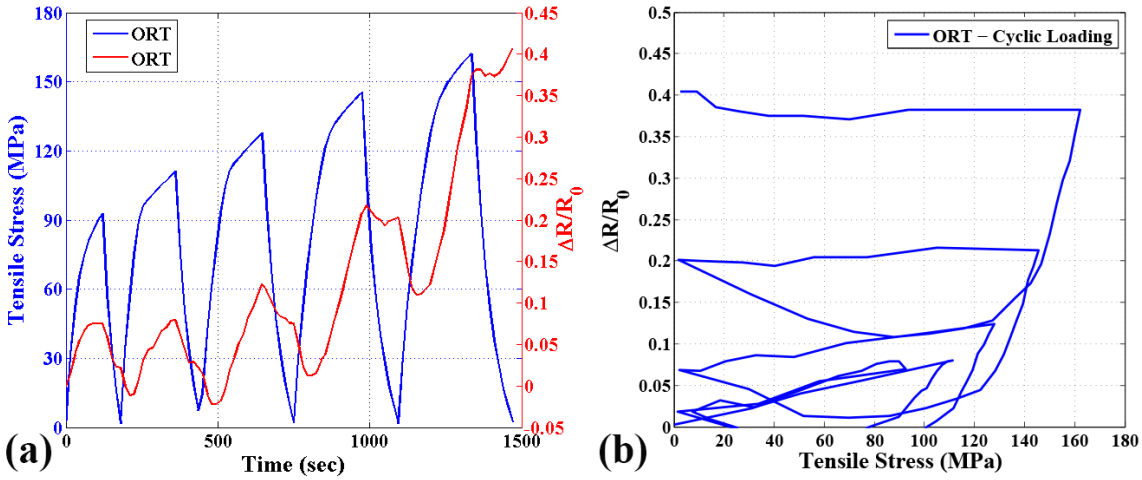

Figure 5.6 Cyclic off-axis tension of ORT: (a) stress and normalised resistance variation vs. time and (b) cyclic normalised resistance variation vs. stress

The cyclic curves (see Fig. 5.6b) show no resistance variation during the unloading cycles. In addition, the resistance increase during the reloading cycles does not exceed the maximum value of the previous cycle until the maximum stress of the preceding cycle is reached. In the last unloading cycle, although the stress level reaches almost zero stress, the resistance variation (Fig. 5.6b) remains approximately 40%. The ultimate resistance increase after removing the applied load proves that this resistance increase is due to induced damage in the tested specimen, not due to the piezo-resistive effect. In other words, the change of resistance is irreversible due to actual damage in the material.

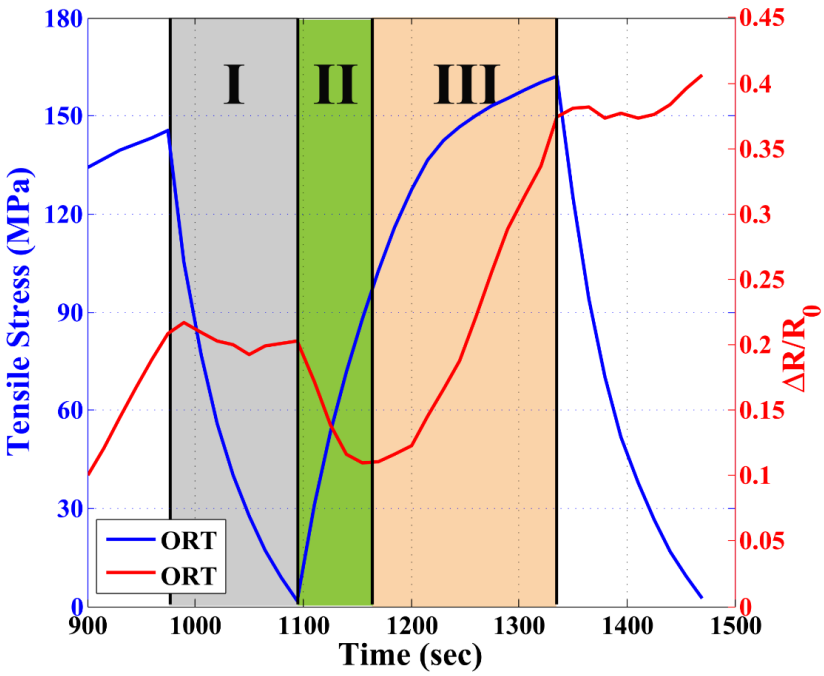

Figure 5.7 Magnification for the resistance variation in the last loading/unloading cycle

One interpretation could be drawn if the last cycle highlighted in Fig. 5.7 is divided into three main stages I, II and III. The first stage (I), while unloading, represents the irreversible electrical resistance change due to the induced damage. This is characterised by almost a constant resistance with a minor reduction upon unloading. Upon reloading in stages (II) and (III), there is a competition between two mechanisms; one of them results in recovery of conductivity "yarn realignment", while the other leads to degradation of conductivity "induced damage". In the second stage (II), it is obvious that the effect of yarn reorientation towards the loading direction is higher than the effect of the induced damage, so there is recovery of the electrical conductivity that is demonstrated in the form of resistance reduction to a minimum value. The reorientation "realignment" of yarns recovers the conductive path/network. So in spite of damage existence, resistance reversibility occurs. This competition is reversed, half way through the loading cycle, where the resistance starts increasing again from the minimum value to a higher value compared to the previous loading cycle. This simply demonstrates that the effect of the excessive induced damage during the current cycle is more

dominant than the effect of the yarns' realignment that tries to recover the conduction network.

Similarly, the AI specimens tested demonstrated the same trend like the ORT specimens. It is clear from Fig. 5.8a that AI specimens demonstrate a constant resistance during the unloading cycles with a slight decrease; while there is a tendency to recover conductivity in the beginning of the consecutive loading cycles. This behaviour can be explained in the same manner as the ORT specimens. In addition, for the cyclic curves, both remarks regarding the constant resistance upon unloading and the resistance increase every reloading cycle are still valid (see Fig. 5.8b). The only difference here is in the final change of resistance after unloading which is around 60% in this case.

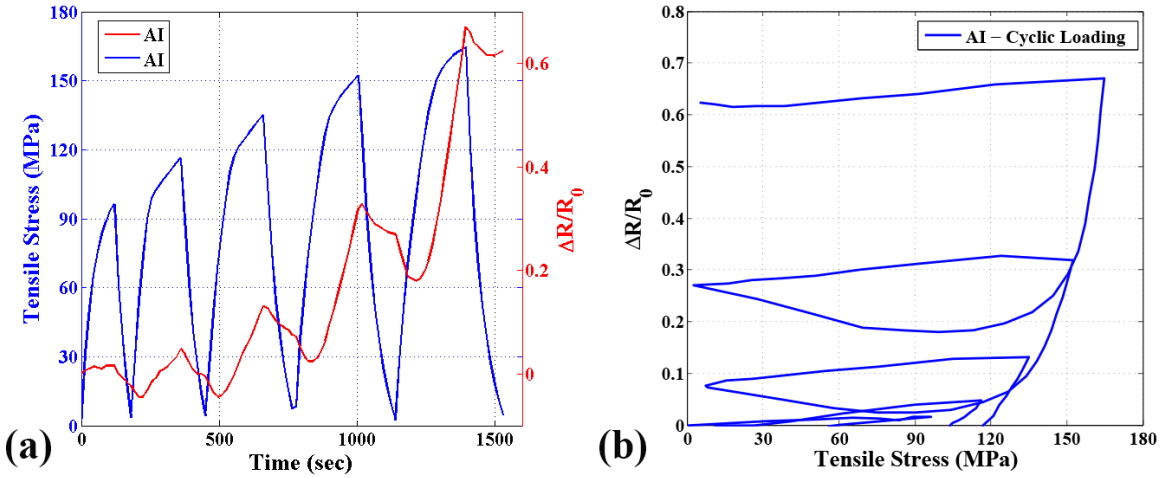

Figure 5.8 Cyclic off-axis tension of AI: (a) stress and normalised resistance variation vs. time and (b) cyclic normalised resistance variation vs. stress

For LTL specimens, the same trend of minor resistance change while unloading and conductivity recovery upon reloading is shown in Fig. 5.9a and Fig. 5.9b. However, there is one major difference compared to the ORT and AI specimens. The resistance variation is much higher compared to the other architectures. This is attributed to the fact that damage occurs in a localised region for the LTL specimens (Fig. 5.10) starting from the third cycle. The level of damage induced in

the LTL specimens after this cycle leads to extensive localised damage level in the region of interest of the LTL specimen results in high resistance measurement.

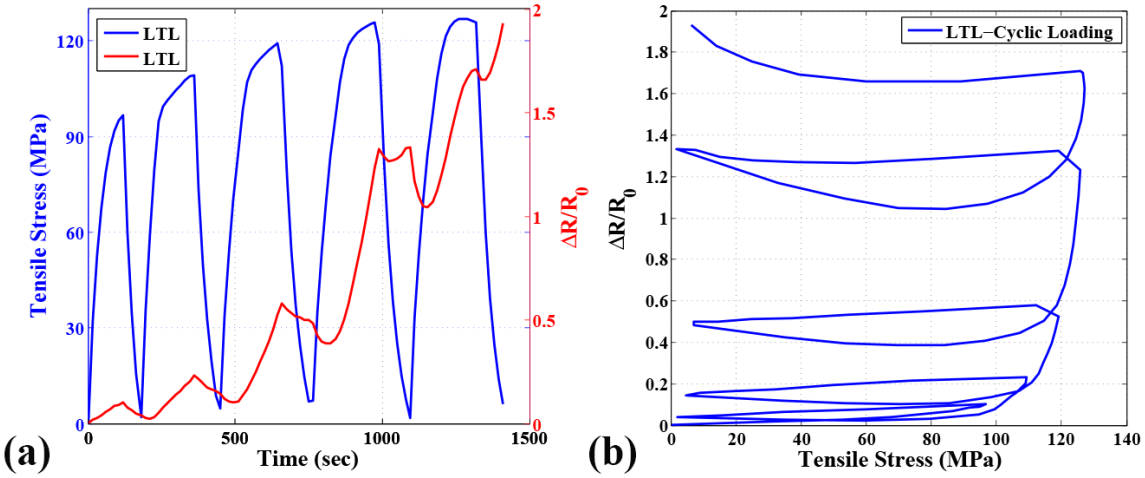

Figure 5.9 Cyclic off-axis tension of LTL: (a) stress and normalised resistance variation vs. time and (b) cyclic normalised resistance variation vs. stress

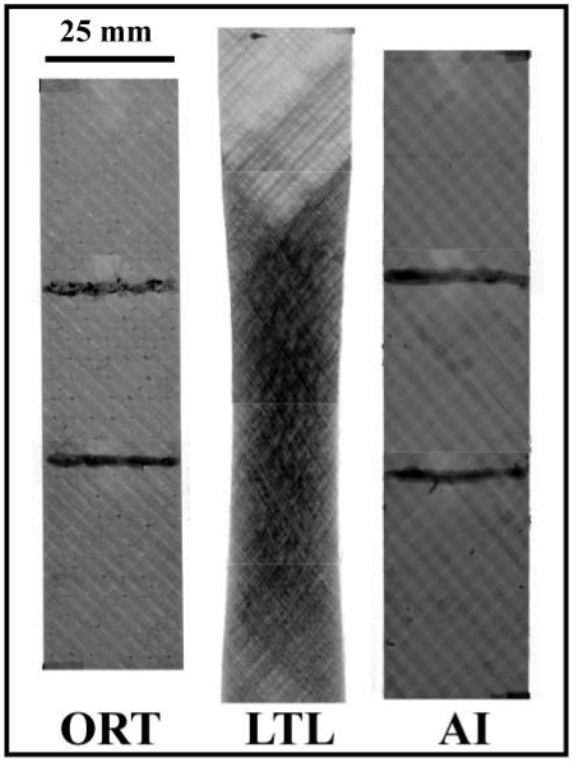

Figure 5.10 Comparison between the level of damage and cross-section reduction for 3D woven composites in cyclic off-axis tension

In order to understand the evolution of damage and plasticity in 3D woven composites tested in the off-axis direction, results from the cyclic "load/unload" test are investigated. A schematic is shown in Fig. 5.11a to explain the calculation of the following parameters.

- E_0: the initial tensile modulus of the tested specimen
- E_i: the tensile modulus at a given cycle (i)
- d_i: the damage level at a given cycle (i)
- ε_i^e: the elastic strain after unloading at a given cycle (i)
- ε_i^p: the residual plastic strain after unloading at a given cycle (i)

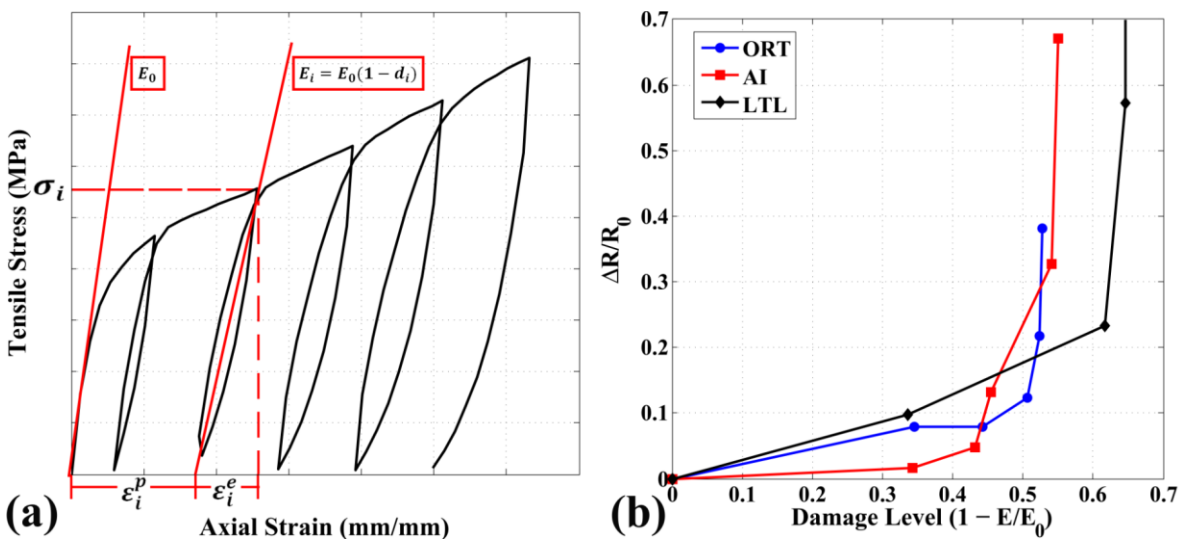

Figure 5.11 (a) Reduced modulus and plastic strain calculation schematic, (b) evolution of resistance as function of damage level

Table 5.3 Modulus, plastic strain and normalised resistance as function of the loading cycles

Cycle	Modulus (GPa)			Plastic strain (%)			$\Delta R/R_0$		
	ORT	AI	LTL	ORT	AI	LTL	ORT	AI	LTL
Initial	11.97	12.07	13.08	0.00	0.00	0.00	0.00	0.00	0.00
1st	7.84	7.87	7.95	1.21	1.13	1.42	0.08	0.02	0.10
2nd	6.67	6.81	4.59	3.61	3.49	4.61	0.08	0.05	0.23
3rd	5.91	6.53	4.24	5.75	5.96	8.55	0.12	0.13	0.57
4th	5.71	5.50	4.24	7.84	8.08	13.37	0.22	0.33	1.33
5th	5.66	5.39	3.97	9.98	10.78	20.51	0.38	0.67	1.71

The initial modulus (E_0) for all the architectures is determined by measuring the slope of the stress strain curve in the first loading stage; while the reduced tensile modulus for a given cycle (i) is determined from the unloading curve as shown in Fig. 5.11a. The evolution of the tensile modulus as well as the residual plastic strain and the normalised resistance variation as a function of the "loading/unloading" cycle is reported in Table 5.3.

As LTL architecture has the least undulation followed by AI and finally ORT, it demonstrates the highest initial modulus followed by AI and ORT. However, once damage accumulates, the LTL architecture experiences more delamination and slippage between in-plane yarns which is directly reflected in the reduction of the modulus especially at the last cycle. Due to through-thickness binder existence, AI and ORT experience less damage compared to LTL. Moreover, as the ORT unit cell is smaller than AI, ORT binding yarns can resist delamination so it maintains the highest modulus, the least damage level and plastic strain after unloading at the last cycle. Similarly, the change of resistance as function of the damage level (Fig. 5.11b) supports the fact that LTL samples experience more damage followed by AI and ORT which is directly reflected in the resistance increase.

5.4 Concluding Remarks

Through a systematic experimental study, electrical resistance monitoring has been proven to have the potential not only for detecting damage initiation but also for tracking damage evolution in 3D woven composites tested in both on-axis and off-axis directions. The effect of the through-thickness binder is clearly seen as the initial resistance of the specimens are architecture dependent. For on-axis loaded specimens, the resistance increase due to damage in the transverse yarns and delamination can still be detected using the 4-probe technique as the resistance increase is around 20%. The resistance increase for the off-axis loaded specimens is much higher than for on-axis counterparts as it reaches approximately 90%. Out of all the 3D woven architectures, the 3D orthogonal woven composite loaded off-

axially exhibits a recovery in electrical conductivity which indicates that yarn realignment reached a point where they become connected again and resistance drops accordingly. For all the off-axis tested specimens, the resistance increase upon unloading is irreversible which proves that the resistance increase is due to actual damage in the tested specimens, not due to a piezo-resistive effect. In cyclic loading tests, during unloading the resistance drop is small due to the piezo-resistive nature of the samples. However, during reloading the resistance drops due to fibre/yarns realignment up to a point at which the effect of induced damage becomes more significant than the recovery due to the realignment process. That is why the resistance starts increasing again. The remaining challenge for electrical resistance monitoring would still be the capability of localising and sizing the damage in 3D woven composites. Further development can be achieved by correlating the electrical resistance change to the damage evolution through micromechanical models such as the one detailed in **Chapter 8**. This ERM technique can also be further extended to detect the damage in open-hole tension of 3D woven composites which is the scope of the next chapter.

6 Open hole tension of off-axis 3D woven composites

6.1 Introduction

As previously concluded in **Chapter 4**, 3D woven composites tested in the off-axis direction demonstrated high strain to failure and more energy absorption compared to their on-axis counterparts. Out of all the examined architectures, 3D orthogonal woven composites (ORT) demonstrated a superior behaviour indicated by high strain to failure (~23%) and high translaminar energy absorption (~40 MJ/m^3). As ORT architecture has smaller unit cell size than LTL and AI, this enables stress redistribution over a longer span of the specimen, and prevents slippage between in-plane yarns. Thus, the damage in ORT seems to be uniformly distributed all over the gauge length of the specimen. Those two characteristics "pseudo-ductility and stress redistribution/relief" make ORT architecture loaded in the off-axis "shear" direction a potential candidate for composite joint applications where those lateral characteristics are key design parameters [71,131,132]. One additional key parameter is the notch sensitivity of composite materials. The strength and damage progression of composite materials is significantly affected by notch presence. That is why the open-hole tensile strength of 3D woven composites tested off-axially is investigated in this chapter.

Previous studies focused on evaluating the effect of notches on the fracture toughness, strength as well as damage and failure mechanisms of both laminated [133,134] and 2D woven composites [135,136]. It was observed that the woven laminates exhibited more resistance to delamination and splitting compared to laminated composites. The undulating nature of the woven fabric acted as crack stoppers in the sense that it prevented crack propagation within the matrix. This led to a notched strength that is higher for 2D woven laminates compared to laminated composites which could be translated into less notch sensitivity

[137,138]. Further enhancement for the notch strength and fracture toughness of composites was achieved by replacing 2D woven by 3D woven composites as reported in [23,139]. The through-thickness binder in 3D woven composites reduced dramatically the notch sensitivity of 3D woven composites and improved the fracture toughness and damage tolerance compared to 2D woven laminates.

One recent study, by Dai *et al.* [140], investigated the notch sensitivity of CFRP 3D orthogonal and angle interlock woven composites tested in quasi-static tension and tension-tension fatigue. Both tests categories focused on the on-axis loading either along the warp or the weft direction. Damage evolution was characterised and monitored using DIC and infra-red camera for the fatigue testing. Moreover, the effect of the notch size was addressed by comparing two different hole sizes with a diameter to width ratio of 1/6 and 1/2 respectively. The study concluded that regardless of the hole size, the reduction in the strength of the investigated architectures did not exceed 17% compared to the un-notched strength in the case of on-axis loading.

Although 3D woven composites tested along the warp or weft directions have been proven to be relatively notch insensitive [140,141], nothing was reported with regards to the behaviour/sensitivity of 3D woven composites loaded along the off-axis direction. So, this part of the study will only consider this aspect as there is little point in repeating previous work in the case of on-axis loading, either along the warp or the weft directions. So, this chapter is divided into four main sections. Section 2 details the specimens' preparation process and the testing method. Then, section 3 discusses the key findings of the study. Finally, section 4 summarises the chapter and gives insight about the potential of using 3D woven composites in composite joints' applications.

6.2 Testing procedure

According to the ASTM standards D5766 "Test Method for Open-Hole Tensile Strength of Polymer Matrix Composite Laminates", the suggested specimen

dimensions are (200 x 36 mm^2) with a hole diameter of 6 mm; so the diameter to width ratio (d/w) is (1/6). However, those suggested dimensions are not followed here. The objective of the study is to compare the notched strength of the off-axis 3D woven specimens against the un-notched ones. As the un-notched specimens were standard tensile coupon specimens, the nominal dimensions are (250 x 25 mm^2). Thus, the open-hole tensile specimens were cut with the same dimensions but the ratio between the hole diameter and specimen width was kept as (1/6) according to the standards. It is worth mentioning here that this was the only modification made to the testing method D5766.

6.2.1 Specimen preparation

Before the drilling process, the area to be drilled was 'sandwiched' between two small glass/epoxy plates with tapes in order to minimise the damage around the hole rims. A hole of 4.16 mm was made by CNC lathe machine (VMX42SR, Hurco) as shown in Fig. 6.1a. In this case, the ratio between hole diameter and specimen width is maintained to be 1/6 as recommended by the ASTM standards. The drill bit is made of carbide with a diameter of 2 mm (see Fig. 6.1b). The drilling process was carried out at 3000 rpm starting with a 2 mm hole until the hole reached 4.16 mm diameter.

Figure 6.1 (a) CNC lathe machine, (b) carbide drill bit with 2 mm diameter

A speckle pattern is applied over an area of 50 mm x 25 mm in the middle of the specimen. White paint is sprayed twice. Upon drying, black paint is sprayed over the white surface forming a speckle pattern.

6.2.2 Test setup

With a 2 mm/min displacement-controlled rate, the open-hole tensile test was conducted for all the off-axis architectures (ORT, LTL and AI). DIC was used, as a non-contact strain measurement device, to capture the strain contour map over the specimens' surface and intensity around the hole. Fig. 6.2 shows the test setup and the speckle pattern around the hole. All tests were performed in a controlled environment where the temperature was 21°C and the relative humidity (RH) was 45%. The speckle images were then processed using Vic 2D. DIC image processing parameters were kept the same as Section 4.1.2 for comparison.

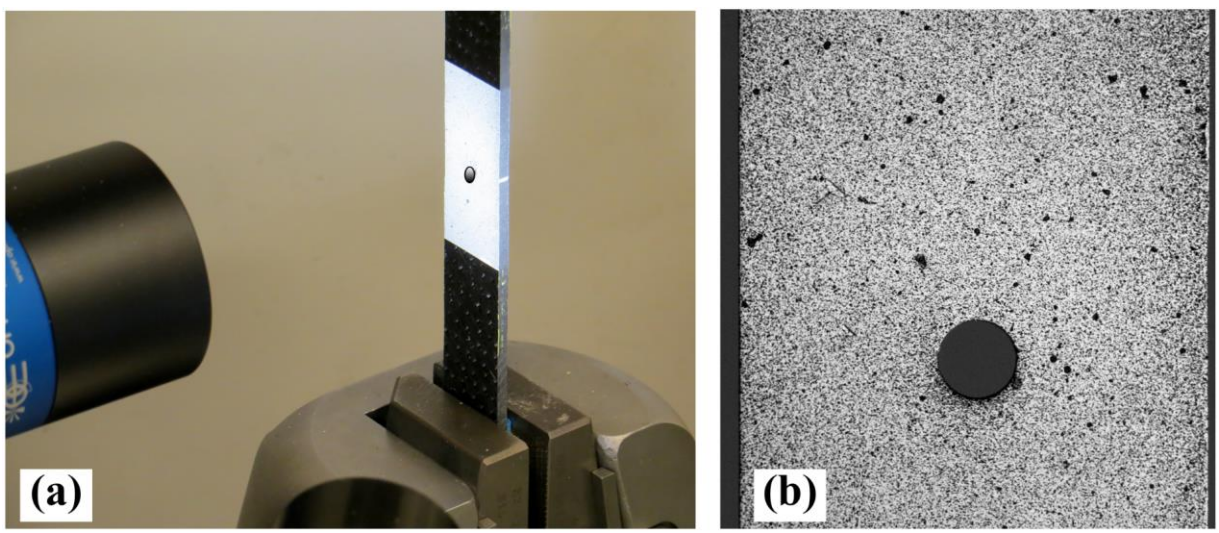

Figure 6.2 Open hole tension (a) Test setup (the hole has been highlighted for clarification), (b) Typical speckle pattern around the hole

6.3 Results and discussion

6.3.1 Stress strain curves

Global stress strain curves for the notched 3D woven composites loaded in the off-axis direction are shown in Fig. 6.3a-c. For the sake of comparison, the open-hole

"notched" results are plotted in dashed line format against the un-notched results in solid lines. For all the tested architectures, the linear elastic behaviour of the notched curve is almost the same as the un-notched or at least lies within the experimental marginal error. Once damage accumulates after the "knee" point, there is a slight reduction in the slope of the ORT notched result compared to the un-notched ones. However, for the LTL and AI architectures, this difference is not as significant. The ultimate tensile strength mean values for the notched and un-notched specimens are detailed in Table 6.1.

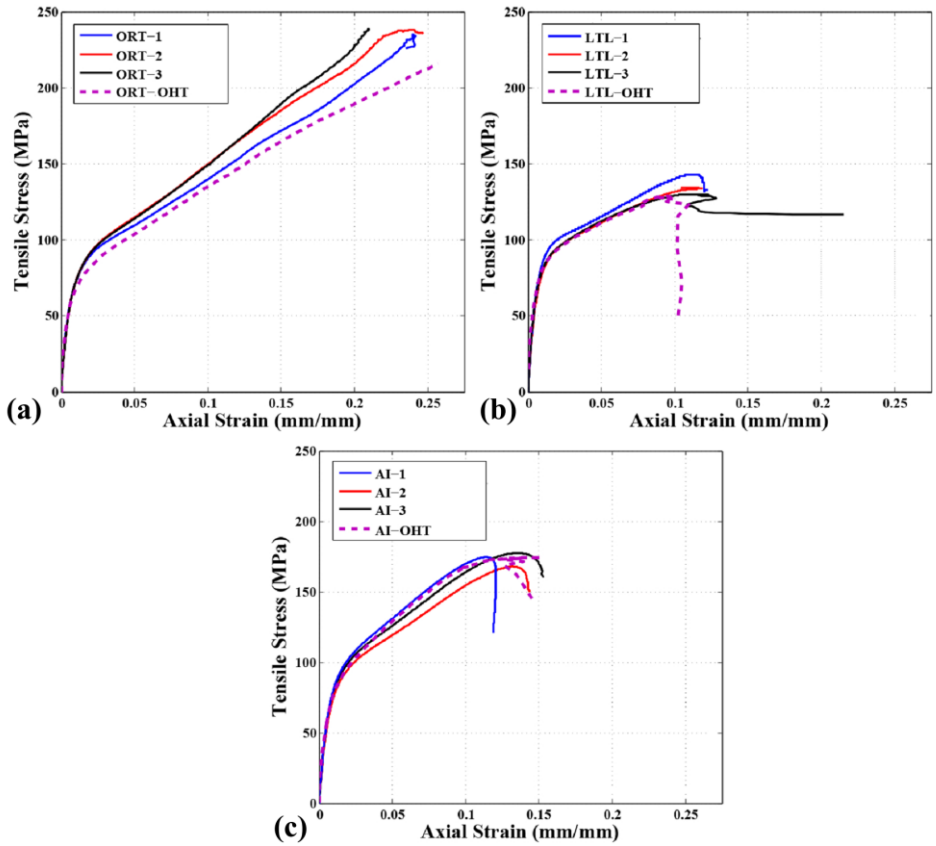

Figure 6.3 Stress strain curves for un-notched "solid" vs. notched "dashed" lines for (a) ORT, (b) LTL, (c) AI

In this study, the normalised tensile strength is defined as the notched strength (σ_n) divided by the un-notched strength (σ_{un}) of the tested specimens. For all the tested architectures, the normalised tensile strength is greater than 90% of the un-notched ultimate strength. This suggests that the 3D woven architectures in the

off-axis orientation are relatively less sensitive to notches existence. Further understanding of the damage progression and reasons for this notch insensitivity is discussed in detail later in this chapter.

Table 6.1 Comparison between average notched and un-notched strength for 3D woven architectures loaded off-axially

Textile architecture	Strength Un-notched (MPa)	Strength Notched (MPa)	σ_n/σ_{un}
ORT	237.37	215.29	0.91
LTL	135.73	128.31	0.95
AI	173.3	172.21	0.99

To evaluate the notch sensitivity of the tested off-axis 3D woven composites "at this specific hole diameter to width ratio", the notched tensile strength is normalised by the un-notched strength. Then, the normalised value is compared against the ideally ductile "notch insensitive" curve and the ideally brittle "notch sensitive" curve as depicted in Fig. 6.4.

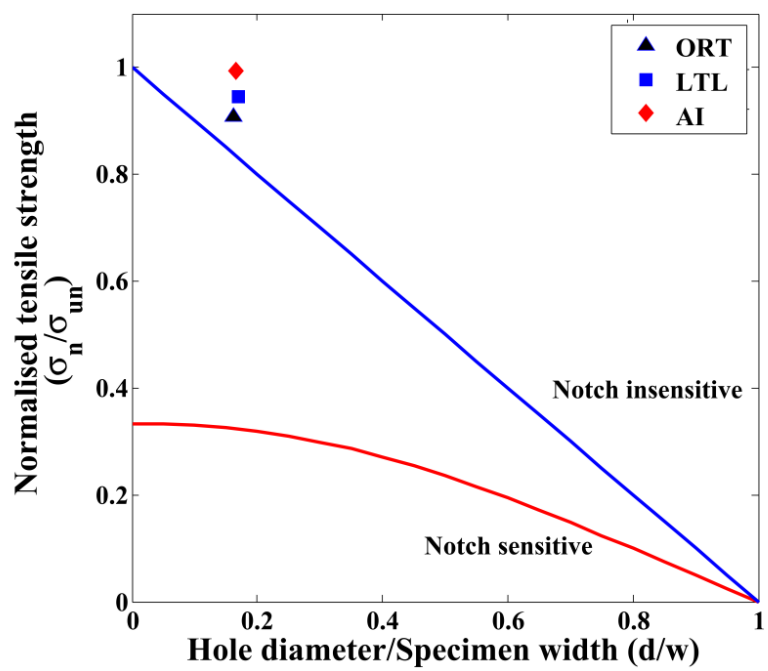

Figure 6.4 Notch sensitivity/normalised strength in off-axis composites

Equations for calculating the notch sensitive and notch insensitive responses [134] are detailed as follows:

- Notch insensitive (ductile materials)

$$\sigma_n/\sigma_{un} = 1 - (d/w) \tag{6.1}$$

where:

(σ_n) : The notched tensile strength

(σ_{un}) : The un-notched tensile strength

(d) : The hole diameter

(w) : The specimen width

- Notch sensitive (brittle materials)

$$\sigma_n/\sigma_{un} = [1 - (d/w)]/K_T \tag{6.2}$$

$$K_T = 2 + [1 - (d/w)]^3 \tag{6.3}$$

where (K_T) is the finite width concentration factor.

It is clear from the comparison that all the three 3D woven architectures are notch insensitive when loaded in the off-axis orientation for this specific diameter to width ratio. This behaviour can be attributed to two major reasons. The first reason is common even for laminated composites which is the lay-up orientation in that case. And the fact that the tested architectures are 3D woven composites does not significantly affect the behaviour. However, the second reason is the effect of the binder existence which typically distinguishes 3D woven composites from their 2D laminated counterparts. To elaborate more on those two reasons, the change of the lay-up orientation from ($0^o/90^o$) to ($\pm 45^o$) directly affects the Stress Concentration Factor (SCF) at the notch "hole". For an isotropic material, the SCF of a hole in an infinite plate [142] is approximately 3. Composites are not isotropic in nature; on the contrary, they are anisotropic material systems in which the material response is completely dependent on the lay-up. For orthotropic laminates loaded at an angle from their principal directions [65], the SCF varies between (0 to 8) times the global stress applied. This is explained further by applying the stress transformation tensor to the global stress putting into consideration the

angle between the loading direction and the lamina principal directions. The off-axis ($\pm 45^{o}$) orientation reduces the global stress concentration to approximately 1.7 times the global stress; which means less sensitivity to the notch "hole" presence. In addition, 3D woven composites are characterised by out-of-plane binding yarns that hold the in-plane yarns. In the case of notched specimens those binding yarns play a major role in supressing delamination and damage evolution as well as stress redistribution on wider areas as explained previously in Section 4.4; and will be elaborated more in the following section.

Remark:

- The relative notch "size/diameter" to the unit cell size of 3D woven architectures is an important parameter that should be investigated as it may affect the response of those material systems. Due to material shortage, only one notch size was considered in this study and it was less than the unit cell size for all architectures ORT, LTL and AI.

6.3.2 Damage evolution

Analysis of the DIC images Fig. 6.5 to Fig. 6.7 better explains the strain/stress distribution and damage evolution in all the notched 3D woven architectures loaded in the off-axis direction at various loading levels. At the very early loading levels $\sim$ 5% strain (Fig. 6.5a, Fig. 6.6a and Fig. 6.7a), the strain distribution shows that the localised strain/stress regions do not only exist around the hole edge but also at the interlacement points between the binding yarns and the weft yarns of the 3D woven composites. Regions of localised strain in all architectures lie on the ($\pm 45^{o}$) directions.

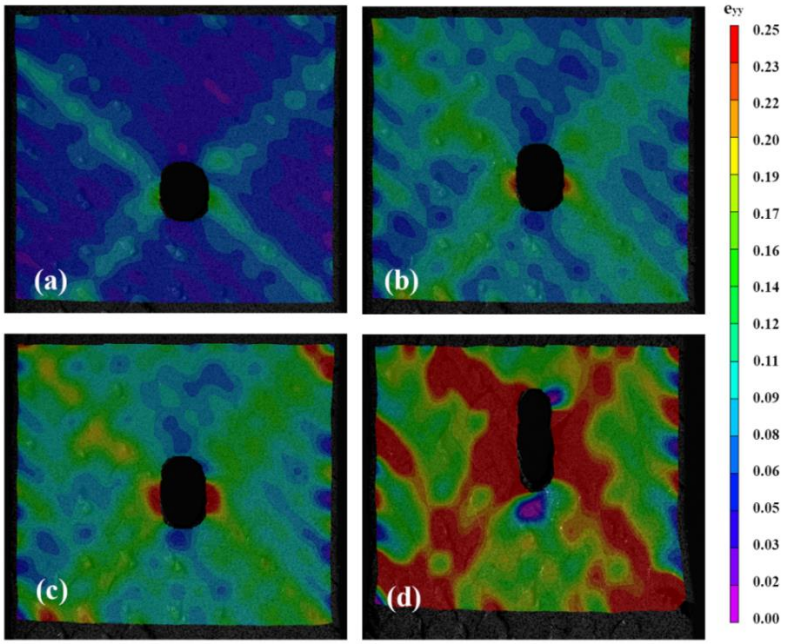

Figure 6.5 Evolution of axial strain contour map for ORT (a) 0.05, (b) 0.09, (c) 0.11, (d) 0.18 mean strain

When the load is increased, the stress concentration regions in all the architectures can be found only at the notch "hole" tip. This is clear in (Fig. 6.5b, Fig. 6.6b and Fig. 6.7b) where the red regions are highlighted. Due to this stress concentration, damage and cracking initiates in the form of matrix cracking. Although at that stage the global strain applied does not exceed 10%, very high strain values (> 25%) is observed around the hole edge which indicates the regions of stress concentration and eventually the premature damage. It is worth mentioning here that those strain/stress concentration regions captured by the DIC suggests that the level of damage is even higher than the induced damage due to the free-edge cracking at that stage of loading.

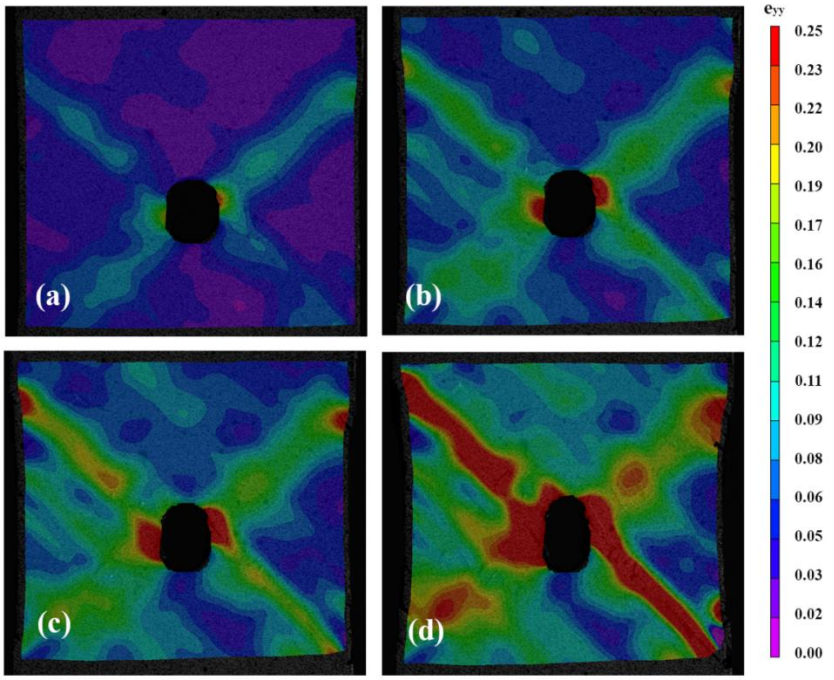

Figure 6.6 Evolution of axial strain contour map for LTL (a) 0.04, (b) 0.07, (c) 0.09, (d) 0.12 mean strain

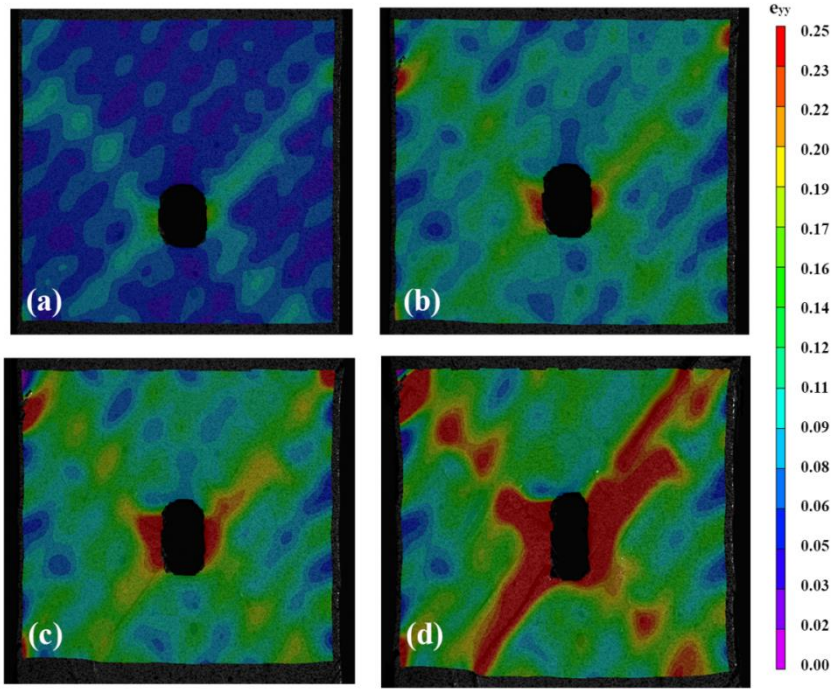

Figure 6.7 Evolution of axial strain contour map for AI (a) 0.06, (b) 0.10, (c) 0.12, (d) 0.15 mean strain

Upon load increase, the damage zone expands along the ($\pm 45^{o}$) direction (Fig. 6.5c, Fig. 6.6c and Fig. 6.7c) in the form of matrix cracking and delamination until they are arrested by binding yarns. This is one major difference in the damage evolution between 3D woven and laminated composites. In laminated composites, those ($\pm 45^{o}$) matrix cracking and delamination areas extend across the specimen width and lead to final fracture of the specimens in an instantaneous catastrophic manner while in 3D woven composites, the damage evolution is more progressive and does not lead to catastrophic fracture. Finally before failure (Fig. 6.5d, Fig. 6.6d and Fig. 6.7d), the ORT architecture seems to be different from the other architectures in the sense that strain/stress is redistributed over a larger area of the specimen unlike the AI and LTL where the damage extends along a ($\pm 45^{o}$) line and causes final fracture without being arrested by the binders. To be more precise, damage progression and cracking cause the binder to fracture which leads to the final failure of those architectures. Through the whole test, the hole elongation is properly captured by the DIC system as shown in (Fig. 6.5 to Fig. 6.7).

Optical images for the surfaces of the three tested architectures (Fig. 6.8a-c), just before fracture, demonstrate excessive hole elongation, matrix cracking and inter-yarn delamination in the form of ply separation and free-edge cracking around the hole and at the edges of the specimens. Again, it is clear that due to the smaller unit cell in the ORT architecture, the matrix cracking and delamination are arrested and do not extend along the whole span of the specimens' width as it is the case in the LTL and AI architectures.

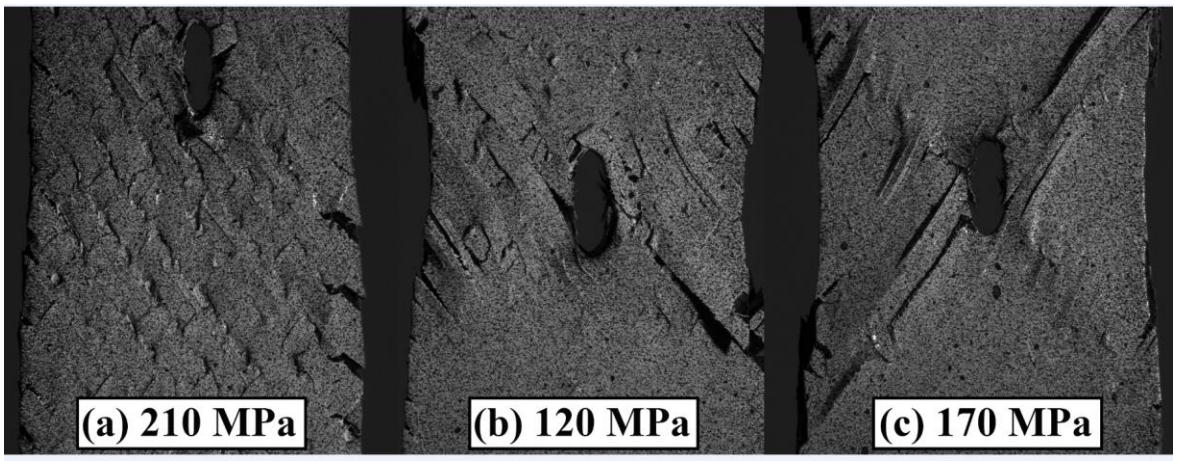

Figure 6.8 Optical surface images at failure for (a) ORT, (b) LTL, (c) AI

6.4 Concluding Remarks

In this chapter, the notched response of 3D woven composites, in off-axis orientation, has been studied by open hole tension according to the ASTM standard. The global stress strain response suggests that all 3D woven architectures (ORT, LTL, and AI) are notch insensitive. The final failure of all the 3D woven architectures in the off-axis direction is progressive failure not catastrophic brittle fracture. Out of all the tested architectures, the ORT architecture in the off-axis orientation exhibits higher ultimate strength and strain to failure, as was the case for the un-notched specimens. From the DIC analysis, the ORT architecture redistributes the stress over a wider region away from the hole which reduces the stress concentration at the notch periphery. In addition, the higher intensity of binding yarns acts as crack stoppers for delamination and matrix cracking. Thus, 3D woven composites in the off-axis orientation, especially ORT, demonstrate a potential of overcoming some of the major challenges for composite joint applications which are the pseudo-ductility, stress redistribution away from the notch and notch insensitivity. One last investigation for the potential usage of 3D woven composites in composite joint applications, discussed in the following chapter, is the single fastener double-lap joint bearing strength test.

7 Bearing strength response of off-axis 3D woven composites

7.1 Introduction

So far in this research, 3D woven composites tested in the off-axis direction have been proven to have high strain to failure and higher energy absorption. Moreover, it has been shown in **Chapter 6** that 3D woven composites in the off-axis direction are relatively notch in-sensitive which affirms their potential of being used in composite joint applications. One additional aspect that needs to be investigated is the bearing response of those material systems which is the focus of this chapter.

In spite of many studies investigating the bearing response of 2D laminated composites [71,131,143–148], the literature discussing the bearing response for 3D woven composites is quite sparse. Only one recent study by Warren *et al.* [149] investigated the bearing response of two 3D woven architectures namely as layer-to-layer and orthogonal structures. The study extensively investigated the single-lap bearing response of these architectures and its dependency on the loading orientation using seven different orientations between warp (0º) and weft (90º) directions. In addition, they only studied the double-lap bearing response of the same architectures along the warp direction. For the layer-to-layer architecture, two sizes of IM7 carbon tows were used; 12K and 24K respectively. The study concluded that 3D woven composites fail in a non-catastrophic manner and the associated failure mode is bearing failure. The most dominant damage mechanisms were found to be matrix cracking and tow distortion around the hole which caused some drop in the load. Changing the loading direction orientation in the single-lap bearing strength test led to stiffness reduction in the range of 24.7% to 32.7% of the on-axis stiffness. The 24K tow size increased slightly the bearing response compared to the 12K layer-to-layer and orthogonal architectures. Nevertheless, no

previous work investigated the off-axis double-lap bearing strength response of 3D woven composites.

7.2 Testing procedure

7.2.1 Test setup

The single-fastener double-lap bearing strength test is conducted according to "*Procedure A*" of the ASTM standards D5961 "Bearing Response of Polymer Matrix Composite Laminates". The specimen dimensions are (135 x 36 mm^2) with a hole diameter of 6 mm and an end distance of 18 mm; so the diameter-to-width ratio (d/w) is (1/6). The drilling was carried out with a steel-tipped drill bit. The fastening torque applied is 2.8 N.m which is again within the recommended range of the ASTM standard (2.2 N.M to 3.4 N.m). With a 2 mm/min displacement-controlled rate, the test was conducted for all the off-axis architectures (ORT, LTL, AI). An advanced video extensometer (AVE) was used, as a non-contact strain measurement device, to capture the strain throughout the whole test. A schematic diagram of the testing setup is shown in Fig. 7.1. All tests were performed in a controlled environment where the temperature was 21ºC and the relative humidity (RH) was 45%. It is recommended by the standards to stop the test at 50% strain in order not to mask the failure mode of the specimens. However, in this study, there was an interest in calculating the energy absorption up to final failure of the joint. Thus, five specimens were tested for ORT, LTL and AI resulting in fifteen specimens in total. Three of those five were tested only up to 50% strain to be able to evaluate the failure mode while the other two were tested up to final failure.

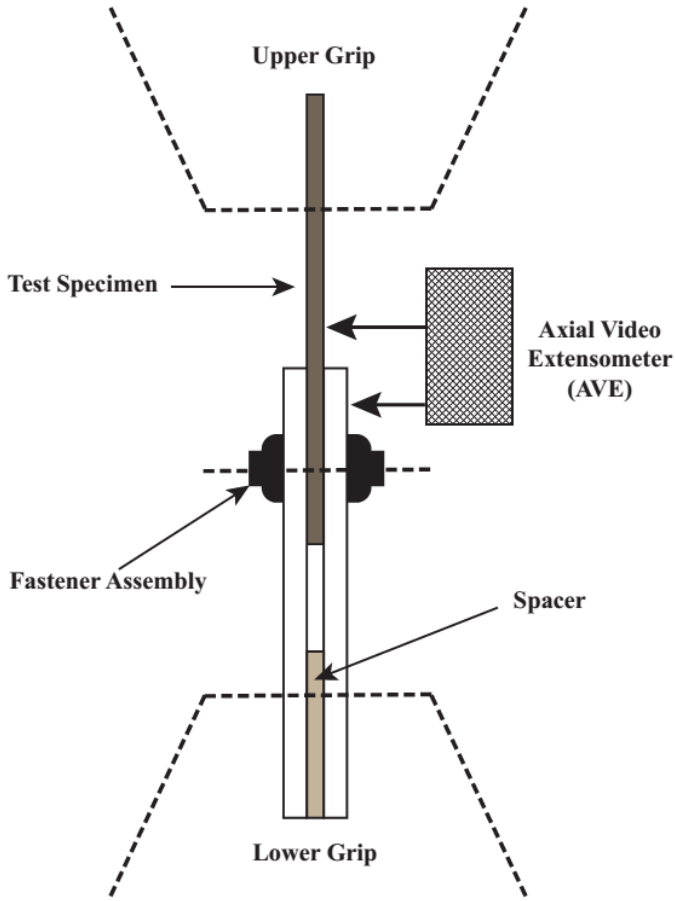

Figure 7.1 Schematic diagram of double-lap bearing strength test

7.2.2 X-ray CT setup

The damaged 3D woven composite samples (ORT, LTL and AI) were examined using X-ray CT. A dye penetrant was employed to enhance the contrast between the damaged volume (air) and the bulk composite prior to X-ray CT imaging. The dye penetrant consisted of 250 g zinc iodide, 80 ml distilled water, 80 ml isopropyl alcohol and 1 ml Kodak photoflow. The samples were soaked in the dye penetrant solution for 24 hours in order to allow sufficient penetration into all connected damage. X-ray CT scanning was performed on the Nikon XTH 225 CT scanner in the Henry Moseley X-ray Imaging Facility. A tungsten target was used and the accelerating voltage and current were set to 100 kV and 70 μA respectively. The exposure time for each projection was 1 second and 5013 projections were collected

over 360º, resulting in a total data acquisition time of 1.5 hours. Reconstruction was performed using the 3D CT Pro software and the voxel size of the reconstructed CT datasets was 16.8×16.8×16.8 μm^3. 3D visualisation and data analysis were carried out using Avizo 9.0 software.

7.3 Results and discussion

7.3.1 Stress strain curves

The global bearing stress/bearing strain curves for the 3D woven composites loaded in the off-axis direction, up to 50% strain, are shown in Fig. 7.2a-c. The initial portion of the bearing stress/bearing strain curves, for all architectures, exhibits a non-linear behaviour which is correlated, in the ASTM D5961 standard [150], to a combination of different factors which include joint translation due to the hole tolerance, joint straightening and joint friction. That is why the bearing stiffness has to be determined beyond this effect in the linear portion of the curve. Once the stiffness is determined, the effective strain origin is the intersection of the chord stiffness line with the bearing strain axis. This effective strain origin is then used to calculate the offset bearing strength. The ASTM standard [150] provides detailed discussion of results and calculations. There is no significant difference in the global behaviour of the three tested architectures up to 50% strain. The bearing stress/bearing strain curve is characterised by linear response up to a specific strain where a drop in the stress is observed. Then, the bearing stress continues increasing with a lower slope with increase of the applied strain up to a maximum stress value which represents the ultimate bearing strength.

Table 7.1 summarises the bearing stiffness, offset bearing strength and ultimate bearing strength values for ORT, LTL and AI. It is clear from the comparison that the bearing stiffness of ORT is less than AI and LTL. This may be due to ORT architecture having the smallest unit cell size. However, no significant difference is observed for either the offset bearing strength or the ultimate bearing strength. As specimens are loaded in the off-axis orientation, it is quite useful to compare the

ultimate bearing strength with the compressive strength of the same material systems along the warp and weft directions.

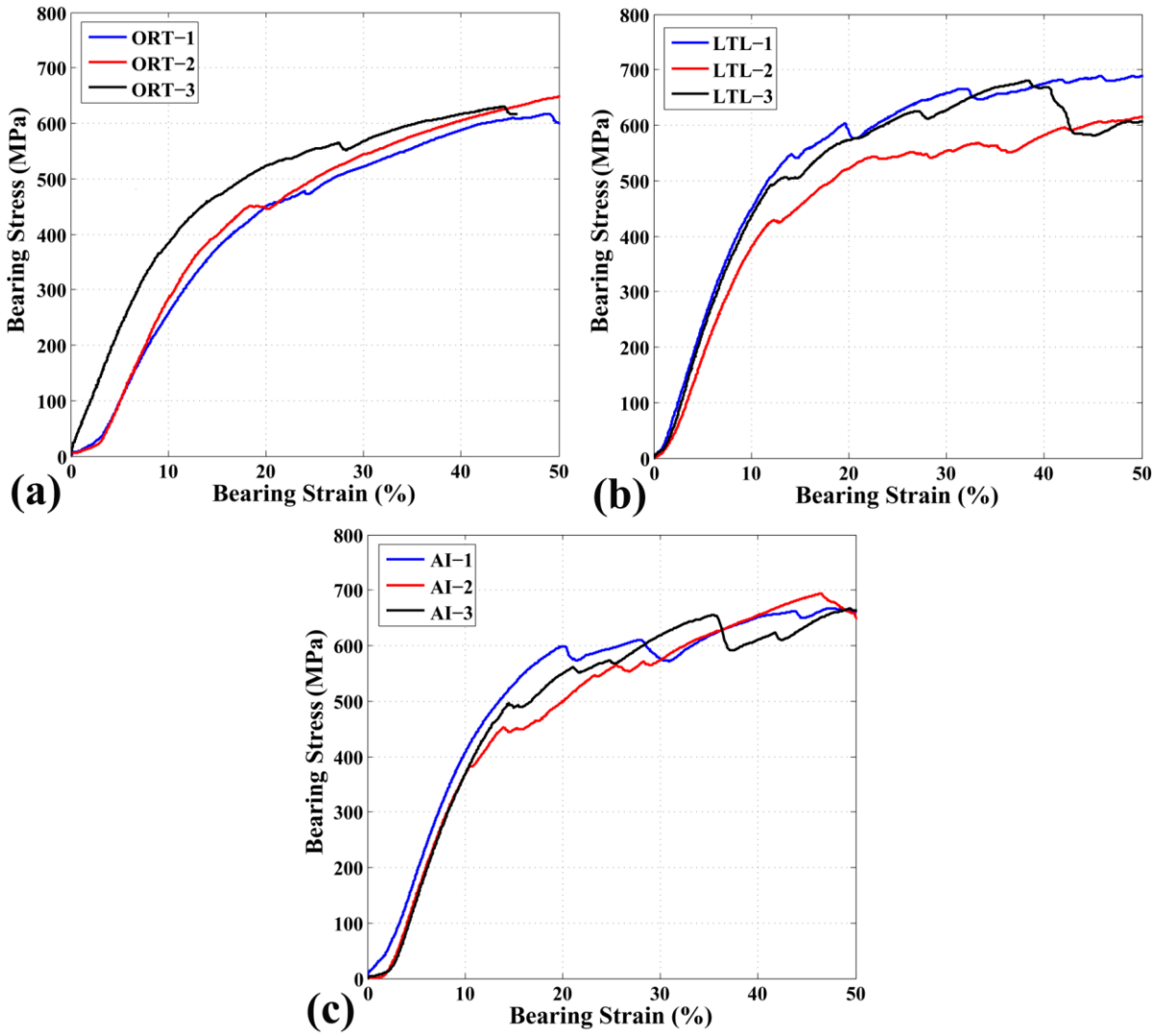

Figure 7.2 Bearing stress vs. bearing strain curves up to 50% strain for (a) ORT, (b) LTL, (c) AI

Table 7.1 Summary of bearing stiffness and strength for ORT, LTL and AI

Textile architecture	Bearing stiffness (GPa)	Offset bearing strength (MPa)	Ultimate bearing strength (MPa)
ORT	3.48 ± 0.02	429.63 ± 57.53	658.67 ± 27.62
LTL	5.32 ± 0.23	466.97 ± 33.06	677.33 ± 22.95
AI	5.26 ± 0.09	456.90 ± 38.33	683.33 ± 9.39

The 2D stress transformation for a plane-stress case (see Fig. 7.3a) is used here to transform the global (x, y) ultimate bearing strength into the local "warp and weft" directions (1, 2).

$$\begin{Bmatrix} \sigma_1 \\ \sigma_2 \\ \tau_{12} \end{Bmatrix} = [T_1] \begin{Bmatrix} \sigma_x \\ \sigma_y \\ \tau_{xy} \end{Bmatrix} \tag{7.1}$$

where $[T_1]$ is the stress transformation matrix (a second-order tensor)

$$[T_1] = \begin{bmatrix} m^2 & n^2 & 2mn \\ n^2 & m^2 & -2mn \\ -mn & mn & m^2 - n^2 \end{bmatrix} \tag{7.2}$$

where: $m = \cos(\theta)$, $n = \sin(\theta)$ and $\theta = 45^o$. Substituting Eq. 7.2 equation into Eq. 7.1 leads to the following system of equations (Eq. 7.3) for the stresses in principal "local" coordinate system which are the warp and weft directions respectively.

$$\begin{aligned} \sigma_1 &= m^2\sigma_x + n^2\sigma_y + 2mn\tau_{xy} \\ \sigma_2 &= n^2\sigma_x + m^2\sigma_y - 2mn\tau_{xy} \\ \tau_{12} &= -mn\sigma_x + mn\sigma_y + (m^2 - n^2)\tau_{xy} \end{aligned} \tag{7.3}$$

In the case of a bearing strength test, the global applied load is only axial ($\sigma_x \neq 0$) which reduces Eq. 7.3 to Eq. 7.4 in the local coordinate system (1, 2) as follows:

$$\begin{aligned} \sigma_1 &= m^2\sigma_x \\ \sigma_2 &= n^2\sigma_x \\ \tau_{12} &= -mn\sigma_x \end{aligned} \tag{7.4}$$

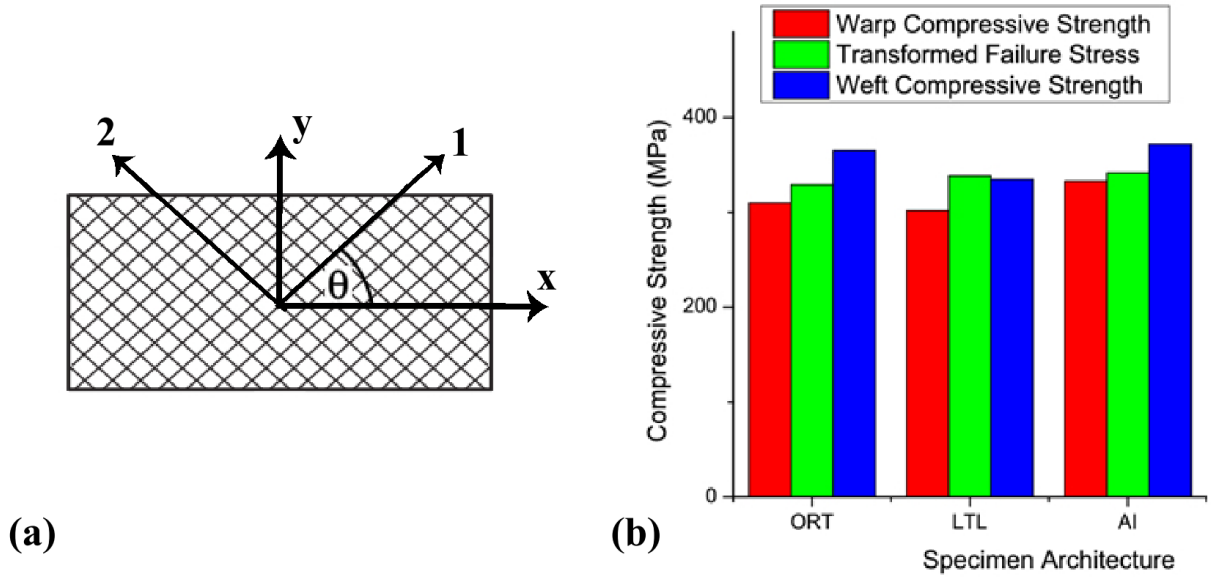

Figure 7.3 transformed bearing strength: (a) schematic, (b) comparison with compressive strength in warp and weft directions

Then, the transformed stresses obtained are compared against the ultimate compressive strength (see Fig. 7.3b) of the same material systems tested, in-house, along the warp and the weft directions in a standard compression test according to ASTM D3410 "Compressive Properties of Polymer Matrix Composite Materials with Unsupported Guage Section by Shear Loading". For all the tested architectures, the stress at failure in the local coordinate system "warp/weft" exceeds the strength of the material either in the warp or the weft directions (see Table 7.2) which leads to the final failure of the specimens.

Table 7.2 Comparison of transformed bearing strength against warp and weft compressive strength for ORT, LTL and AI

Textile architecture	Warp compressive strength (MPa)	Transformed bearing strength (MPa)	Weft compressive strength (MPa)
ORT	310 ± 4.18	329.33 ± 13.81	365.33 ± 4.5
LTL	302 ± 26.9	338.67 ± 11.48	335 ± 27.3
AI	333 ± 22.4	341.67 ± 4.70	372 ± 54.42

The next step is to investigate the bearing response of ORT, LTL and AI architectures up to final failure. Global bearing stress/bearing strain curves are

depicted in Fig. 7.4. Although there is no significant difference between all the architectures up to 50% strain, the response is quite different up to failure. It is clear that the LTL architecture fails first (~85% strain) followed by the AI (~105% strain) and finally ORT (~140% strain). This higher strain to failure is associated with higher energy absorption for ORT (~760 MJ/m^3) as opposed to AI (~590 MJ/m^3) and finally LTL (~490 MJ/m^3). This suggests that the damage progression is different depending on the 3D woven architecture. A similar trend was reported in [98] for testing 3D woven composites in tension in the off-axis direction. The smaller unit cell size in ORT redistributes the stress over a wider region of the specimen and resists cracking and delamination progression. Further understanding of the damage mechanisms is thus studied using X-ray CT in the following section.

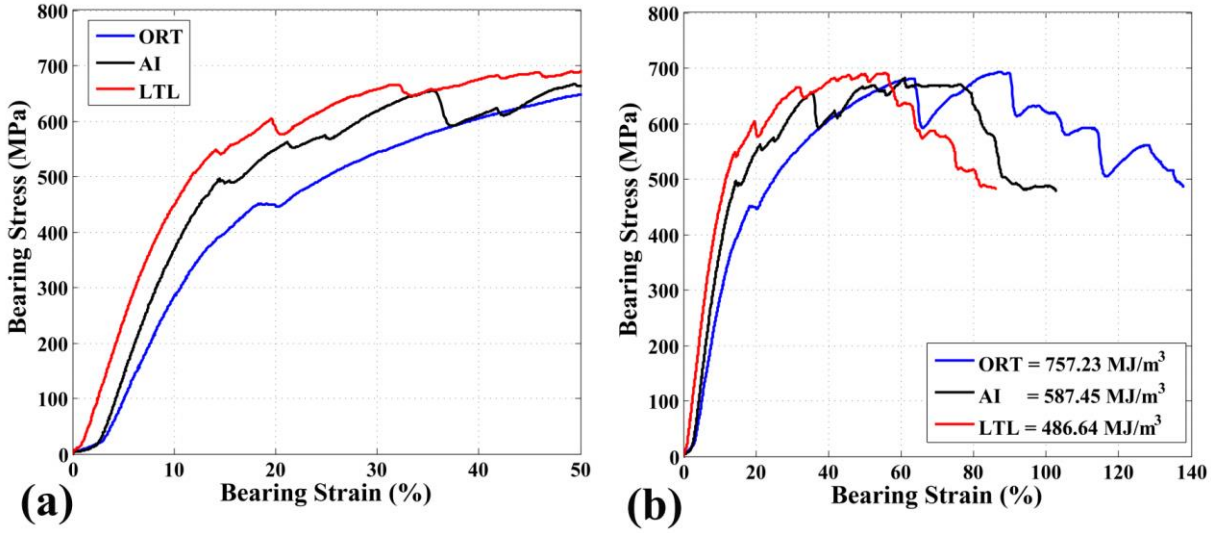

Figure 7.4 Bearing stress vs. bearing strain: (a) up to 50% strain, (b) failure strain

7.3.2 X-ray CT damage characterisation

To assess the level of damage and various damage mechanisms in the double-lap bearing strength test, X-ray CT was used. Specimens tested up to 50% strain are scanned as detailed in Section 7.2.2. To aid the damage analysis using X-ray CT, nomenclature of damage types is given in Table 7.3. A comparison between the damaged specimens and the X-ray front view for ORT, LTL and AI is shown in

Fig. 7.5. Although damage is not very obvious on the surface of the specimens, the X-ray images reveal more information. All specimens fail in a bearing failure mode (B-type) which is highlighted by the rectangular dashed frame (see Fig. 7.5d-f). Clear yarn distortion is experienced by the LTL architecture at the hole front tip (see Fig. 7.5b, e) while it is less severe in ORT (see Fig. 7.5a) and AI (see Fig. 7.5c). Transverse cracking (T-type) dominates the three architectures ORT, LTL and AI. However, the propagation length of the cracks seems to be architecture dependant "unit cell size". Transverse cracks propagate along the yarn longitudinal direction until they encounter a z-binder yarn; so the least cracking length is observed in ORT, followed by LTL and then AI. Once transverse cracking is suppressed by the z-binder yarns, another damage mechanism is observed in the form of z-binder induced damage (Z-type).

Table 7.3 Nomenclature of damage types in bearing strength test

Code	Damage type
F	Free edge matrix crack between yarns
Z	Z-binder induced damage
T	Transverse crack within yarns
D	Inter-yarn matrix delamination
M	Matrix Damage
B	Bearing Failure

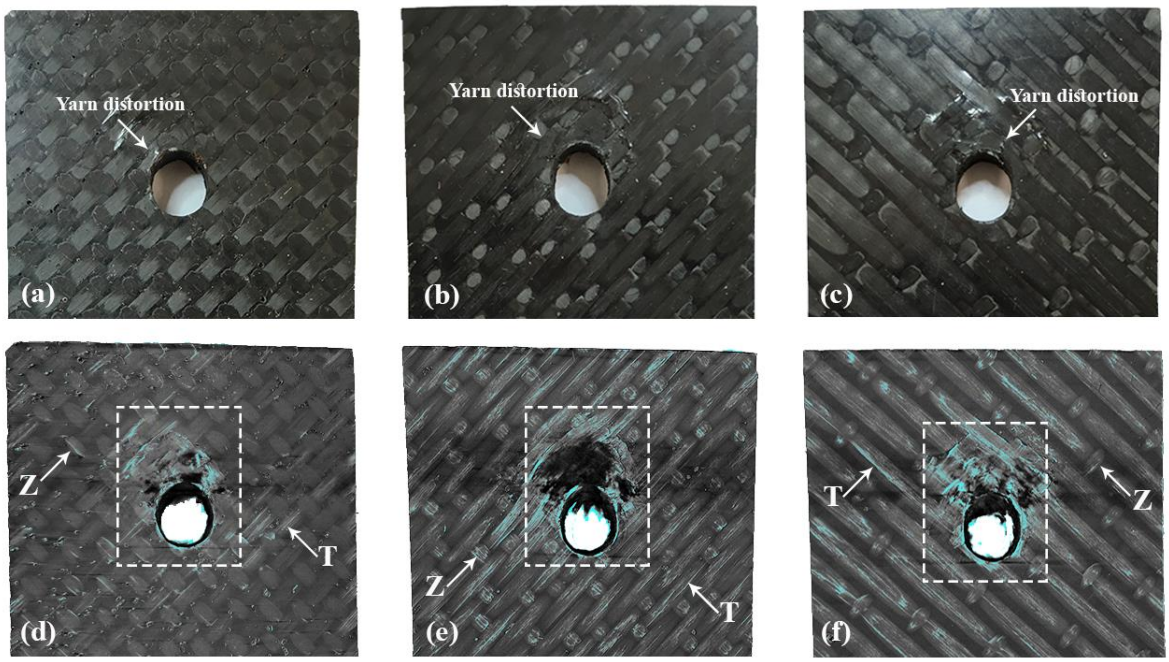

Figure 7.5 At 50% strain: (a, b, c) damaged specimens, (d, e, f) X-ray front view for ORT, LTL and AI respectively

After reconstruction of the 2D scanned slices, the 3D volume of the damage specimens is visualised in (Fig. 7.6b, d, f). The size of the B-type damaged region is largest in the LTL architecture, smaller in AI and smallest in ORT. Although all specimens are deformed with the same strain level, Fig. 7.6b, d, f suggests that ORT has the highest resistance to deformation followed by AI and finally LTL which supports the argument that the smaller ORT unit cell size redistributes the stress over a wider region and resists cracking and delamination progression.

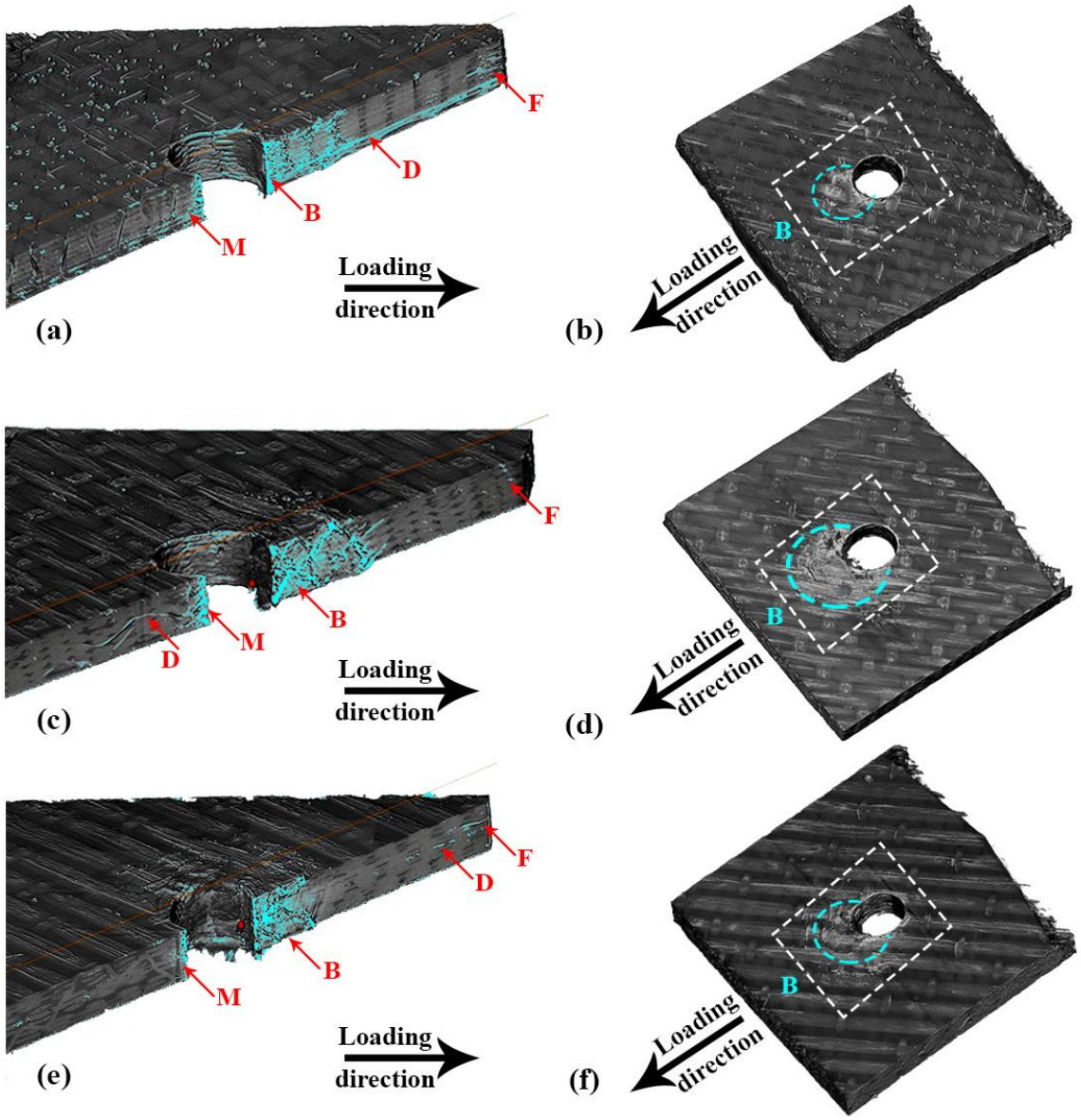

Figure 7.6 X-ray CT scans at 50% strain: (a, c, e) virtual sectioning along the warp direction, (b, d, f) isometric 3D volume for ORT, LTL and AI respectively

The next step is to virtually cut a sectioning plane along the warp direction to reveal the damage along the z-binder path (see Fig. 7.6b, d, f) in the 3D reconstructed volume. In all architectures, bearing failure with extensive matrix crushing and damage (type-M) is observed at the hole periphery in the loading direction "bearing plane". In addition, free edge cracking (type-F) is common in all architectures. In case of ORT (see Fig. 7.6a) and AI (see Fig. 7.6e), the through-thickness binder prevents the delamination (type-D) from growing across the width

of the specimen. However, the z-binding yarns in LTL (see Fig. 7.6c) guide the delamination (type-D) along their path. In regions where z-binding yarns do not exist, delamination (type-D) grows across the specimen width even in ORT and AI architectures. This indicates that the z-binder architecture plays a major role in determining the damage path in 3D woven composites and consequently their damage resistance and global stress/strain response.

7.4 Concluding Remarks

The double-lap bearing strength test has been conducted for ORT, LTL and AI architectures in the off-axis direction. Up to 50% bearing strain, no significant variation in the global bearing stress/bearing strain response was observed as all of them failed in a bearing failure mode. However, X-ray CT damage characterisation revealed the effect of the z-binder architecture on the damage mechanisms and delamination propagation. The dominant damage mechanisms were found to include matrix crushing, extensive delamination, transverse cracking and z-binder induced damage. Loading specimens up to failure showed that the ORT architecture in the off-axis direction resists deformation and damage progression followed by AI and finally LTL. This suggested that in addition to the unit cell size effect, having a through-thickness binder (ORT and AI) can suppress delamination and delay final failure. However, delamination progression is guided by the z-binding yarns between layers which led to final failure of the LTL architecture. This is reflected by the energy absorption of ORT being the highest followed by AI and finally LTL.

8 Micro-mechanics based damage model for 3D orthogonal woven composites

8.1 Introduction

Most of the modelling strategies adopted in the literature take one of three approaches to describe damage evolution and material degradation in 3D woven composites. Once a failure criterion is met, either knock down factors are introduced [1,86,89,90,151] or a penalty degradation function is defined [94,152]. In these two approaches, fitting parameters/modelling variables are defined to fit the experimental results obtained. The last approach is the continuum damage modelling (CDM) approach. In this approach, damage is depicted by an internal damage variable which has a continuous range from undamaged material (d=0) to a completely damaged material (d=1). The evolution of a constitutive relation requires experimental results to calibrate the damage evolution as a function of the damage driving force [30]. Thus, all the previously listed models use approaches in which the evolution laws are obtained by retrofitting global experimental observations. However, the objective of this study is to propose a damage evolution model obtained from micro-mechanical considerations and relies only on a few well-defined material parameters and to then validate it against experimental results.

To develop a damage mechanics model for composite materials, damage initiation criteria and damage evolution laws have to be specified for both composite constituents; yarns and matrix.

For matrix failure, a pressure dependent modified von Mises criterion [94] is used

(see Eq. 8.1)

$$F_m = \frac{S_m^c - S_m^t}{S_m^c S_m^t}(\sigma_1 + \sigma_2 + \sigma_3) + \frac{1}{2S_m^c S_m^t}[(\sigma_1 - \sigma_2)^2 + (\sigma_2 - \sigma_3)^2 + (\sigma_1 - \sigma_3)^2] \tag{8.1}$$

where σ_i with i =1, 2, 3 are the principal stresses and S_m^j with j = t, c are the tensile and compressive strengths of the matrix. The matrix is assumed to fail once the damage initiation parameter F_m exceeds 1.

For yarns, three damage mechanisms are considered: fibre breakage, transverse damage and shear diffused damaged. A maximum stress failure criterion is assumed for fibre longitudinal breakage; and it is only associated with reduction in longitudinal stiffness. The damage initiation criteria assumed are the critical energy release rates for the other two mechanisms (see Section 8.3.3). However, transverse cracking and shear diffused damage result in reduction of the transverse and the in-plane shear moduli respectively. Continuum damage mechanics (CDM) is used to derive the damage evolution laws, so the stiffness properties are degraded in a continuous manner as damage propagates in each constituent. Poisson's ratios ($\nu_{12}, \nu_{23}, \nu_{13}$) are assumed to remain constant.

8.2 Model considerations

To derive a damage evolution law for the yarns, the proposed model simplifies the 3D orthogonal (ORT) woven structure (see Fig. 8.1a) as a cross-ply laminate. The reasoning behind this simplification is that previous studies [20,24,44] have shown that the damage and cracking progression in 3D woven composites is very similar to cross-ply laminates when loaded uniaxially along the warp or the weft directions as detailed in Section 8.3.1. Another motivation for this assumption is that the in-plane properties of 3D orthogonal woven composites are not significantly affected by the binder removal as demonstrated in Table 8.1. Only the out-of-plane properties are significantly affected as the binder yarns provide through thickness reinforcement in the first place. Experimental results are provided in the table along with analytical approximation calculated by rule of mixture taking into account the directional fibre volume fraction in the warp, weft and binder directions. As an example for clarification, the Young's modulus along the warp direction is calculated as the fibre longitudinal modulus multiplied by the warp

volume fraction plus the fibre transverse modulus multiplied by the weft volume fraction plus the fibre transverse modulus multiplied by the binder volume fraction plus the matrix modulus multiplied by the matrix volume fraction. In the case of "without binder" calculations, the binder volume fraction is multiplied by the elastic modulus of the matrix. In other words, the matrix volume fraction is increased while the fibre volume fraction is only depicted by the warp and weft volume fractions. A fibre packing factor "volume fraction" inside yarns of ~75% is assumed for the rest of the simulation.

Table 8.1 Elastic properties of 3D orthogonal woven composite: Experimental vs Analytical

	Experiment	**With Binder**	**Without Binder**
E1 (GPa)	56.2 ± 0.78	58.54	58.29
E2 (GPa)	68.2 ± 3.71	69.17	68.92
E3 (GPa)	---	15.82	6.51
G12 (GPa)	2.98 ± 0.04	3.30	3.17
υ12	---	0.31	0.32

Thus, the model considers a warp/weft/warp laminate as described in Fig. 8.1b where h_f and h_w are the weft and warp layer thicknesses respectively.

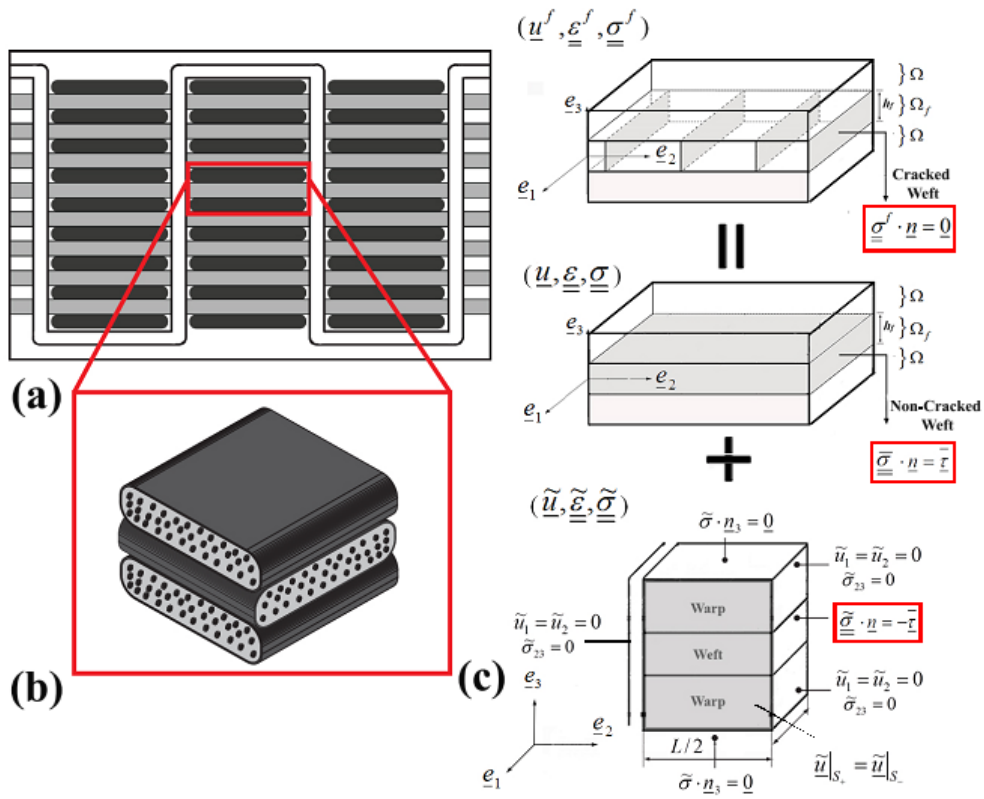

Figure 8.1 Schematic diagram of: (a) 3D orthognal woven composite unit cell, (b) cross-ply laminate simplification, (c) micromechanics reference problem

Both the weft and warp layers are assumed to be orthotropic expressed in the form of 4th order stiffness tensors $\underline{\underline{\underline{\underline{K}}}}_f^0$ and $\underline{\underline{\underline{\underline{K}}}}_w^0$ respectively. The laminate is subjected to a macroscopic in-plane strain $\underline{\underline{\varepsilon}}^p$ (with 1 being the fibre direction in the weft layer and 2 is the transverse direction):

$$\underline{\underline{\varepsilon}}^p = \varepsilon_{11}^p \underline{e}_1 \otimes \underline{e}_1 + \varepsilon_{22}^p \underline{e}_2 \otimes \underline{e}_2 + \varepsilon_{12}^p (\underline{e}_1 \otimes \underline{e}_2 + \underline{e}_2 \otimes \underline{e}_1) \tag{8.2}$$

Remark: The thermal residual stresses due to the manufacturing process are not described here, however they can be accounted for, if needed, by modifying the effective stress described in Section 8.3.

This laminate is then perturbed by a periodic network of transverse cracks quantified by a dimensionless cracking rate ρ ($\rho = h_f/L$, L being the average inter crack spacing) (Fig. 8.1c). Those cracks are assumed to extend through the

thickness of the weft layer and are infinite about the $\underline{e}_1$ direction.

8.3 Micro-mechanics damage model

In this part, the model for the multiplication of transverse and shear damage is derived, taking into account the geometrical and loading assumptions described earlier. Three steps are required for the model derivation. First, the structure of the mechanical fields (displacements, strains and stresses) in the cracked structure are highlighted. Second, the homogenisation step that defines an equivalent damage layer to the cracked one is explained in detail. Finally, the evolution laws, for transverse damage and shear damage under the loading described by Eq. 8.2, are derived.

8.3.1 Structure of the mechanical fields

Let $(\underline{u}^f, \underline{\underline{\varepsilon}}^f, \underline{\underline{\sigma}}^f)$ be the displacement field, the infinitesimal strain field and the Cauchy stress field in the cracked laminate when subjected to $\underline{\underline{\varepsilon}}^p$ (Fig. 8.1c). Also, $(\bar{\underline{u}}, \bar{\underline{\underline{\varepsilon}}}, \bar{\underline{\underline{\sigma}}})$ are assumed to be the displacement field, the infinitesimal strain field and the Cauchy stress fields in the uncracked laminate (the same structure without cracks) when subjected to $\underline{\underline{\varepsilon}}^p$ (Fig. 8.1c). Just as a naming convention, $(\bar{\underline{u}}, \bar{\underline{\underline{\varepsilon}}}, \bar{\underline{\underline{\sigma}}})$ are refered to, in this study, as the *"effective"* mechanical fields. Cracked surfaces are traction free surfaces($\underline{\underline{\sigma}}^f \cdot \underline{n} = \underline{0}$) in the actual damaged weft layer while in the case of a non-cracked weft layer, internal traction can be expressed as ($\bar{\underline{\underline{\sigma}}} \cdot \underline{n} = \bar{\underline{\tau}}$). So, the perturbation problem introduced should have the counter traction

($\tilde{\underline{\underline{\sigma}}} \cdot \underline{n} = -\bar{\underline{\tau}}$) experienced by the non-cracked layer, to end up simulating the traction free surfaces in the cracked weft layer.

Thus, the solution of the actual cracked laminate $(\underline{u}^f, \underline{\underline{\varepsilon}}^f, \underline{\underline{\sigma}}^f)$ can be written as the superposition (Fig. 8.1c) of the non-cracked laminate solution $(\bar{\underline{u}}, \bar{\underline{\underline{\varepsilon}}}, \bar{\underline{\underline{\sigma}}})$ and

the periodic perturbation solution ($\underline{\tilde{u}}, \underline{\underline{\tilde{\varepsilon}}}, \underline{\underline{\tilde{\sigma}}}$) induced by the transverse cracks such that:

$$\underline{u}^f = \underline{\bar{u}} + \underline{\tilde{u}} \quad ; \quad \underline{\underline{\varepsilon}}^f = \underline{\underline{\bar{\varepsilon}}} + \underline{\underline{\tilde{\varepsilon}}} \quad ; \quad \underline{\underline{\sigma}}^f = \underline{\underline{\bar{\sigma}}} + \underline{\underline{\tilde{\sigma}}} \tag{8.3}$$

So, the problem now is reduced to solving the residual "perturbation" problem (Fig. 8.1c) to determine how the stiffness tensor of the weft layer evolves with increasing crack density in the yarns as will be highlighted in the following section.

8.3.2 Strain energy density and homogenisation of the damaged layer

The homogenisation approach utilised here was initially proposed by [153], and then developed in [109,113,154] for the analysis of transverse cracking in laminated composites. This technique can be extended to the proposed framework. The key points of this approach are highlighted here, however extensive details and related proofs are contained in the original publication[153].

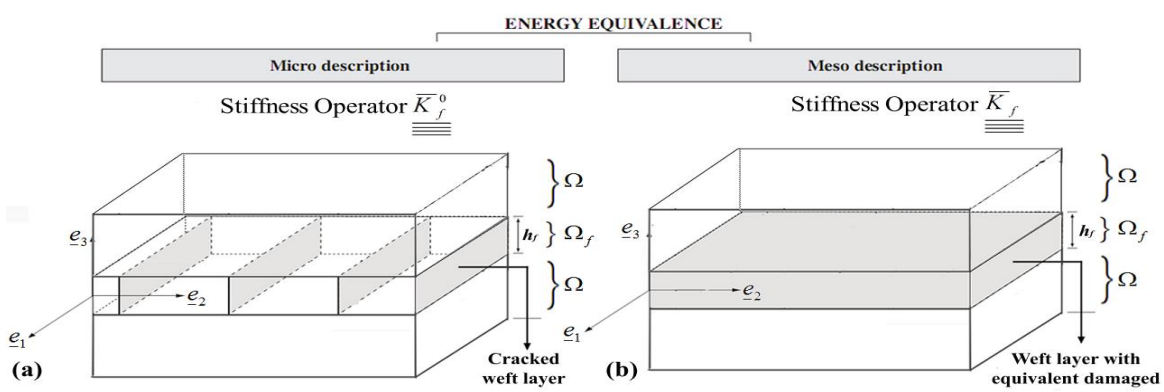

Figure 8.2 Micro-meso energy equivalence: (a) actual damaged weft layer, (b) homogenised weft layer with reduced stiffness

Following this technique, the cracked weft layer (see Fig. 8.2a) can be replaced by an equivalent layer, homogeneous but with mechanical damage (see Fig. 8.2b). The criterion of this homogenisation process is that the total strain energy of the new

laminated structure (see Fig. 8.2b) is equal to the strain energy of the initial cracked structure (see Fig. 8.2a), when subjected to $\underline{\underline{\varepsilon}}^p$. From [153,154] , the strain energy density e_f of the equivalent weft layer is written:

$$e_f = e_f^0 - [\frac{f_+(\bar{\sigma}_{11})d_f}{2E_{11f}^0}\bar{\sigma}_{11}^2 + \frac{f_+(\bar{\sigma}_{22})d_t}{2E_{22f}^0}\bar{\sigma}_{22}^2 + \frac{d_s}{2G_{12f}^0}\bar{\sigma}_{12}^2] \tag{8.4}$$

where:

- e_f^0 is the *effective strain energy density* (the strain energy density of the undamaged weft layer experiencing the effective fields $(\underline{\underline{\bar{\varepsilon}}}, \underline{\underline{\bar{\sigma}}})$):

$$e_f^0 = \frac{1}{2}\underline{\underline{\bar{\sigma}}} : \underline{\underline{\underline{\underline{K_f^0}}}}^{-1} : \underline{\underline{\bar{\sigma}}} \tag{8.5}$$

- $\bar{\sigma}_{11}$ is the *effective longitudinal stress* in the weft layer ($\bar{\sigma}_{11} = \underline{e}_1 \cdot \underline{\underline{\bar{\sigma}}} \cdot \underline{e}_1$)
- $\bar{\sigma}_{22}$ is the *effective transverse stress* in the weft layer ($\bar{\sigma}_{22} = \underline{e}_2 \cdot \underline{\underline{\bar{\sigma}}} \cdot \underline{e}_2$)
- $\bar{\sigma}_{12}$ is the *effective shear stress* in the weft layer ($\bar{\sigma}_{12} = \underline{e}_1 \cdot \underline{\underline{\bar{\sigma}}} \cdot \underline{e}_2$)
- $f_+(\cdot)$ is defined as:

$$\forall x \in R, \quad f_+(x) = \frac{x + |x|}{2} \tag{8.6}$$

where $|\cdot|$ is the absolute value function and R the real numbers space. This function accounts for crack closure effects (the mechanical damage associated with cracks vanishes when those cracks get closed).

- d_f, d_t , d_s are the internal variables that quantify longitudinal, transverse and shear damage respectively. E_{11f}^0, E_{22f}^0, G_{12f}^0 are the longitudinal, transverse and in-plane shear moduli of the non-cracked weft layer.

Fibre breakage failure is simulated as brittle fracture so direct reduction of longitudinal stiffness is assumed ($d_f = 0.999$) while damage evolution for the transverse and shear damage mechanisms is detailed here. The derivation details first the damage evolution law for transverse loading (Only $\bar{\sigma}_{22} \neq 0$) followed by the shear loading (Only $\bar{\sigma}_{12} \neq 0$).

For transverse damage, d_t depends on ρ through a bijective function $\mathbf{c}_t$, such that:

$$\forall \rho \in R^+, \quad d_t = \mathbf{c}_t(\rho) \tag{8.7}$$

Function $\mathbf{c}_t$ is calculated by solving the residual problem defining the periodic perturbation ($\underline{u}, \underline{\underline{\varepsilon}}, \underline{\underline{\sigma}}$) over the periodic cracked cell. $\mathbf{c}_t^{-1}$ is defined as the reciprocal function of $\mathbf{c}_t$, and $\mathbf{c}_t'$ as the derivative of $\mathbf{c}_t$ such that:

$$\forall \rho \in R^+, \quad \mathbf{c}_t^{-1}(\mathbf{c}_t(\rho)) = \rho \quad ; \quad \mathbf{c}_t'(\rho) = \frac{d\mathbf{c}_t}{d\rho}(\rho) \tag{8.8}$$

From Eq. 8.4 and 8.5, e_f can be rewritten in terms of the effective stress to derive the damage evolution law as needed in Section 8.3.3:

$$e_f = \frac{1}{2}\underline{\underline{\bar{\sigma}}} : \left(\underline{\underline{\underline{\underline{K}}}}_f^{0\,-1} - \frac{f_+(\bar{\sigma}_{22}) d_t}{E_{22f}^0} \underline{e}_2 \otimes \underline{e}_2 \right) : \underline{\underline{\bar{\sigma}}} \tag{8.9}$$

However, it is also convenient to rewrite the strain energy density as a function of the stress in the equivalent damaged layer, as this defines the effective stiffness of this layer. Denoting $\underline{\underline{\sigma}}$ as the stress in the equivalent damaged layer when the structure is subjected to the in-the-plane extension $\underline{\underline{\varepsilon}}^p$ (Fig. 8.2b). Then, introducing $\underline{\underline{\underline{\underline{\bar{K}}}}}_f^0$ as the plane-stress stiffness operator for the undamaged layer, and

$\overline{\underline{\underline{\underline{\underline{K}}}}}_f$ as the plane-stress stiffness operator for the damaged layer, stresses can be expressed as:

$$\overline{\underline{\underline{\sigma}}} = \overline{\underline{\underline{\underline{\underline{K}}}}}_f^0 : \underline{\underline{\varepsilon}}^p \quad ; \quad \underline{\underline{\sigma}} = \overline{\underline{\underline{\underline{\underline{K}}}}}_f : \underline{\underline{\varepsilon}}^p \tag{8.10}$$

Introducing Eq. 8.10 into Eq. 8.9, then:

$$e_f = \frac{1}{2} \underline{\underline{\sigma}} : \overline{\underline{\underline{\underline{\underline{K}}}}}_f^{-1} : \underline{\underline{\sigma}} \tag{8.11}$$

where

$$\overline{\underline{\underline{\underline{\underline{K}}}}}_f = \overline{\underline{\underline{\underline{\underline{K}}}}}_f^0 : \left(\underline{\underline{\underline{\underline{K}}}}_f^{0\,-1} - \frac{f_+(\overline{\sigma}_{22}) d_t}{E_{22f}^0} \underline{e}_2 \otimes \underline{e}_2 \right) : \overline{\underline{\underline{\underline{\underline{K}}}}}_f^0 \tag{8.12}$$

Eq. 8.12 directly defines the stiffness operator of the equivalent damaged layer as function of the transverse cracks induced damage d_t.

8.3.3 Micro-mechanics based damage evolution

The strain energy density defined by Eq. 8.9 is now used as a potential to derive the cracking evolution law. First, the damage force Y_{d_t} that drives the damage progression is defined. Then, the damage evolution law, that relates d_t to the damage evolution force Y_{d_t}, is calculated.

- *The damage force:* the damage force is the derivative of e_f with respect to d_t at constant effective stress.

$$Y_{d_t} = -\frac{\partial e_f}{\partial d_t} \Big|_{\overline{\underline{\underline{\sigma}}}} = f_+(\overline{\sigma}_{22}) \frac{\overline{\sigma}_{22}^2}{2E_{22f}^0} \tag{8.13}$$

- *The damage evolution:* the cracking evolution is obtained by calculating the energy release rate G of the structure when cracks multiply. This is

a classical approach in the micro-mechanics of laminated composites [109]. In this case, a continuous definition of G is obtained as a function of the continous variable ρ such that:

$$G(\rho) = -\frac{\partial U}{\partial A}(\rho) \tag{8.14}$$

U is the potential energy of the structure and A is the total area of cracks. At constant effective stresses, G can be expressed as a function of the total strain energy of the structure, E:

$$G = -\frac{\partial U}{\partial A} = -\frac{\partial E}{\partial A}|_{\overline{\underline{\underline{\sigma}}}} \tag{8.15}$$

Remarks: $E = E_f + E_w$, where E_f is the total strain energy in the weft layer and E_w is the total strain energy in the warp layer (2) E_w is constant when the effective stress $\overline{\underline{\underline{\sigma}}}$ is kept constant. So,

$$G = -\frac{\partial(E_f + E_w)}{\partial A}|_{\overline{\underline{\underline{\sigma}}}} = -\frac{\partial E_f}{\partial A}|_{\overline{\underline{\underline{\sigma}}}}$$

$$= |\Omega_f| \frac{\partial e_f}{\partial d_t} \mathbf{c}_t'(\rho) \frac{d\rho}{dA} = |\Omega_f| \frac{f_+(\overline{\sigma}_{22})\overline{\sigma}_{22}^2}{2E_{22f}^0} \mathbf{c}_t'(\rho) \frac{d\rho}{dA} \tag{8.16}$$

where $|\Omega_f|$ is the volume of the weft layer. Considering the relation between the volume of the weft layer, its thickness, the cracking rate and the total cracked area ($A = \rho|\Omega_f|/h_f$), Eq. 8.16 can be further simplified to:

$$G = h_f \frac{f_+(\overline{\sigma}_{22})\overline{\sigma}_{22}^2}{2E_{22f}^0} \mathbf{c}_t'(\rho) \tag{8.17}$$

Cracks multiply when G equals the fracture toughness G_f that represents the resistance of the weft layer to transverse cracking. Then, considering Eq. 8.13, and from Eq. 8.17 during crack multiplication:

$$G_f = h_f Y_{d_t} \mathbf{c}_t^{'}(\rho) \tag{8.18}$$

The equilibrium during cracking described by Eq. 8.18 can be turned into a meso scale evolution law for d_t. This would define the following pseudo-potential of dissipation f for the evolution of the meso scale damage variable d_t:

$$f(Y_{d_t}, d_t) = f_1(Y_{d_t}) - f_2(d_t) \tag{8.19}$$

$$f_1(Y_{d_t}) = Y_{d_t} \tag{8.20}$$

$$f_2(d_t) = \frac{G_f}{h_f \mathbf{c}_t^{'}(\mathbf{c}_t^{-1}(d_t))} \tag{8.21}$$

To conclude this part, the transverse cracking evolution can be fully replaced by the calculation of the evolution of the equivalent variable d_t. The evolution law of d_t is a classical damage evolution law based on the pseudo-potential defined by Eq. 8.19.

Similarly, to derive the damage evolution law of shear damage within a yarn, in Eq. 8.4, normal stress $\bar{\sigma}_{22}$ is set to zero and only shear stress $\bar{\sigma}_{12}$ is considered instead. The shear damage evolution law can be defined in a similar manner to Eq. 8.19. Here, those damage evolution laws (Fig. 8.3) are obtained from micro mechanical considerations and rely on a few well-defined material parameters. This largely differs from classical damage mechanics approaches in which the evolution law is obtained by retrofitting global experimental observations.

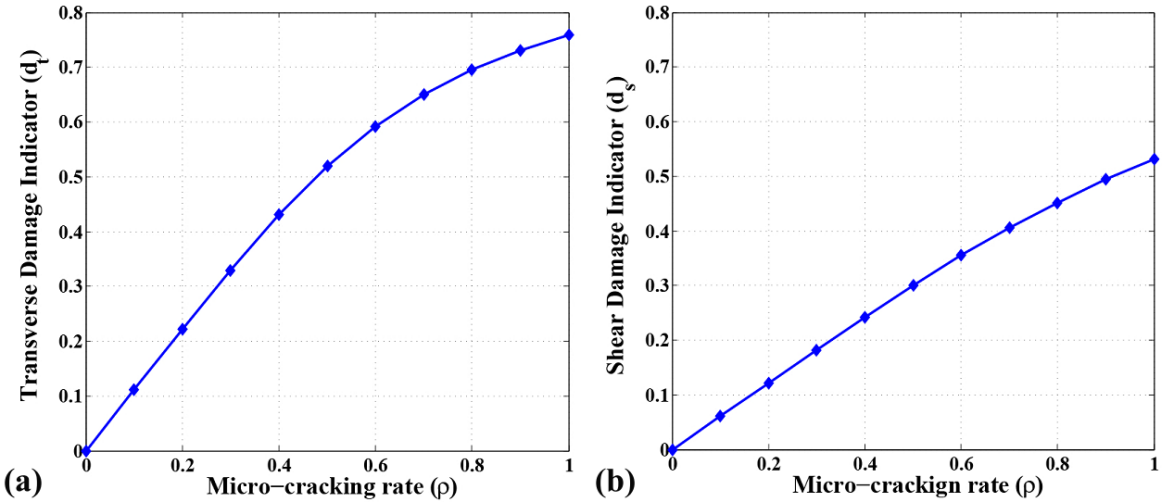

Figure 8.3 Damage evolution as a function of crack density: (a) transverse damage indicator, (b) shear damage indicator

After obtaining the damage evolution laws as a function of the micro-cracking rate, they can be correlated with the applied strain (Fig. 8.4) via the energy release rate [155] for transverse cracking and shear diffused damage respectively. Finally, those damage evolution laws are incorporated into a UMAT subroutine in ABAQUS Standard to simulate the damage evolution law for individual yarns.

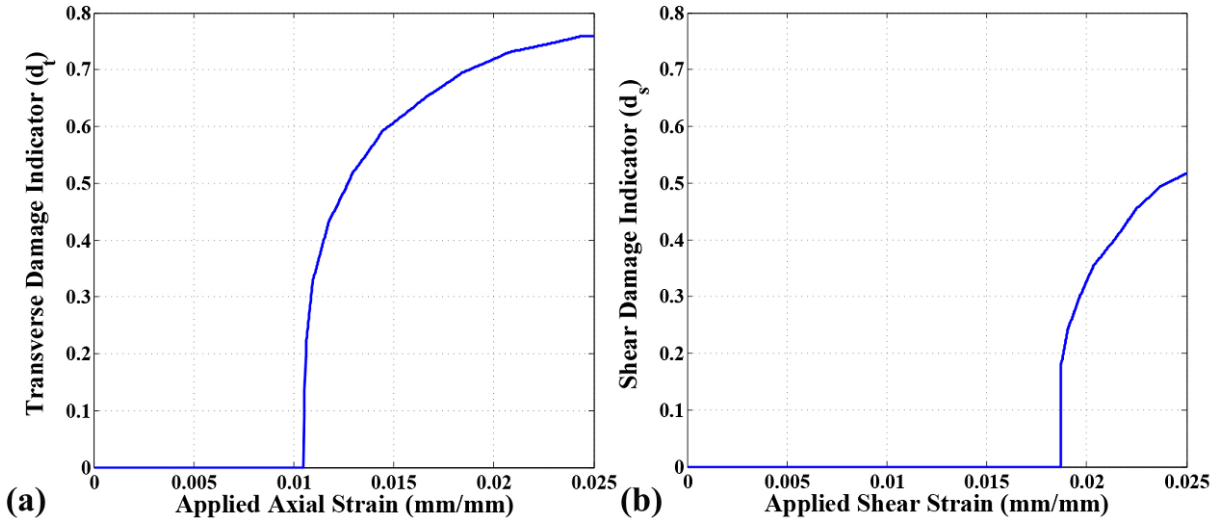

Figure 8.4 Damage evolution as a function of applied strain: (a) Transverse damage indicator, (b) Shear damage indicator.

The unit cell model used for the simulation was produced by TexGen software. Dimensions of the warp, weft and z-binder yarns as well as the spacing between yarns were measured from the X-ray CT scans (see Section. 3.4)

8.4 Results and Discussion

8.4.1 Stress strain curves

The total fibre volume fraction measured experimentally was 51.35 ± 0.45 % with 2.63 ± 0.02 % void content. Specimens were tested along the warp 0º and weft 90º directions up to failure. The global stress/strain behaviour of the orthogonal woven composite (Fig. 8.5a) shows a repeatable response of specimens tested along either the warp or the weft direction. However, the material seems to be stiffer along the weft direction as well as having higher strength and strain to failure. The stiffness (Fig. 8.5a) measured along the weft and warp directions is 68.2 ± 3.71 GPa and 56.2 ± 0.78 GPa respectively. Similarly, the strength along the weft direction is 849 ± 26.14 MPa compared to 704 ± 14.78 MPa along the warp. This is due to the different fibre volume fraction in the warp (21.57%) and weft (26.00%) directions.

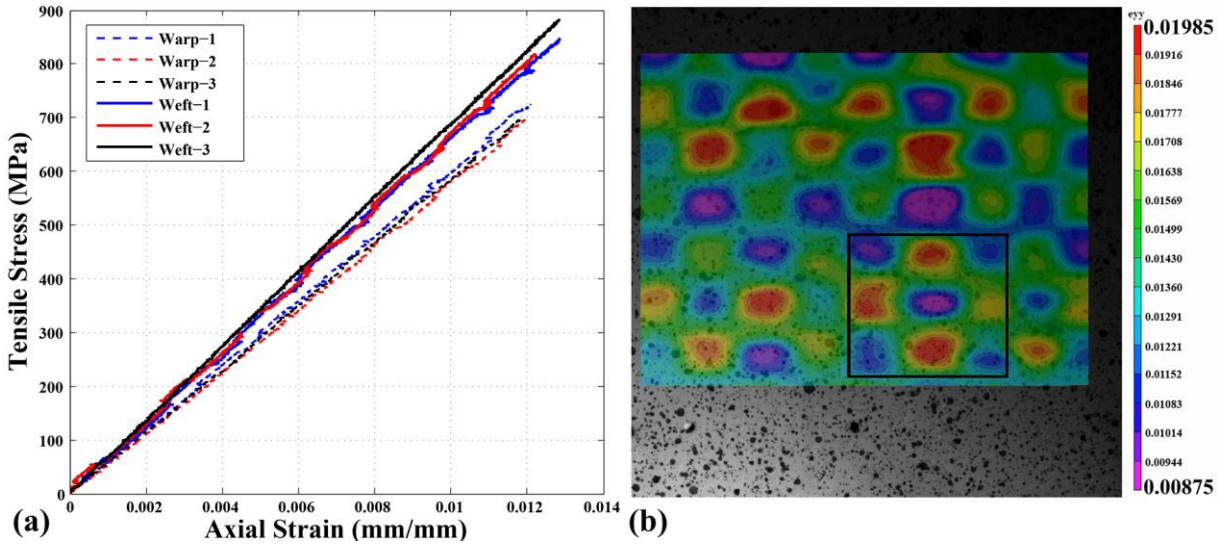

Figure 8.5 3D orthogonal woven composite: (a) stress strain curves, (b) DIC strain contour at failure with unit cell highlighted in the black frame

8.4.2 DIC Results

Digital Image Correlation (DIC) was mainly used as a non-contact strain measurement technique during testing. The strain contours over the specimen's surfaces are plotted in Fig. 8.5b. However, in the testing of the 3D woven composites it was even more utilised to identify the unit cell for the tested architectures. The orthogonal woven composite has a unit cell (Fig. 8.5b) with approximate dimensions of 5 x 5 mm. The periodicity of the weaving pattern makes it useful for the modelling and simulation to be verified against the DIC strain contours in case the asymptotic expansion homogenisation "periodic homogenisation" is implemented [30,90,100,156]. One advantage of utilising the DIC is for the determination of stress localisation regions which are mainly the interlacement points between the binding yarns and the warp and weft yarns. Those colour maps as well as the DIC images (Fig. 8.5b) were captured at failure. Although the global strain to failure reported in (Fig. 8.5a) varies between 1.2 to 1.3% strain, the stress localisation regions experience much higher strains (~2%).

8.4.3 Micro-mechanical modelling

8.4.3.1 Damage progression

The predicted damage evolution for the ORT unit cell loaded along the warp direction (x-axis) is shown in Fig. 8.6. Previous studies [20,24,44] have proven, experimentally, that the damage and cracking progression in 3D woven composites is very similar to cross-ply laminates when loaded uniaxially along the warp or the weft directions. The damage starts first at the interlacement points (Fig. 8.6a) between the z-binder and the in-plane yarns "warp and weft". Following this stress localisation effect, in-plane yarns, perpendicular to the loading direction, start experiencing transverse cracking (Fig. 8.6b-d), which is characterised by cracks spanning the whole yarn length and multiplying in number within the yarn up to a saturation point. The damage mechanism changes to delamination between the in-plane yarns that happens at the very last stage of the loading, just before the longitudinal fibre breakage (Fig. 8.6e-f) of the yarns. Damage progression has been

captured with the proposed model and correlates well with the experimental observations reported in literature.

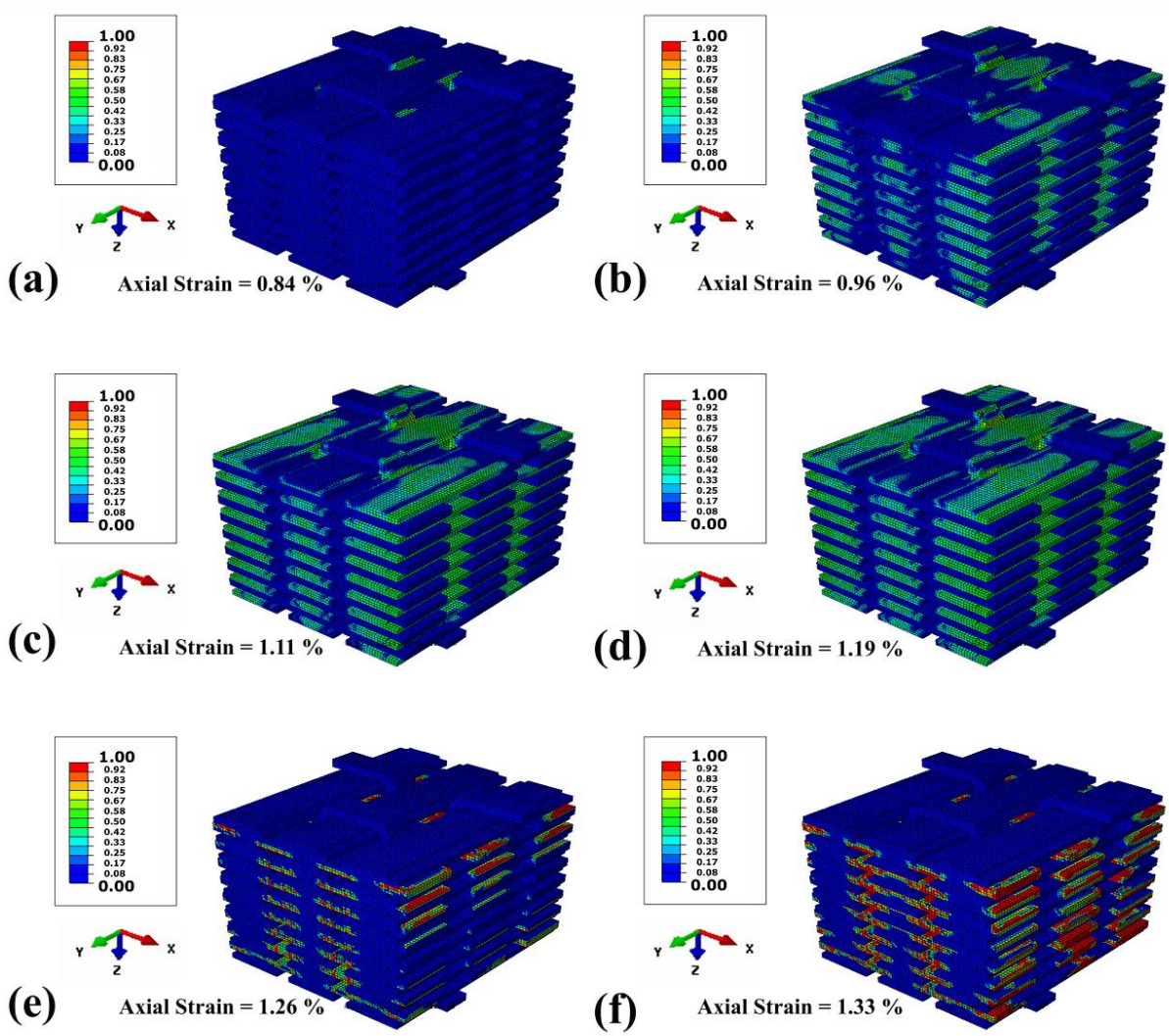

Figure 8.6 Damage progression: (a) binder localised damage, (b-d) transverse damage in weft yarns, and (e-f) fibre breakage in warp yarns

8.4.3.2 Global stress strain response

Experimental stress/strain curves for specimens tested in the warp (Fig. 8.7a) and weft (Fig. 8.7b) directions are plotted in solid lines while the model prediction is in dashed lines. In both testing directions, the predicted response overestimates the actual response of the material. This is due to the fact that the model does not

take into account the geometrical distortions of the ORT due to compaction and yarn waviness.

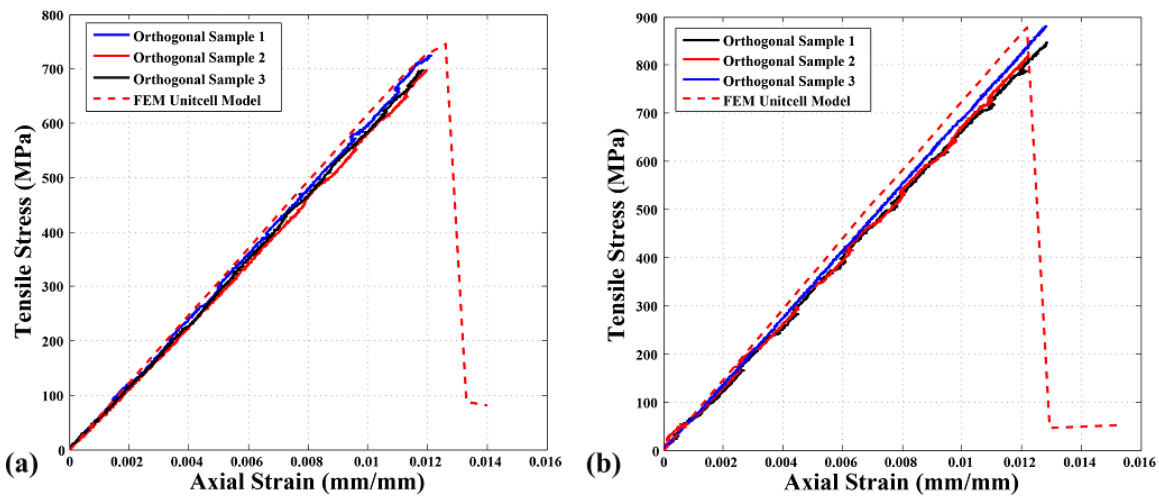

Figure 8.7 Stress strain curves for the model vs. experimental results: (a) along warp direction, (b) along weft direction

The global stress strain response of the ORT loaded uni-axially along the warp and the weft direction does not demonstrate significant reduction of the axial modulus. However, the effect of transverse cracking in the weft (Fig. 8.8a) and warp (Fig. 8.8b) layers on the elastic material properties of the ORT unit cell suggests that although the matrix cracking doesn't affect the axial modulus, less than 5% (a fibre dominated property), a 20% reduction in shear modulus is observed for the same amount of cracks at failure.

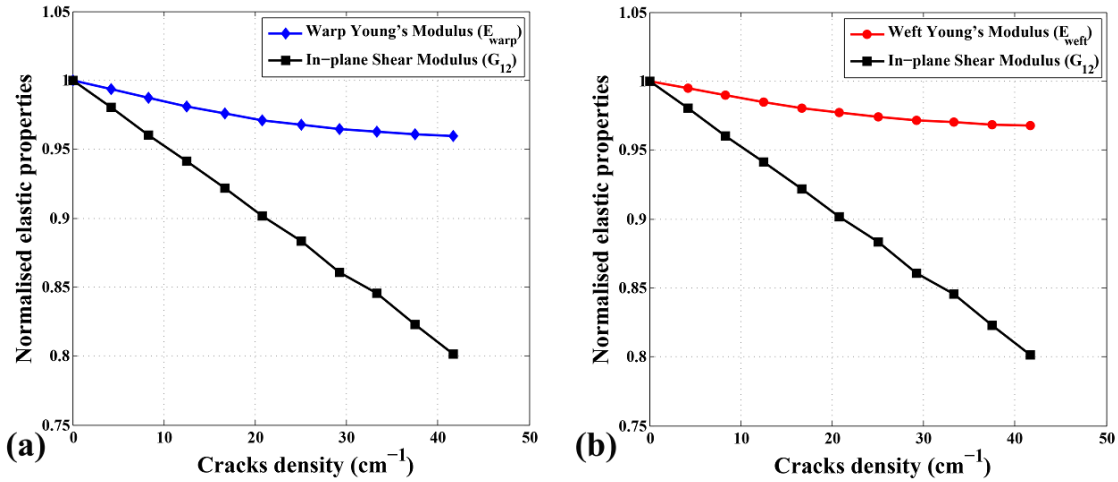

Figure 8.8 Prediction of normalised elastic properties due to transverse cracking in (a) weft yarns, (b) warp yarns

In order to evaluate the efficiency of the model, Table 8.2 summarises the key comparison parameters as well as the margin of error in the model. Although the model is a simplified model, yet it can capture, with less than a 10% margin of error, the global behaviour of the ORT tested in uniaxial tension. The main advantage of the model is that it only relies on well-defined material parameters with no need for any fitting or calibration constants.

Table 8.2 Comparison between experimental and modelling results

Parameter	Warp			Weft		
	Experiment	Model	Error (%)	Experiment	Model	Error (%)
Young's Modulus (GPa)	56.2 ± 0.78	61.2	8.9	68.2 ± 3.71	73.4	7.3
Tensile Strength (MPa)	704 ± 14.78	745	5.9	849 ± 26.14	879	3.5
Failure Strain (%)	1.19 ± 0.01	1.26	5.8	1.26 ± 0.03	1.21	3.9

The proposed model does not take into account the effect of void content as well as the actual compacted structure after manufacturing. In addition, in deriving the damage evolution law for transverse damage and shear damage, it assumes

implicitly equal crack spacing by calculating the average micro-cracking rate. Those model limitations can be improved further by implementing an image based FEM model using the reconstructed 3D geometry from the X-ray CT. This definitely will increase the computational cost but should lead to more accurate and conservative results. Using a voxel meshing technique in this model is not the most suitable approach to capture the damage initiation and localisation as sharp edges are susceptible to stress concentration. Some techniques for smoothing those stress concentrations out and effectively characterise damage on the meso-scale level have been investigated by Fang *et al.* and Doitrand *et al.* in [157,158]. To account for the viscoelastic nature of the matrix, more advanced plasticity models should be incorporated as well. The scope of this work was to establish the basis for the damage evolution laws as a function of the material parameters of the yarns and the recommended model improvements will be the focus of future work for off-axis tension simulation.

8.5 Concluding Remarks

The aim of this study was to provide a predictive micro-mechanical model capable of simulating the tensile response of ORT loaded along the warp or the weft direction. The proposed model differs from previous models introduced in the literature in the sense that damage evolution laws are defined only using material parameters rather than using penalty functions or fitting degradation schemes. The effect of transverse cracking and shear diffused damage on the in-plane transverse modulus and shear modulus were investigated for yarns while one failure criterion was introduced to simulate the matrix damage "cracking". Although the proposed model simplifies the ORT unit cell as a cross-ply laminate, deviation from experimental results was in the range of 10% difference and managed to capture the damage evolution in the binder, weft and warp yarns as proposed by experimental work in the literature. DIC was used to evaluate the surface strain contours during testing. The strain contour distribution demonstrated clearly the stress localisation at interlacement points and the periodicity of the weaving

architecture. In addition, an X-ray CT scan was conducted on undamaged specimen to visualise the "as-manufactured" panel and capture all the geometrical distortions due to waviness and fabric compaction. The predicted values from the model overestimated the experimental response of the tested specimens as it did not include the effect of geometrical distortions and void content. This opens an opportunity for improvement of the model using image-based FEM and incorporating plasticity models to account for the viscoelasticity of the matrix. This study provides more efficient and predictive capabilities to existing unit cell models, which in turn reduces the need for extensive experimental characterisation, with a high level of confidence in the modelling results.

9 Conclusions and Recommendations

9.1 Introduction

Three-dimensional (3D) woven composites are becoming of prime interest to the aerospace, automotive and military industries thanks to their enhanced out-of-plane properties, damage resistance and the potential for using the textile technology to automate the production of near net-shape preforms with minimal wastage. However, most of the research focused on characterising the out-of-plane response of those material systems while less work is available for characterising their in-plane response especially in the off-axis direction. Therefore, the aim of this study was to investigate the loading direction sensitivity and the effect of the z-binder architecture by characterising the electromechanical behaviour of three different architectures of 3D woven composites "orthogonal (ORT), layer-to-layer (LTL) and angle interlock (AI)" loaded, in three different orientations "warp (0°), weft (90°) and off-axis (45°)", in tension. Damage initiation and evolution up to final failure was examined using X-ray CT imaging. Then, the obtained results from this analysis were used to investigate the potential of using 3D woven composites loaded off-axially in composite joint applications by carrying out open-hole tension and "single fastener double-lap joint" bearing strength testing. Finally, a micro-mechanics based damage model was proposed to predict the tensile response of 3D orthogonal (ORT) woven composites. All the findings and accomplishments of this research are summarised in the next section followed by the recommendations for future work.

9.2 Conclusions

9.2.1 Tensile properties

Three different architectures of 3D woven composites (orthogonal, ORT; layer-to-layer, LTL; angle interlock, AI) were characterised in terms of on-axis and off-axis

mechanical properties and the influence of z-binder architecture. Regardless of the weaving architecture type, the stiffness and tensile strength of 3D woven composites under on-axis loading mainly depends on the directional fibre volume fraction of warp and weft yarns. Among all textile architectures, 3D orthogonal woven composites exhibit the best performance (highest failure strength and failure strain) under off-axis loading due to the interlocking mechanism provided by the z-binder. This interlocking mechanism increases the rotation angle of warp and weft yarns, and thus the ability of the yarns to bear extensive off-axis strain. Moreover, as the ORT specimen has smaller unit cell size, this enables the stress redistribution over a longer span of the specimen, and prevents slippage between in-plane yarns. So, the damage is uniformly distributed all over the gauge length of the specimen. The 3D orthogonal woven composites exhibit the highest energy absorption among other architectures during off-axis loading, which paves the road for their use in the energy-based design of composite structures.

9.2.2 Electrical resistance monitoring

Through a systematic experimental study, electrical resistance monitoring has been proven to have the potential not only for detecting damage initiation but also for tracking damage evolution in 3D woven composites tested in both on-axis and off-axis directions. The effect of the through-thickness binder is clearly identified as the initial resistances of the specimens are architecture dependent. For on-axis loaded specimens, the resistance increase due to damage in the transverse yarns and delamination can still be detected using the 4-probe technique as the resistance increase is around 20%. The resistance increase for the off-axis loaded specimens is much higher than for on-axis counterparts as it reaches approximately 90%. Out of all the 3D woven architectures, 3D orthogonal woven composites loaded off-axially exhibit a recovery in electrical conductivity which indicates that yarn realignment reached a point where the yarns become connected again and resistance drops accordingly. For all the off-axis tested specimens, the resistance increase upon unloading is irreversible which proves that the resistance increase is due to actual damage in the tested specimens, not due to the piezo-resistive effect. In cyclic

loading tests, during unloading the resistance drop is small due to the piezo-resistive nature of the material. However, during reloading the resistance drops due to fibre/yarns realignment up to a point at which the effect of induced damage becomes more significant than the recovery due to the realignment process. That is why the resistance starts increasing again. The remaining challenge for electrical resistance monitoring would still be the capability of localising and sizing the damage in 3D woven composites.

9.2.3 Open hole tension

The notched response of 3D woven composites, in the off-axis orientation, has been studied by open hole tension according to the ASTM standard. The global stress strain response suggests that all 3D woven architectures (ORT, LTL, and AI) are notch insensitive. The final failure of all the 3D woven architectures in the off-axis direction is progressive failure not catastrophic brittle fracture. Out of all the tested architectures, the ORT architecture in the off-axis orientation exhibits higher ultimate strength and strain to failure as was the case for the un-notched specimens. From the DIC analysis, the ORT architecture redistributes the stress over a wider region away from the hole which reduces the stress concentration at the notch periphery. In addition, the higher intensity of binding yarns acts as a crack stopper for delamination and matrix cracking. Thus, 3D woven composites in the off-axis orientation, especially ORT, demonstrate the potential for overcoming some of the major challenges for composite joint applications which are pseudo-ductility, stress redistribution away from the notch and notch insensitivity.

9.2.4 Bearing strength

The double-lap bearing strength test has been conducted for ORT, LTL and AI architectures in the off-axis direction. Up to 50% bearing strain, no significant variation in the global bearing stress/bearing strain response was observed as all of them failed in a bearing failure mode. However, X-ray CT damage characterisation revealed the effect of the z-binder architecture on the damage mechanisms and on delamination propagation. The dominant damage mechanisms were found to

include matrix crushing, extensive delamination, transverse cracking and z-binder induced damage. Loading specimens up to failure showed that the ORT architecture in the off-axis direction resists deformation and damage progression followed by AI and finally LTL. This suggested that in addition to the unit cell size effect, having a through-thickness binder (ORT and AI) can suppress delamination and delay final failure. On the contrary, delamination progression is guided by the z-binding yarns between layers which led to final failure of the LTL architecture. This is reflected by the energy absorption of ORT being the highest followed by AI and finally LTL.

9.2.5 Micro-mechanics model

The effect of transverse cracking and shear diffused damage on the in-plane transverse modulus and shear modulus was investigated for yarns while one failure criterion was introduced to simulate the matrix damage "cracking". Although the proposed model simplifies the ORT unit cell as a cross-ply laminate, deviation from experimental results was in the range of 10% difference and managed to capture the damage evolution in the binder, weft and warp yarns as proposed by experimental work in the literature. DIC was used to evaluate the surface strain contour during testing. The strain contour distribution demonstrated clearly the stress localisation at interlacement points and periodicity of the weaving architecture. In addition, an X-ray CT scan was conducted on an undamaged specimen to visualise the "as-manufactured" panel and capture all the geometrical distortions due to waviness and fabric compaction. The predicted values from the model overestimated the experimental response of the tested specimens as it did not include the effect of geometrical distortions and void content.

9.3 Summary

This study revealed the effect of the z-binder architecture on void content, directional fibre volume fraction, mechanical properties (on-axis and off-axis), failure mechanisms, energy absorption and fibre rotation angle in off-axis tested

specimens. In the case of the in-plane off-axis loading, having a through-thickness z-binder (ORT and AI) can suppress delamination and delay final failure. However, in the case of LTL architecture, delamination progression is guided by the z-binding yarns between layers which led to final failure. This is reflected on the strain to failure, strength and energy absorption of ORT being the highest followed by AI and finally LTL. The same effect is observed in the cases of the un-notched, notched and bearing strength of 3D woven composites. This suggests that optimisation of 3D woven composites design should consider the z-binder architecture depending on the application and avoid the layer-to-layer binding approach. Then, the second optimisation parameter is the unit cell size. For applications in which high strain to failure and higher energy absorption required, smaller weaving architecture unit cell with smaller unit cell size should be adopted such as the ORT architecture. In addition, off-axis loaded 3D woven composites have been proven to be relatively notch insensitive with high strain to failure and energy absorption especially the ORT architecture.

From the experimental point of view, this research work represents the first step to systematically characterise the loading direction sensitivity of different 3D woven composite architectures, and provides some basic guidelines for industrial and scientific communities for 3D woven composites' application-oriented design by understanding the influence of the z-binder architecture and weaving parameters "such as unit cell size" on the in-plane response as well as the loading direction effect. Moreover, electrical resistance monitoring (ERM) has been successfully introduced as a qualitative SHM for damage detection in 3D woven composites for the first time in the available literature.

From the simulation point of view, the proposed micro-mechanics model provides more efficient and predictive capabilities to existing unit cell models, which in turn reduces the need for extensive experimental characterisation, with a high level of confidence in the modelling results. The main contribution of the proposed model is that it relies only on few well-defined material parameters.

9.4 Recommendations for future work

Recommendations for future work that would be a valuable contribution to the current research work include:

- Manufacturing 3D woven composite laminates with liquid resin infusion instead of resin film infusion to determine the effect of the infusion process on void content.
- Weaving a "close to quasi-isotropic" 3D ORT fabric with the warp along the (0°) direction, the weft along the (90°) direction and the z-binder yarns in the off-axis direction (45°).
- Characterising the "quasi-isotropic" ORT architecture in tension and comparing it with results obtained from this study (Off-axis un-notched tension, Open-hole tension and Double-lap bearing strength).
- Extending the ERM method into electrical resistance tomography (ERT) to enable sizing and localising damage in 3D woven composite plates and structures. For simplicity, ERT can be applied for impact damage detection in 3D woven composite plates or the open-hole tension test.
- Carrying out X-ray CT scanning for interrupted open-hole tension to fully visualise the internal damage evolution in ORT, LTL and AI architectures.
- Investigating the effect of hole-size on the mechanical response of off-axis loaded 3D woven composites in open-hole tension.
- Improving the proposed micro-mechanics model using image-based FEM to account for geometrical imperfections due to manufacturing and incorporating plasticity models to account for the matrix viscoelasticity and damage evolution.
- Validating the improved model by simulating the off-axis tension response of 3D woven composites and ORT specifically.

References

[1] Ansar M, Xinwei W, Chouwei Z. Modeling strategies of 3D woven composites: A review. Compos Struct 2011;93:1947–63.

[2] Redman C, Bayraktar H, Mcclain M. Curved Beam Test Behavior of 3D Woven Composites. SAMPE Conf., 2014.

[3] Bayraktar H, Ehrlich D, Goering J, Mcclain M. 3D Woven Composites for Energy Absorbing. 20th Int. Conf. Compos. Mater., 2015, p. 19–24.

[4] Mcclain M. Overview of Recent Developments in 3D Structures. Albany Eng Compos 2012:1–12.

[5] 3d Woven Fabric Applications. 3Dwovens n.d.

[6] Jewell J, Kennedy R, Lecarrié G. FULL-SCALE LEAP FAN BLADE-OUT RIG TEST YIELDS OUTSTANDING RESULTS; ADVANCED LEAP FAN ENDURANCE TEST COMPLETE. CFM Power Flight 2011.

[7] Hemrick JG, Lara-Curzio E, Loveland ER, Sharp KW, Schartow R. Woven graphite fiber structures for use in ultra-light weight heat exchangers. Carbon N Y 2011;49:4820–9.

[8] Sharp K, Bogdanovich A, Boyle R, Brown J, Mungalov D. Wind blade joints based on non-crimp 3D orthogonal woven Pi shaped preforms. Compos Part A Appl Sci Manuf 2013;49:9–17.

[9] Mohamed MH, Wetzel KK. 3D Woven Carbon/Glass Hybrid Spar Cap for Wind Turbine Rotor Blade. J Sol Energy Eng 2006;128:562–73.

[10] L. Tong, A.P. Mouritz MB. Chapter 2 Manufacture of 3D Fibre Preforms. 3D Fibre Reinf. Polym. Compos., 2009.

[11] L. Tong, A.P. Mouritz MB. Chapter 5 3D Woven Composites. 3D Fibre Reinf. Polym. Compos., 2009.

[12] Stig F. 3D-woven Reinforcement in Composites. 2012.

[13] Stig F, Hallström S. Influence of crimp on 3D-woven fibre reinforced composites. Compos Struct 2013;95:114–22.

[14] Stig F, Hallström S. Assessment of the mechanical properties of a new 3D woven fibre composite material. Compos Sci Technol 2009;69:1686–92.

[15] Hao A, Sun B, Qiu Y, Gu B. Dynamic properties of 3-D orthogonal woven composite T-beam under transverse impact. Compos Part A Appl Sci Manuf 2008;39:1073–82.

[16] Ji C, Sun B, Qiu Y, Gu B. Impact damage of 3D orthogonal woven composite circular plates. Appl Compos Mater 2007;14:343–62.

[17] Luo Y, Lv L, Sun B, Qiu Y, Gu B. Transverse impact behavior and energy absorption of three-dimensional orthogonal hybrid woven composites. Compos Struct 2007;81:202–9.

[18] Seltzer R, González C, Muñoz R, LLorca J, Blanco-Varela T. X-ray microtomography analysis of the damage micromechanisms in 3D woven composites under low-velocity impact. Compos Part A Appl Sci Manuf 2013;45:49–60.

[19] Gerlach R, Siviour CR, Wiegand J, Petrinic N. In-plane and through-thickness properties, failure modes, damage and delamination in 3D woven carbon fibre composites subjected to impact loading. Compos Sci Technol 2012;72:397–411.

[20] Dai S, Cunningham PR, Marshall S, Silva C. Influence of fibre architecture on the tensile, compressive and flexural behaviour of 3D woven composites. Compos Part A Appl Sci Manuf 2015;69:195–207.

[21] Behera BK, Dash BP. Mechanical behavior of 3D woven composites. Mater Des 2015;67:261–71.

[22] Cox BN, Dadkhah MS, Morris WL, Flintoff JG. Failure mechanisms of 3D woven composites in tension, compression, and bending. Acta Metall Mater 1994;42:3967–84.

[23] Cox BN, Dadkhah MS, Morris WL. On the tensile failure of 3D woven composites. Compos Part A Appl Sci Manuf 1996;27:447–58.

[24] Lomov S V, Bogdanovich a E, Karahan M, Mungalov D, Verpoest I, Leuven KU. Mechanical Behaviour of Non-Crimp 3D Woven Carbon / Epoxy Composite Under in-Plane Tensile Loading. ICCM 18, 2011, p. 1–5.

[25] Leong KH, Lee B, Herszberg I, Bannister MK. Effect of binder path on the tensile properties and failure of multilayer woven CFRP composites. Compos Sci Technol 2000;60:149–56.

[26] Quinn JP, McIlhagger a. T, McIlhagger R. Examination of the failure of 3D woven composites. Compos Part A Appl Sci Manuf 2008;39:273–83.

[27] Pochiraju K. Three-Dimensionally Woven and Braided Composites. II: An Experimental Characterization. Polym Compos 1999;20:733–47.

[28] Tan P, Tong L, Steven GP, Ishikawa T. Behavior of 3D orthogonal woven CFRP composites. Part I. Experimental investigation. Compos Part A Appl Sci Manuf 2000;31:259–71.

[29] Warren KC, Lopez-Anido R a., Goering J. Experimental investigation of three-dimensional woven composites. Compos Part A Appl Sci Manuf 2015;73:242–59.

[30] Visrolia a., Meo M. Multiscale damage modelling of 3D weave composite by asymptotic homogenisation. Compos Struct 2013;95:105–13.

[31] Ivanov DS, Lomov S V., Bogdanovich AE, Karahan M, Verpoest I. A comparative study of tensile properties of non-crimp 3D orthogonal weave and multi-layer plain weave E-glass composites. Part 2: Comprehensive experimental results. Compos Part A Appl Sci Manuf 2009;40:1144–57.

[32] Flannery BP, Deckman HW, Roberge WG, Amico KLD. Three-Dimensional X-ray Microtomography. Science (80-) 1987;237:1439–44.

[33] Baruchel J, Buffiere JY, Maire E. X-ray tomography in material science. Hermes Sci Publ 2000.

[34] Landis EN, Keane DT. X-ray microtomography. Mater Charact 2010;61:1305–16.

[35] Salvo L, Cloetens P, Maire E, Zabler S, Blandin JJ, Buffière JY, et al. X-ray micro-tomography an attractive characterisation technique in materials science. Nucl Instruments Methods Phys Res Sect B Beam Interact with Mater Atoms 2003;200:273–86.

[36] Herman GT. Image reconstruction from projections. Real-Time Imaging 1995:3–18.

[37] Feldkamp L a., Davis LC, Kress JW. Practical cone-beam algorithm. J Opt Soc Am A 1984;1:612.

[38] Pan X, Sidky EY, Vannier M. Why do commercial CT scanners still employ traditional, filtered back-projection for image reconstruction? Inverse Probl 2009;25:123009.

[39] Davis GR, Elliott JC. Artefacts in X-ray microtomography of materials. Mater Sci Technol 2006;22:1011–8.

[40] Brooks R a, Di Chiro G. Beam hardening in x-ray reconstructive tomography. Phys Med Biol 1976;21:390–8.

[41] Lambert J, Chambers AR, Sinclair I, Spearing SM. 3D damage characterisation and the role of voids in the fatigue of wind turbine blade materials. Compos Sci Technol 2012;72:337–43.

[42] Nikishkov Y, Airoldi L, Makeev A. Measurement of voids in composites by X-ray Computed Tomography. Compos Sci Technol 2013;89:89–97.

[43] Bull DJ, Sinclair I, Spearing SM. Partial volume correction for approximating crack opening displacements in CFRP material obtained from micro-focus X-ray CT scans. Compos Sci Technol 2013;81:9–16.

[44] Yu B, Bradley RS, Soutis C, Hogg PJ, Withers PJ. 2D and 3D imaging of fatigue failure mechanisms of 3D woven composites. Compos Part A Appl Sci Manuf 2015.

[45] Wright P, Fu X, Spearing SM, Sinclair I. Ultra High Resolution Computed Tomography of Damage in Notched Carbon Fiber Epoxy Composites. J Compos Mater 2008;42.

[46] Bull DJ, Helfen L, Sinclair I, Spearing SM, Baumbach T. A comparison of multi-scale 3D X-ray tomographic inspection techniques for assessing carbon fibre composite impact damage. Compos Sci Technol 2013;75:55–61.

[47] Sket F, Enfedaque A, Alton C, González C, Molina-Aldareguia JM, Llorca J. Automatic quantification of matrix cracking and fiber rotation by X-ray

computed tomography in shear-deformed carbon fiber-reinforced laminates. Compos Sci Technol 2014;90:129–38.

[48] Aroush D, Maire E, Gauthier C, Youssef S, Cloetens P, Wagner H. A study of fracture of unidirectional composites using in situ high-resolution synchrotron X-ray microtomography. Compos Sci Technol 2006;66:1348–53.

[49] Desplentere F, Lomov S V., Woerdeman DL, Verpoest I, Wevers M, Bogdanovich A. Micro-CT characterization of variability in 3D textile architecture. Compos Sci Technol 2005;65:1920–30.

[50] Straumit I, Lomov S V., Wevers M. Quantification of the internal structure and automatic generation of voxel models of textile composites from X-ray computed tomography data. Compos Part A Appl Sci Manuf 2015;69:150–8.

[51] Coror PC, Owston CN. Electrical resistance of single carbon fibres. Nature 1969;224:488–90.

[52] Todoroki A, Yoshida J. Electrical Resistance Change of Unidirectional CFRP Due to Applied Load. JSME Int J Ser A 2004;47:357–64.

[53] Todoroki A, Ueda M, Hirano Y. Strain and Damage Monitoring of CFRP Laminates by Means of Electrical Resistance Measurement. J Solid Mech Mater Eng 2007;1:947–74.

[54] Todoroki A, Yoshida J. Apparent Negative Piezoresistivity of Single-Ply CFRP due to Poor Electrical Contact of Four-Probe Method. Key Eng Mater 2005;297–300:610–5.

[55] Schulte K, Baron C. Load and failure analyses of CFRP laminates by means of electrical resistivity measurements. Compos Sci Technol 1989;36:63–76.

[56] Ceysson O, Salvia M, Vincent L. Damage mechanisms characterisation of carbon fibre/epoxy composite laminates by both electrical resistance measurements and acoustic emission analysis. Scr Mater 1996;34:1273–80.

[57] Omagari K, Todoroki A, Shimamura Y, Kobayashi H. Detection of Matrix Cracking of CFRP Using Electrical Resistance Changes. Key Eng Mater 2005;297–300:2096–101.

[58] Todoroki A, Tanaka Y. Delamination identification of cross-ply graphite / epoxy composite beams using electric resistance change method 2002;62:629–39.

[59] Todoroki A, Suzuki K, Mizutani Y, Matsuzaki R. Electrical Resistance Change of CFRP under a Compression Load. J Solid Mech Mater Eng 2010;4:864–74.

[60] Abry JC. In situ detection of damage in CFRP laminates by electrical resistance measurements. Compos Sci Technol 1999;59:925–35.

[61] Abry, Choi, Chateauminois, Dalloz, Giraud, Salvia. In-situ monitoring of damage in CFRP laminates by menas of AC and DC measurement. Compos Sci Technol 2001;61:855–64.

[62] Hirano Y, Todoroki a. Damage Identification of Woven Graphite/Epoxy Composite Beams using the Electrical Resistance Change Method. J Intell Mater Syst Struct 2006;18:253–63.

[63] Wang S, Chung DDL, Chung JH. Impact damage of carbon fiber polymer-matrix composites, studied by electrical resistance measurement. Compos Part A Appl Sci Manuf 2005;36:1707–15.

[64] Todoroki A, Shimazu Y, Mizutani Y, Matsuzaki R, Samejima Y, Hirano Y, et al. Using Electrical Resistance Change to Monitor the Damage in a Thick CFRP Plate Caused by a Dent. J Solid Mech Mater Eng 2010;4:44–53.

[65] Jones R. Mechanics of Composite Materials. Second Edi. 1998.

[66] Kelly G. Load transfer in hybrid (bonded/bolted) composite single-lap joints. Compos Struct 2005;69:35–43.

[67] Sun CT, Luo J. Failure loads for notched graphite/epoxy laminates with a softening strip. Compos Sci Technol 1985;22:121–33.

[68] Kelly G. Joining of Carbon Fibre Reinforced Plastics for Automotive Applications. Royal Institute of Technology, Stockholm, Sweden, 2004.

[69] Goland M, Reissner E. The Stresses in Cemented Joints. J Appl Mech 1944:A17–27.

[70] Tong Liyong, Soutis Costas. Recent Advances in Structural Joints and Repairs for Composite Materials. Dordrecht: Springer Netherlands; 2003.

[71] Atas A. Strength Prediction of Mechanical Joints in Composite Laminates Based on Subcritical Damage Modelling. 2012.

[72] KUO W-S, PON B-J. Elastic moduli and damage evolution of three-axis woven fabric composites. Mater Sci 1997;2.

[73] Cox BN, Dadkhah MS. The Macroscopic Elasticity of 3D Woven Composites. J Compos Mater 1995;29:785–819.

[74] Tan P, Tong L, Steven GP. Models for Predicting Thermomechanical Properties of Three-Dimensional Orthogonal Woven Composites. J Reinf Plast Compos 1999.

[75] Tan P, Tong L, Steven GP. Micromechanics models for mechanical and thermomechanical properties of 3D through-the-thickness angle interlock woven composites. J Reinf Plast Compos 2006;30:637–48.

[76] Wu ZJ, Brown D, Davies JM. An analytical modelling technique for predicting the stiffness of 3-D orthotropic laminated fabric composites. Compos Struct 2002;56:407–12.

[77] Buchanan S, Grigorash A, Archer E, McIlhagger A, Quinn J, Stewart G. Analytical elastic stiffness model for 3D woven orthogonal interlock composites. Compos Sci Technol 2010;70:1597–604.

[78] Kim SJ, Ji KH, Paik SH. Numerical Simulation of Mechanical Behavior of

Composite Structures by Supercomputing Technology. Adv Compos Mater 2008;17:373–407.

[79] Lee CS, Chung SW, Kim SJ, Shin H. Virtual Material Characterization of 3D Orthogonal Woven Composite Materials by Large-scale Computing. J Compos Mater 2005;39:851–63.

[80] Wang XF, Wang XW, Zhou GM, Zhou CW. Multi-scale Analyses of 3D Woven Composite Based On Periodicity Boundary Conditions. J Compos Mater 2007;41:1773–88.

[81] Xia Z, Zhang Y, Ellyin F. A unified periodical boundary conditions for representative volume elements of composites and applications. Int J Solids Struct 2003;40:1907–21.

[82] Xia Z, Zhou C, Yong Q, Wang X. On selection of repeated unit cell model and application of unified periodic boundary conditions in micro-mechanical analysis of composites. Int J Solids Struct 2006;43:266–78.

[83] Tan P, Tong L, Steven GP. Behavior of 3D orthogonal woven CFRP composites . Part II . FEA and analytical modeling approaches 2006;31:273–81.

[84] Tong L, Tan P, Steven GP. Effect of yarn waviness on strength of 3D orthogonal woven CFRP composite materials. J Reinf Plast Compos n.d.;21:153–73.

[85] Yang C, Kim YK, Qidwai U a., Wilson a. R. Related Strength Properties of 3D Fabrics. Text Res J 2004;74:634–9.

[86] Jiwei D, Miaolin F. Damage Simulation for 3D Braided Composites by Homogenization Method. Chinese J Aeronaut 2010;23:677–85.

[87] Song S, Waas AM, Shahwan KW, Xiao X, Faruque O. Braided textile composites under compressive loads: Modeling the response, strength and degradation. Compos Sci Technol 2007;67:3059–70.

[88] Waas a. M, Shahwan KW, Faruque O. Compression Response of 2D Braided Textile Composites: Single Cell and Multiple Cell Micromechanics Based Strength Predictions. J Compos Mater 2008;42:2461–82.

[89] Alexander E. Bogdanovich. Progressive Failure Modeling and Strength Predictions of 3-D Woven Composites. Am Inst Aeronaut Astronaut 2009:1–20.

[90] Jia X, Xia Z, Gu B. Micro/meso-scale damage analysis of three-dimensional orthogonal woven composites based on sub-repeating unit cells. J Strain Anal Eng Des 2012;47:313–28.

[91] Sun B, Yao Y, Jin L, Gu B. Finite element analyses of stress distributions of three-dimensional angle-interlock woven composite subjected to three-point bending cyclic loading. J Text Inst 2013;104:1186–94.

[92] Yang G, Sun B, Gu B. Large-scale finite element analysis of a 3D angle-

interlock woven composite undergoing low-cyclic three-point bending fatigue. J Text Inst 2014;105:275–93.

[93] Nasution MRE, Watanabe N, Kondo A, Yudhanto A. Thermomechanical properties and stress analysis of 3-D textile composites by asymptotic expansion homogenization method. Compos Part B Eng 2014;60:378–91.

[94] Green SD, Matveev MY, Long a. C, Ivanov D, Hallett SR. Mechanical modelling of 3D woven composites considering realistic unit cell geometry. Compos Struct 2014;118:284–93.

[95] Kulkarni M, Carnahan D, Kulkarni K, Qian D, Abot JL. Elastic response of a carbon nanotube fiber reinforced polymeric composite: A numerical and experimental study. Compos Part B Eng 2010;41:414–21.

[96] Hexcel. HexTow ® IM7. 2014.

[97] Koerselman JR. A Multidisciplinary Optimization of Composite Space Enclosures. TU-Delft, 2012.

[98] Saleh MN, Yudhanto A, Potluri P, Lubineau G, Soutis C. Characterising the loading direction sensitivity of 3D woven composites: Effect of z-binder architecture. Compos Part A Appl Sci Manuf 2016;90:577–88.

[99] Saleh MN, Lubineau G, Potluri P, Withers PJ, Soutis C. Micro-mechanics based damage mechanics for 3D orthogonal woven composites : Experiment and numerical modelling. Compos Struct 2016;156:115–24.

[100] Daggumati S, Van Paepegem W, Degrieck J, Praet T, Verhegghe B, Xu J, et al. Local strain in a 5-harness satin weave composite under static tension: Part II - Meso-FE analysis. Compos Sci Technol 2011;71:1217–24.

[101] Obert E, Daghia F, Ladevèze P, Ballere L. Micro and meso modeling of woven composites: Transverse cracking kinetics and homogenization. Compos Struct 2014;117:212–21.

[102] Fuller JD, Wisnom MR. Pseudo-ductility and damage Suppression in thin ply angle-ply carbon-epoxy laminates. Compos Part A Appl Sci Manuf 2013;69:64–71.

[103] Bogdanovich AE, Karahan M, Lomov S V., Verpoest I. Quasi-static tensile behavior and damage of carbon/epoxy composite reinforced with 3D non-crimp orthogonal woven fabric. Mech Mater 2013;62:14–31.

[104] Mittelstedt C, Becker W. Free-Edge Effects in Composite Laminates. Appl Mech Rev 2007;60:217.

[105] Mittelstedt C, Becker W. Interlaminar Stress Concentrations in Layered Structures: Part I - A Selective Literature Survey on the Free-Edge Effect since 1967. J Compos Mater 2004;38:1037–62.

[106] Sun CT, Zhou SG. Failure of Quasi-Isotropic Composite Laminates with Free Edges. J Reinf Plast Compos 1988;7:515–57.

[107] Varna J, Berglund LA, Ericson ML. Transverse single-fibre test for

interfacial debonding in composites: 2. Modelling. Compos Part A Appl Sci Manuf 1997;28:317–26.

[108] Lubineau G, Ladeve P. On a damage mesomodel for laminates : micro – meso relationships , possibilities and limits. Compos Sci Technol 2001;61:2149–58.

[109] Lubineau G. A Pyramidal Modeling Scheme for Laminates - Identification of Transverse Cracking. Int J Damage Mech 2010;19:499–518.

[110] Nouri H, Lubineau G, Traudes D. An experimental investigation of the effect of shear-induced diffuse damage on transverse cracking in carbon-fiber reinforced laminates. Compos Struct 2013;106:529–36.

[111] Zhang J, Fan J, Herrmann KP. Delaminations induced by constrained transverse cracking in symmetric composite laminates. Int J Solids Struct 1999;36:813–46.

[112] Nairn J, Hu S. The initiation and growth of delamination induced by matrix microcracks in laminated composites. Int J Fract 1991:1–24.

[113] Ladèveze P, Lubineau G. An enhanced mesomodel for laminates based on micromechanics. Compos Sci Technol 2002;62:533–41.

[114] Beetz CP. The analysis of carbon fibre strength distributions exhibiting multiple modes of failure. Fibre Sci Technol 1982;16:45–59.

[115] Chi Z, Chou TW, Shen G. Determination of single fibre strength distribution from fibre bundle testings. J Mater Sci 1984;19:3319–24.

[116] Ansar M, Xinwei W, Chouwei Z. Modeling strategies of 3D woven composites: A review. Compos Struct 2011;93:1947–63.

[117] Aymerich F, Meili S. Ultrasonic evaluation of matrix damage in impacted composite laminates. Compos Part B Eng 2000;31:1–6.

[118] Sánchez DM, Gresil M, Soutis C. Distributed internal strain measurement during composite manufacturing using opical fibre sensors. Compos Sci Technol 2015;120:49–57.

[119] De Rosa IM, Santulli C, Sarasini F. Acoustic emission for monitoring the mechanical behaviour of natural fibre composites: A literature review. Compos Part A Appl Sci Manuf 2009;40:1456–69.

[120] Ciang CCC, Lee J-RJ, Bang HH-J. Structural health monitoring for a wind turbine system: a review of damage detection methods. Meas Sci Technol 2008;19:122001.

[121] Ng CT, Veidt M. A Lamb-wave-based technique for damage detection in composite laminates. Smart Mater Struct 2009;18:74006.

[122] Selvakumaran L, Lubineau G. Electrical behavior of laminated composites with intralaminar degradation : A comprehensive micro-meso homogenization procedure. Compos Struct 2014;109:178–88.

[123] Selvakumaran L, Long Q, Prudhomme S, Lubineau G. On the detectability

of transverse cracks in laminated composites using electrical potential change measurements. Compos Struct 2015;121:237–46.

[124] Song DY, Takeda N, Kitano A. Correlation between mechanical damage behavior and electrical resistance change in CFRP composites as a health monitoring sensor. Mater Sci Eng A 2007;456:286–91.

[125] Ogi K, Takao Y. Characterization of piezoresistance behavior in a CFRP unidirectional laminate. Compos Sci Technol 2005;65:231–9.

[126] Hirano, Yoshiyasu; Todoroki A. Damage Identification of Woven Graphite / Epoxy Composite Beams using the Electrical Resistance Change Method. J Intell Mater Syst Struct 2007;18:253–63.

[127] Berry B. Investigation of electrical and impact properties of carbon fiber textile composites. University of Iowa, 2014.

[128] Almuhammadi K, Selvakumaran L, Alfano M, Yang Y, Bera TK, Lubineau G. Laser-based surface preparation of composite laminates leads to improved electrodes for electrical measurements. Appl Surf Sci 2015;359:388–97.

[129] Yudhanto A, Lubineau G, Ventura IA, Watanabe N, Iwahori Y, Hoshi H. Damage characteristics in 3D stitched composites with various stitch parameters under in-plane tension. Compos Part A Appl Sci Manuf 2015;71:17–31.

[130] Selvakumaran L. Effect of voltage measurement on the quantitative identification of transverse cracks by electrical measurements. Sensors (Switzerland) 2016;16.

[131] Ataş a., Soutis C. Subcritical damage mechanisms of bolted joints in CFRP composite laminates. Compos Part B Eng 2013;54:20–7.

[132] O'Higgins RM, McCarthy MA, McCarthy CT. Comparison of open hole tension characteristics of high strength glass and carbon fibre-reinforced composite materials. Compos Sci Technol 2008;68:2770–8.

[133] Awerbuch J, Madhukar MS. Notched Strength of Composite Laminates : Predictions and Experiments & mdash - A Review. J Reinf Plast Compos Reinf 1985;4:3–159.

[134] Callus PJ. The Effects of Hole-size and Environment on the Mechanical Behaviour of a Quasi-isotropic AS4 / 3501-6 Laminate in Tension , Compression and Bending. n.d.

[135] Yudhanto A, Watanabe N, Iwahori Y, Hoshi H. The effects of stitch orientation on the tensile and open hole tension properties of carbon/epoxy plain weave laminates. Mater Des 2012;35:563–71.

[136] Yudhanto A, Iwahori Y, Watanabe N, Hoshi H. Open hole fatigue characteristics and damage growth of stitched plain weave carbon/epoxy laminates. Int J Fatigue 2012;43:12–22.

[137] Naik NK, Shembekar PS, Verma MK. On the Influence of Stacking Sequence

on Notch Sensitivity of Fabric Laminates. J Compos Mater 1990;24:838–52.

[138] Shembekar PS, Naik NK. Notched strength of fabric laminates. II: Effect of stacking sequence. Compos Sci Technol 1992;44:13–20.

[139] Tsai KH, Chiu CH, Wu TH. Fatigue behavior of 3D multi-layer angle interlock woven composite plates. Compos Sci Technol 2000;60:241–8.

[140] Dai S, Cunningham PR, Marshall S, Silva C. Open hole quasi-static and fatigue characterisation of 3D woven composites. Compos Struct 2015;131:765–74.

[141] Mubeen A. Damage Tolerance of 3D Woven Composites with Weft Binders. University of Manchester, 2014.

[142] Yang QQ, Gao CF, Chen WT. Stress concentration in a finite functionally graded material plate. Sci China Physics, Mech Astron 2012;55:1263–71.

[143] Ataş a., Soutis C. Strength prediction of bolted joints in CFRP composite laminates using cohesive zone elements. Compos Part B Eng 2014;58:25–34.

[144] Kelly G, Hallström S. Bearing strength of carbon fibre/epoxy laminates: Effects of bolt-hole clearance. Compos Part B Eng 2004;35:331–43.

[145] Khashaba U a., Sebaey T a., Alnefaie K a. Failure and reliability analysis of pinned-joints composite laminates: Effects of stacking sequences. Compos Part B Eng 2013;45:1694–703.

[146] Öndürücü A, Esendemir Ü, Tunay RF. Progressive failure analysis of glass-epoxy laminated composite pinned-joints. Mater Des 2012;36:617–25.

[147] Pisano a. a., Fuschi P. Mechanically fastened joints in composite laminates: Evaluation of load bearing capacity. Compos Part B Eng 2011;42:949–61.

[148] Thoppul SD, Finegan J, Gibson RF. Mechanics of mechanically fastened joints in polymer-matrix composite structures - A review. Compos Sci Technol 2009;69:301–29.

[149] Warren KC, Lopez-Anido RA, Goering J. Behavior of three-dimensional woven carbon composites in single-bolt bearing. Compos Struct 2015;127:175–84.

[150] ASTM D5961. Standard Test Method for Bearing Response of Polymer Matrix Composite Laminates. Annu B ASTM Stand 2003;i:1–18.

[151] Mao JZ, Sun XS, Ridha M, Tan VBC, Tay TE. A Modeling Approach Across Length Scales for Progressive Failure Analysis of Woven Composites. Appl Compos Mater 2012;20:213–31.

[152] Ruijter W. Analysis of mechanical properties of woven textile composites as a function of textile geometry 2010.

[153] Ladevèze P, Lubineau G. On a damage mesomodel for laminates: micro–meso relationships, possibilities and limits. Mech Mater 2003;35:763–75.

[154] Ladevèze P, Lubineau G. On a damage mesomodel for laminates:

Micromechanics basis and improvement. Mech Mater 2003;35:763–75.

[155] Czabaj MW, Ratcliffe JG. Comparison of Intralaminar and Interlaminar Mode-I Fracture Toughness of Unidirectional IM7/8552 Graphite/Epoxy Composite. 15th US-Japan Conf Compos Mater 2012:18.

[156] Obert E, Daghia F, Ladevèze P, Ballere L. Micro and meso modeling of woven composites: Transverse cracking kinetics and homogenization. Compos Struct 2014;117:212–21.

[157] Fang G, El Said B, Ivanov D, Hallett SR. Smoothing artificial stress concentrations in voxel-based models of textile composites. Compos Part A Appl Sci Manuf 2016;80:270–84.

[158] Doitrand a., Fagiano C, Irisarri F-X, Hirsekorn M. Comparison between voxel and consistent meso-scale models of woven composites. Compos Part A Appl Sci Manuf 2015;73:143–54.